ANALYSIS OF PARTIAL DIFFERENTIAL EQUATIONS WITH TIME-PERIODIC FORCING, APPLICATIONS TO NAVIER-STOKES EQUATIONS

By
Corina Alexandra Coros
Department of Mathematics and Statistics
May 2006

A Thesis
submitted to the School of Graduate Studies and Research
in partial fulfillment of the requirements
for the degree of
Doctor of Philosophy in Mathematics[1]

[1]The Ph.D. Program is a joint program with Carleton University, administered by the Ottawa-Carleton Institute of Mathematics and Statistics

Abstract

Flows with time-periodic forcing can be found in various applications, such as the circulatory and respiratory systems, or industrial mixers. In this thesis, we address few questions in relation with the time-periodic forcing of flows and related partial differential equations (PDE), including the linear Advection-Diffusion equation.

In Chapter 2, we first study linear PDE's with non-symmetric operators subject to time-periodic forcing. We prove that they have a unique time-periodic solution which is stable and attracts any initial solution if the bilinear form associated to the operator is coercive, and we obtain an error estimate for finite element method with a backward Euler time-stepping scheme. That general theory is applied to the Advection-Diffusion equation and the Stokes problem. The first equation has a non-symmetric operator, while the second has a symmetric operator but two unknowns, the velocity and pressure. To apply the general theory, we prove an error estimate for a Riesz projection operator, using a special Aubin-Nistche argument for the Advection-Diffusion equation with a time-dependent advective velocity. A spectral analysis for the 1-D Advection-Diffusion equation, relevant parameters that control the speed of convergence of any initial solution to the time-periodic solution are identified.

In Chapter 3, we extend a theorem of J.L. Lions about the existence of time-periodic solutions of Navier-Stokes equations under periodic distributed forcing with homogeneous Dirichlet boundary conditions to the case of non-homogeneous time-periodic Dirichlet boundary conditions. Our theorem predicts the existence of a time-periodic solution for Navier-Stokes equations subject to time-periodic forcing but the stability of these time-periodic solutions is not known.

In Chapter 4, we investigate the stability of these time-periodic solutions, through numerical simulations with test cases in a 2-D time-periodic lid driven cavity and a 2-D constricted channel with a time-periodic inflow. From our numerical simulations, it seems that a bifurcation occurs in the range 3000–8000 in the periodically driven cavity, and the range 400–1200 in the periodically driven channel.

ACKNOWLEDGMENTS

I would like to express my gratitude and respect to my supervisor Prof. Yves Bourgault for his advice, guidance and encouragement throughout the study and preparation of this thesis. I thank Prof. Yves Bourgault for introducing me to this research subject, for the many inspiring discussions and suggestions he provided and for supporting me financially.
I would like to thank the Department of Mathematics and Statistics for the financial support.
A special thank go to my parents, my husband and family for their moral support.
My thanks also go to my colleagues and friends.

I dedicate this work to my daughter Laura-Christine.

Contents

List of Figures

List of Tables

Chapter 1

Introduction

1.1 Motivation

Time-periodic flows can be found in various applications, such as the circulatory system, respiratory system or industrial mixers. We first review two important applications of periodic flows, namely the lid-driven cavity flows and blood flows in arteries.

1.1.1 Lid-driven Cavity

Lid-driven cavities are a class of internal recirculating flows, usually bounded, of an incompressible, viscous, Newtonian fluid in which the motion is generated by the motion of a portion of the boundary. Cavity flows are important in a number of industrial contexts in which these flows and the structures they exhibit play a role. In [30] and [1], the authors point out the direct relevance of cavity flows to coaters and melt spinning processes used to manufacture microcrystalline materials. The eddy structures found in driven-cavity flows give insights into the behavior of such structures in applications as diverse as drag-reducing riblets and mixing cavities used to synthesize fine polymeric composites. In fact, the driven cavity problem is one of the standard test cases used to test new computational schemes. Another advantage

of this class of flows is that the flow domain is very simple, a square or a rectangle in 2-D. They exhibit almost all phenomena that can possibly occur in the incompressible flows: eddies, secondary flows, instabilities, transition and turbulence which make them an interesting test case.

1.1.2 Blood Flow in Arteries

The mathematical setting of blood flow in arteries has been presented in detail in [18] and [11]. From a physiological point of view, blood is a mixture of cells, proteins, lipoproteins and ions by which nutrients are transported. Red blood cells typically comprise approximately half of the blood's volume. They are small semisolid particles, they increase the viscosity of the blood and make the blood almost four times more viscous than water. Moreover, blood does not exhibit a constant viscosity at all flow rates and it is non-Newtonian in the microcirculatory system. However, in sufficiently large arteries, blood behaves in a Newtonian way, under normal physiological conditions.

Blood velocity and pressure are unsteady. The heart pumps the blood in a cyclic fashion and creates pulsatile conditions in all arteries. Pressure and velocity are different in various parts of the arterial system and different from the normal Poiseuille flow. The typical Reynolds number ranges from 1 in small arteries to 4000 in the largest artery, such as the aorta. Thus the flow spans a range of Reynolds numbers in which the viscous forces are dominant on one end and inertial forces are more important on the other.

A simplified model of the blood flow in arteries considers a Newtonian flow where two non-dimensional parameters, the Reynolds (Re) and Strouhal (Str) numbers govern the flow field (see [25]). The Strouhal number corresponds to the non-dimensional frequency of the inlet flow pulsation and it is less than 1 in the circulatory system. A dimensional analysis of the unsteady Navier-Stokes equations subject to a periodic forcing, gives a nondimensional number known as the Womersley parameter, $Wo = (\frac{\pi ReStr}{2})^{\frac{1}{2}}$. This parameter Wo can be interpreted as the ratio of the periodic inertial forces to the viscous forces. When the Womersley parameter is low, viscous

forces dominate, velocity profiles are nearly parabolic in shape, and the centerline velocity oscillates in phase with the driving pressure gradient. For Womersley parameters above 10, the unsteady inertial forces dominate, and the flow has a flat velocity profile, eventually with small reversed flow regions, near the wall.

1.2 Literature review

1.2.1 Numerical and experimental studies of time-periodic flows

The study of time-periodic flows has been done before, especially in engineering and bio-fluid applications. As we mentioned before there are a large number of applications of lid-driven cavity flows in industrial applications, see [30]. That paper, which is a very good review of the subject, presents the detailed structure of cavity flows where the flow is generated by the steady, uniform motion of one of the walls alone, the lid. Applying the no-slip conditions on the side walls, and the bottom of the cavity, some features of cavity flow fields will show up. Some characteristics such as primary eddies, corner eddies, corner singularities will appear. The simulation will reveal the tendency of the core fluid to move almost like a solid body with uniform vorticity when we approach a $Re = 10000$. The paper also suggests that a critical Reynolds number for which the flow becomes unstable is $Re = 13000$. It is difficult to investigate this question when we talk about 2-D flows because they are almost fictious: 3-D effects rapidly appear when increasing the Reynolds number.
The problem of finding such a critical Reynolds number is not an easy one. Different studies have been done, one to mention is the paper by A. Fortin et al. [10]. That paper is concerned with precise localization of Hopf bifurcations in various fluid flow problems. One of them is the steady lid-driven cavity flow and the approach used was the computation of eigenvalues of a large matrix corresponding to the linearization of the discretized Navier-Stokes equations in the neighborhood of the stationary solution, which is a standard technique in bifurcation theory. The critical Reynolds

number was found to be around $Re = 8000$.

Despite the fact that lid-driven cavity flows have been studied intensively, few attempts have been made to study time-periodic lid-driven cavity flows. We can mention the work of M.J. Vogel, L. Marquez et al. (see [33], [19], [20]). They have done experimental and numerical work on a 3-D flow in a rectangular cavity driven by the sinusoidal motion of the floor. Their results show that the harmonic oscillation of the floor in the cavity introduces a spatio-temporal invariance. The basic state becomes unstable via symmetry breaking bifurcations. The time-periodic base flow may loose stability in a number of ways: One is via synchronous bifurcations, when a Floquet multiplier crosses the unit circle at $+1$, and another time-periodic state results. Another possibility is for a pair of complex conjugate Floquet multipliers to cross the unit circle, giving rise to a quasi-periodic state. The third generic type of bifurcation occurs via period-doubling. It was also noticed that the system has a space-time symmetry that consists of a reflection about the vertical mid-plane together with a half-period translation in time. The paper is an excellent presentation of the behavior of time-periodic flows in a cavity for Reynolds numbers up to $Re = 1163$ and a fixed period of $T = \frac{1}{53}$. They did not experiment with other parameters such as the period, which as we will see plays an important role in the flow stability.

Another paper of H.M.Blackburn and M.Lopez (see [3]) presents a Floquet analysis of a time-periodic driven-cavity flow. The two-dimensional base flow has no component in the spanwise direction and is periodic in time. In addition, it appears that it has the same space-time symmetry as the two-dimensional periodically shedding bluff-body wake: Invariance to a midplane reflection composed with a half-period evolution in time. A new synchronous mode is found, in addition to the experimentally observed mode. These two modes have very different spanwise length: A long wave-length (named mode A) and a short wave-length (named mode B). They both result from synchronous bifurcations. A third mode (mode QP) has been found. This last one results from a complex conjugate pair of Floquet multipliers crossing the unit circle, and it arises through a Neimark-Sacker bifurcation of the base flow. This mode gives rise to a quasi-periodic state. The Floquet analysis emphasizes the dependence of the stability on the Reynolds number and the period T. In that article the authors

experiment with Reynolds numbers up to $Re = 1500$ and two values of the Strouhal number, $Str = 100$ and $Str = 160$, but they could not identify period-doubling bifurcations.

Other studies have been done to obtain critical Reynolds numbers. For example, P.S. Casas and A. Jorba (see [5]) have identified a critical Reynolds numbers, $Re = 5772.22$, and another Hopf bifurcation at $Re = 7400$ for a wavenumber of 1.02056 in the two-dimensional Poiseuille problem. They also observed the existence of quasi-periodic solutions. Other papers to be mentioned are [19] and [20] where the attention is focused on the occurrence of a Naimark-Sacker bifurcation in a periodically forced system, i.e in a Taylor-Couette flow with axial oscillations of the inner cylinder. They study the linear stability of the spiral Poiseuille flow, covering a wide range of angular velocities of the inner and outer cylinders and values of the axial Reynolds number.

In the domain of blood flow applications one of the most cited books is that of McDonald (see [18]) which has proved to be a cornerstone in this field. The first studies considered the arteries as a straight pipe or a channel where we have a Hagen-Poiseuille flow and plane Poiseuille flow. In [18], an analytical expression for the fully developed pulsatile flow in a straight or a tapered tube is presented. This idea is not new and the result was developed by Womersley in 1955 (see [36]).

Atherosclerosis is a disease of the cardiovascular system which involves the hardening of the arteries due to the deposition of fat. Atherosclerotic constrictions in arteries is known as arterial stenoses. Fluid dynamics of post-stenotic flow plays a key role in the diagnosis of arterial diseases. For two hundred years it has been known that stenosis in arteries produce distinct sounds known as “bruits” which can be heard externally. The general understanding is that the sounds are produced by the ”disturbed” flow downstream of the stenosis, but until 1960s little work has been done to explore the origin of these sounds. Studies done later showed that sounds are due to the shear layer and not to the turbulence in the core of the flow as it was believed. This conclusion is also reached by R.Mittal et al. [21], considering flows in a channel with time-periodic inflow. Their experiments show a vortex structure downstream of the constriction. These vortices form in the shear layers and become more energetic

when the Reynolds number is increased, leading to a higher turbulent kinetic energy. In that article, the Reynolds number was varied over a range of 750 to 2000.
Among the abundant literature, a couple of articles draw our attention. In 1995, M. Rosenfeld [25] described his numerical experiments on 2-D flows in a constricted channel with a pulsating entry. As previous results showed [2], even cases with steady flows at the inlet may exhibit complex patterns. Depending on the geometry and flow conditions, several separation eddies may be generated behind the constriction, and at Reynolds numbers of $O(10^3)$, the flow becomes unsteady and vortices are shed periodically. In [25] the study of pulsating flows was extended to different parameter regimes. Their study focuses on the two most important factors: the Strouhal and Reynolds numbers. The Strouhal number is varied by three orders of magnitude ($12 > Str > 0.01$) while the Reynolds number is changed by almost two orders of magnitude ($1500 > Re > 45$). However, their work did not identify a critical Reynolds number at which the solution becomes unstable.

1.2.2 Theoretical and numerical studies on periodically forced PDEs

Aside from experiments with particular periodically-driven flows, there is a core of theory for PDEs with periodic forcing term, in terms of existence, convergence and numerical methods. A theoretical result on the existence of a time-periodic solution of the Navier-Stokes equations with a time-periodic volumic force was presented by J.L.Lions, see [17]. A missing part in his theory is the analysis of the stability and uniqueness of the time-periodic solution. Moreover, the analysis is done only for volumic forcing with no-slip velocity on all boundaries, which is far from the current practice with periodically forced flows.
Further studies on periodically forced partial differential equations were done by O.Vejvoda [32]. These studies have been developed using Fourier analysis, just for 1-D problems and they do not extend to higher dimensions. C. Bernardi (see [4]) published an article on the numerical approximation of periodic linear parabolic problems with symmetric operators. The discretization uses a Galerkin method for

the space variables and a spectral method for the time variable. Some optimal error estimates are derived. The proof depends on a spectral decomposition in time and therefore the results do not apply to problems where the elliptic spatial operator is time dependent.

Another approach to approximate the periodic parabolic problems has been suggested by C.V.Pao [23]. His method is based on the method of upper and lower solutions and associated monotone iterations. The analysis of periodic solutions of a finite difference system which is a discrete version of a class of nonlinear reaction-convection-diffusion equations is being performed. This method leads to an existence-comparison theorem for periodic solutions of the nonlinear finite difference system. The existence-comparison theorem can be used to show the convergence of a discrete solution to a continuous solution of the original problem. The numerical schemes use a combination of Picard type and Jacobi type monotone iterative schemes.

The calculation of periodic orbits for system of ODEs has been studied before by J. Guckenheimer [13], where the shooting method is applied. However, the method is difficult to implement when we deal with large systems of equations. Algorithms for the computation and bifurcation analysis of periodic solutions of systems of nonlinear autonomous partial differential equations have been studied by K. Lust [16]. The methods are based on single and multiple shooting that exploits the property of PDEs to have periodic orbits with only few unstable or weakly stable modes. Among the techniques presented by K.Lust, the periodic Schur decomposition is capable to compute an eigenvalue spectrum characterized by extreme differences in the magnitude of the eigenvalues. These methods prove to be efficient for autonomous equations but the author did not consider the case of non-autonomous systems.

The Picard iteration is also used in the paper of A. Hansbo (see [14]) where the convergence is proved for the semi-discrete Galerkin method and for a fully discrete method obtained by using the Backward Euler method. These methods can be shown to have the desired contractivity property by an energy argument. However, the results are proven only for symmetric operators. The heat equation is considered in that article, but not the advection-diffusion equation.

1.3 Purpose of the work

The present work is intended to be a study of time-periodic parabolic problems, in particular the Navier-Stokes and related problems, from numerical and theoretical point of views. From theoretical point of view we extend some previous results to more complicated cases. Through numerical experiments we want to find some relevant situations which might lead us to unstable time-periodic solutions.

- **Chapter 2** In the beginning of this chapter, there is a review on the convergence analysis of the semi-discrete and fully-discrete approximations for a general linear parabolic problem. The theory presented by A. Quarteroni, A.Valli [35] and A. Ern, J.L. Guermond [9] are combined and presented here in a uniform manner. The second section takes the results obtained by A. Hansbo [14] on the convergence analysis of a time-periodic solution of linear parabolic problem with a symmetric operator and extends these results to the case with a non-symmetric operator. The results are true only when the projection operator defined from the space of test functions to its finite-dimensional subspace has some special properties and when the bilinear form, associated to our operator, is coercive. In the next section we take an example of parabolic problems with non-symmetric operators; the advection-diffusion equation with a time-dependent advective ve locity. In this case, we had to prove the properties needed to apply the general theory for the projection operator. A special Aubin-Nitsche argument is required to deal with the advective part of the advection-diffusion operator. To our knowledge, a similar analysis for time-periodic solutions of parabolic PDEs with non-symmetric operators is not available in the literature. Also, the Stokes problem is presented, because of the difficulties imposed by the presence of two unknowns, the velocity and the pressure.There are two projection operators to deal with, one is the projection of the velocity and the other is the projection of the pressure. The velocity projection operator satisfies the needed properties and so, the general theory applies for the Stokes problem. The last section of that chapter presents an analysis of the computational results obtained for the 1-D advection-diffusion equation. First, taking a specific problem, we show

that the coercivity of the bilinear form is a necessary condition for the existence and convergence to a periodic solution, at least for some problems. Basically, for the pure advection equation, the bilinear form is not coercive and we may not obtain a time-periodic solution. Then, we focus on the identification of the relevant parameters that control the convergence of the solution of the initial-value problem toward a time-periodic solution. A spectral analysis of the fully-discrete problem and also of the semi-discrete problem is done.

- **Chapter 3** The main topic of this chapter is time-periodic solutions of the Navier-Stokes equations. In his book, J.L. Lions ([17]) proved the existence of a time-periodic solution for the Navier-Stokes equations, when a time-periodic volumic forcing term is applied to the system and homogeneous Dirichlet boundary conditions are being considered. We are interested in flows that are driven by periodic non-homogeneous boundary conditions instead of volumic forces. We prove the existence of a time-periodic solution of the Navier-Stokes problem in this situation. In order to generalize the results obtained by J.L. Lions, the non-homogeneous boundary conditions must be treated in such a way that the problem could be transformed into one with homogeneous Dirichlet boundary conditions. To show how we can treat the boundary conditions, we presented first, the proof of existence of a solution of the Navier-Stokes equations with non-homogeneous boundary conditi ons, not necessarily time-periodic.

- **Chapter 4** The results of our numerical experiments are presented here. The simulations are done for 2-D flows only, but for a relatively large range of Reynolds and Strouhal numbers. We use the results obtained by A. Fortin et al. [10] to validate our code. The simulations are divided into two main parts, the lid-driven cavity and an artery with a stenotic region in the middle. The stenosis is considered to be deformed in both upper and lower wall, while the simulations done so far to characterize the stability of the flow with periodic inflow,(e.g. [21]), consider the deformation of the upper wall only. We calculate the solutions at different Reynolds and Strouhal numbers. What we observed

was that the higher the Reynolds number, the longer is the transition to a time-periodic solution, if the solution is periodic at all. The period plays a role in the stability of a solution. A small period seems to increase the instability of the flow as observed for flow in stenotic arteries. The number of periods needed to obtain a time-periodic solution is monitored. The simulations are carried over different ranges of Reynolds and Strouhal numbers, some of the cases being suggested by the literature available ([25], [21]). We also tried to increase the number of test cases. Our simulations monitor the number of periods needed to obtain a time-periodic solution. We also try to identify flows with Reynolds numbers beyond the critical values for a bifurcation to a quasi-periodic flow.

Chapter 2

Time-periodic solution of linear parabolic problems

A.Hansbo (see [14]) presented some error estimates on the numerical solution of the time-periodic linear parabolic problems with a symmetric operator. These results will be extended in this Chapter to a non-symmetric operator as we will see in Sections 2.1 and 2.2. The advection-diffusion problem is a very attractive test case because it possesses two properties: It has a non-symmetric operator and shares many characteristics with the Navier-Stokes problem. We will discuss that problem in Sections 2.3.1. We also present an application of the general theory to the Stokes problem in Section 2.3.2. The 1-D advection-diffusion equation and some mechanisms that control the convergence of the transient solution toward a periodic solution will be investigated in Section 2.4 as well.

2.1 Initial value problem for a general parabolic equation

Semi-discrete finite element approximations of linear parabolic equations have been studied extensively. As references, [35, chapter 11] and [9, chapter 6] offer an excellent review of the main results and mathematical techniques on this subject.

This section is a review of the main results on the error estimates for the solution of the semi-discrete problem and the fully discrete problem with the backward Euler time discretization.

Let Ω be a bounded domain in $\mathbb{R}^d$, $d = 2,3$ with a Lipschitz boundary. Consider a second order elliptic differential operator L. The initial value problem writes as: Find u solution of

$$\begin{aligned} \frac{\partial u}{\partial t} + Lu &= f \quad in \quad (0,T) \times \Omega \\ u &= 0 \quad on \quad (0,T) \times \partial\Omega \\ u(0) &= u_0 \quad on \quad \Omega \end{aligned} \tag{1}$$

where L is a linear differential operator acting on a subspace of the Hilbert space H (in general $H = L^2(\Omega)$ so the norm of H is denoted by $\| \cdot \|$).

Problem (1) can be reformulated in a weak variational form, therefore we introduce the space V with the norm $\| \cdot \|_1$ as the space of test functions and $W(V)$ as the space of admissible solutions:

$$W(V) := \{u : (0,T) \to V | u \in L^2(0,T;V), d_t u \in L^2(0,T;V')\} \tag{2}$$

where V' is the dual space of V. V is dense in H and the injection from V to H is continuous. There is a Poincaré-type inequality between the V- and H-norms in the sense that there exist a constant $c_P > 0$ such that

$$c_P \parallel u \parallel^2 \leq \parallel u \parallel_1^2$$

The homogeneous Dirichlet's boundary condition requires that $V = H_0^1(\Omega) \subseteq H^1(\Omega)$ in case $L = -\Delta$ or a related operator.

The weak formulation

For all $f \in L^2(0,T;V')$ and $u_0 \in L^2(\Omega)$ we consider the following problem: Find $u \in W(V)$ such that

$$\begin{aligned} \frac{d}{dt} < u, v >_{V \times V'} + a(t;u,v) &= < f, v >_{V \times V'}, \quad for \quad any \quad v \in V \\ u(0) &= u_0 \end{aligned} \tag{3}$$

It is assumed that the bilinear form $a(t;u,v) : V \times V \to \mathbb{R}$ is coercive in the Hilbert space V with a constant α and continuous with a constant M, both independent of time, namely

$$a(t;v,v) \geq \alpha \parallel v \parallel_1^2 \tag{4}$$

$$a(t;u,v) \leq M \parallel u \parallel_1 \parallel v \parallel_1 \tag{5}$$

The existence of a solution has been proved using different methods, for example in [22] the proof is based on semigroup theory or in [6] a Galerkin approach is used.
To discretize the problem (3) we introduce a family of finite-dimensional subspaces $S_h \subset V$, with $h > 0$, such that

$$\parallel w - I_h(w) \parallel_{C^1(0,T;H)} + h \parallel w - I_h(w) \parallel_{C^1(0,T;V)} \leq Ch^{r+1} \parallel w \parallel_{C^1(0,T;H^{r+1})}, \tag{6}$$
$$for \quad any \quad w \in C^1(0,T;V \bigcap H^{r+1}(\Omega))$$

where I_h is the usual Lagrange interpolation operator of degree r (as defined in [9]). For all $t \in [0,T]$ we introduce the projection operator $\Pi_h : V \to S_h$ such that $\Pi_h(w)$ is the solution of

$$a(t;\Pi_h(w),v_h) = a(t;w,v_h) \text{ for all } v_h \in S_h \tag{7}$$

In the following we suppose that the projection operator $\Pi_h(w)$ satisfies the following **Projection Property**

$$\parallel w - \Pi_h(w) \parallel_{C^1(0,T;H)} + h \parallel w - \Pi_h(w) \parallel_{C^1(0,T;V)} \leq Ch^{r+1} \parallel w \parallel_{C^1(0,T;H^{r+1})} \tag{8}$$

This property will be proven below for particular bilinear forms $a(t;\cdot,\cdot)$, e.g. for the advection-diffusion equation. As we shall see, (8) is a very important hypothesis in the next section.
Another important tool in our demonstrations is the Gronwall Lemma (see [9]) which states as follows

Lemma 2.1.1. ***Gronwall Lemma****: Consider $\beta \in \mathbb{R}$, $\phi \in C^1(0,T;\mathbb{R})$ and $f \in C^0(0,T;\mathbb{R})$ such that $\frac{d\phi}{dt} \leq \beta\phi + f$. Then*

$$\phi(t) \leq e^{\beta t}\phi(0) + \int_0^t e^{\beta(t-\tau)} f(\tau) d\tau \tag{9}$$

Semi-discrete approximation

We consider the semi-discrete approximate problem which reads as follows : Given $u_{0,h} \in S_h$ a suitable approximation of the initial datum $u_0 \in L^2(\Omega)$, for each $t \in [0,T]$ find $u_h(t) \in S_h$ such that

$$\begin{aligned} \frac{d}{dt} < u_h(t), v_h > + a(t; u_h(t), v_h) &= < f(t), v_h >, \quad for \quad any \quad v_h \in S_h, t \in (0,T) \\ u_h(0) &= u_{0,h} \end{aligned} \tag{10}$$

Theorem 2.1.2. *Assume that the solution u of (3) is such that $u \in C^1(0,T; H^{r+1}(\Omega))$, $r \geq 1$. Then, using piecewise-polynomials of degree less than or equal to r in the definition of the finite element space S_h, for each $t \in [0,T]$ and assuming that (8) holds, the solution u_h of (10) satisfies*

$$\| u(t) - u_h(t) \| \leq \| u(0) - u_{0,h} \| + C_1 h^{r+1} \| u \|_{C^1(0,T;H^{r+1})} \tag{11}$$

where $C_1 > 0$ is a suitable constant independent of h.

Proof. We make use of the projection operator Π_h defined in (7). By (8) we have that

$$\| u - \Pi_h(u) \|_{C^1(0,T;H)} + h \| u - \Pi_h(u) \|_{C^1(0,T;V)} \leq C h^{r+1} \| u \|_{C^1(0,T;H^{r+1})} \tag{12}$$

For all $t \in [0,T]$ let us write $u_h(t) - u(t) = v_1(t) + v_2(t)$ where
$v_1(t) := u_h(t) - \Pi_h(u(t))$ and $v_2(t) := \Pi_h(u(t)) - u(t)$.
Substituting v_2 in the inequality (12) we can estimate that

$$\sup_{0 \leq \tau \leq t} (\| v_2(\tau) \| + \| \frac{\partial v_2(\tau)}{\partial \tau} \|) \leq C h^{r+1} \| u \|_{C^1(0,T;H^{r+1})} \tag{13}$$

Also, $\| v_1(t) \|$ must be bounded. First we subtract (3) from (10) to obtain

$$\frac{d}{dt} < u_h(t) - u, v_h > + a(t; u_h(t) - u, v_h) = 0 \tag{14}$$

From the definition of the projection operator (7), the definition of $v_1(t)$ and the use

of (14) we have that

$$\begin{aligned}
< \frac{dv_1}{dt}(t), v_h > + a(t; v_1(t), v_h) &= < \frac{du_h(t)}{dt}, v_h > + a(t; u_h(t), v_h) \\
&- < \frac{d\Pi_h(u(t))}{dt}, v_h > - a(t; \Pi_h(u(t)), v_h) \\
&= < \frac{du_h(t)}{dt}, v_h > + a(t; u_h(t), v_h) \\
&- < \frac{d\Pi_h(u(t))}{dt}, v_h > - a(t; u(t), v_h) \\
&= < \frac{du_h(t)}{dt}, v_h > - < \frac{d\Pi_h(u(t))}{dt}, v_h > - \frac{d}{dt} < u_h - u, v_h > \\
&= < \frac{du(t)}{dt}, v_h > - < \frac{d\Pi_h(u(t) >}{dt}, v_h) = < - \frac{dv_2(t)}{dt}, v_h >
\end{aligned}$$

Choosing $v_h = v_1(t)$ it follows from that last equality

$$\frac{1}{2}\frac{d}{dt} \parallel v_1(t) \parallel^2 + a(t; v_1(t), v_1(t)) = - < \frac{dv_2(t)}{dt}, v_1(t) >$$

Using the coercivity of the bilinear form $a(t; \cdot, \cdot)$ and the inequality $pq \leq \frac{p^2}{2} + \frac{q^2}{2}$,

$$\frac{1}{2}\frac{d}{dt} \parallel v_1(t) \parallel^2 + \alpha \parallel v_1(t) \parallel_1^2 \leq - < \frac{dv_2(t)}{dt}, v_1(t) > \leq \frac{\alpha}{2} \parallel v_1(t) \parallel^2 + \frac{1}{2\alpha} \parallel \frac{dv_2(t)}{dt} \parallel^2$$

which gives

$$\frac{1}{2}\frac{d}{dt} \parallel v_1(t) \parallel^2 + \alpha \parallel v_1(t) \parallel_1^2 \leq \frac{\alpha}{2} \parallel v_1(t) \parallel^2 + \frac{1}{2\alpha} \parallel \frac{dv_2(t)}{dt} \parallel^2$$

Since $\parallel v_1(t) \parallel_1^2 \geq c_p \parallel v_1(t) \parallel^2$, the inequality becomes

$$\frac{d}{dt} \parallel v_1(t) \parallel^2 + \alpha c_p \parallel v_1(t) \parallel^2 \leq \frac{1}{\alpha c_p} \parallel \frac{dv_2(t)}{dt} \parallel^2$$

Using Gronwall's Lemma (9) for $v_1(t)$,we obtain that

$$\parallel v_1(t) \parallel^2 \leq \parallel v_1(0) \parallel^2 e^{-\alpha c_p t} + \frac{1}{\alpha c_p} \int_0^t e^{-\alpha c_p (t-\tau)} \parallel \frac{dv_2(\tau)}{d\tau} \parallel^2 d\tau$$

The integral term can be bounded as follows

$$\parallel v_1(t) \parallel^2 \leq \parallel v_1(0) \parallel^2 e^{-\alpha c_p t} + \frac{1 - e^{-\alpha c_p t}}{(\alpha c_p)^2} \sup_{0 \leq \tau \leq t} \parallel \frac{dv_2(\tau)}{d\tau} \parallel^2 \qquad (15)$$

The triangle inequality $\| u(t) - u_h(t) \| \leq \| v_1(t) \| + \| v_2(t) \|$ combined with (15) gives

$$\| u(t) - u_h(t) \| \leq \| v_1(0) \| e^{\frac{-\alpha c_p t}{2}} + (1 + \frac{1}{\alpha c_p}) \sup_{0 \leq \tau \leq t} (\| v_2(\tau) \| + \| \frac{dv_2(\tau)}{d\tau} \|) \quad (16)$$

The term $\| v_1(0) \|$ is bounded in the following way:

$$\| v_1(0) \| = \| u_{0,h} - \Pi_h u_0 \| \leq \| u_{0,h} - u(0) \| + \| u(0) - \Pi_h u(0) \| \quad (17)$$

In (16), $e^{\frac{-\alpha c_p t}{2}} \leq 1$ for all $t \geq 0$. Applying (13), the conclusion of the theorem comes in a straightforward way:

$$\| u(t) - u_h(t) \| \leq \| u(0) - u_{0,h} \| + C_1 h^{r+1} \| u \|_{C^1(0,T;H^{r+1})} \quad (18)$$

□

Fully-discrete approximation

Applying the backward Euler method, the space-time discretization of problem (3) writes as

$$\begin{aligned} \frac{1}{k}(u_h^{n+1} - u_h^n, v_h) + a(t_{n+1}; u_h^{n+1}, v_h) &= (f(t_{n+1}), v_h), \quad for \quad any \quad v_h \in S_h \quad (19) \\ u_h(0) &= u_{0,h} \end{aligned}$$

Here u_h^{n+1}, u_h^n represent the solution of the discretized problem at time $t_{n+1} = k(n+1)$ and $t_n = nk$, respectively, k is the time step.

Theorem 2.1.3. *Assume that the solution u_h of the semi-discretized problem (10) is such that $u_h \in C^2(0,T;L^2(\Omega))$. The solution u_h^n of the fully discrete problem (19) satisfies*

$$\| u_h^n - u_h(t_n) \| \leq C_2 k \left(\int_0^{t_n} \| \frac{\partial^2 u_h(\tau)}{\partial \tau^2} \|^2 \, d\tau \right)^{\frac{1}{2}}$$

at any time t_n.

Proof. The semi-discretized equation (10) can be rewritten as

$$\begin{aligned} \frac{1}{k}(u_h(t_{n+1}) - u_h(t_n), v_h) + a(t_{n+1}; u_h(t_{n+1}), v_h) &= \left(\frac{u_h(t_{n+1}) - u_h(t_n)}{k} - \frac{\partial u_h}{\partial t}(t_{n+1}), v_h \right) \\ &+ (f(t_{n+1}), v_h) \quad (20) \end{aligned}$$

by adding on both sides $\frac{1}{k}(u_h(t_{n+1}) - u_h(t_n), v_h)$.
Given the fact that $u_h \in C^2(0,T;H^{r+1}(\Omega))$, by Taylor's Theorem the first term on the right-hand side is equal to

$$\left(\frac{u_h(t_{n+1}) - u_h(t_n)}{k} - \frac{\partial u_h}{\partial t}(t_{n+1}), v_h\right) = -\frac{1}{k}\left(\int_{t_n}^{t_{n+1}} (\tau - t_n)\frac{\partial^2 u_h}{\partial \tau^2}(\tau)d\tau, v_h\right)$$

Defining $e_h^n := u_h^n - u_h(t_n)$ and subtracting (20) from (19)

$$\frac{1}{k}(e_h^{n+1} - e_h^n, v_h) + a(t_{n+1}, e_h^{n+1}, v_h) = \frac{1}{k}\left(\int_{t_n}^{t_{n+1}} [\tau - t_n]\frac{\partial^2 u_h}{\partial \tau^2}(\tau)d\tau, v_h\right) \qquad (21)$$

for all $v_h \in S_h$.
Replacing v_h with e_h^{n+1}, first we bound the term $\frac{1}{k}\left(\int_{t_n}^{t_{n+1}} [\tau - t_n]\frac{\partial^2 u_h}{\partial \tau^2}(\tau)d\tau, v_h\right)$ using the Jensen's inequality [26],the inequality $pq \leq \frac{p^2}{2} + \frac{q^2}{2}$ and the fact that $|\tau - t_n| \leq k$

$$\begin{aligned}
\frac{1}{k}\left(\int_{t_n}^{t_{n+1}} [\tau - t_n]\frac{\partial^2 u_h(\tau)}{\partial \tau^2}d\tau, e_h^{n+1}\right) &= \frac{1}{k}\int_\Omega \left(\int_{t_n}^{t_{n+1}} [\tau - t_n]\frac{\partial^2 u_h}{\partial \tau^2}(\tau)d\tau\right) e_h^{n+1}dx \\
\leq \int_\Omega \left(|e_h^{n+1}|\int_{t_n}^{t_{n+1}} |\tau - t_n||\frac{\partial^2 u_h}{\partial \tau^2} \mid \frac{d\tau}{k}\right)dx &\leq \parallel e_h^{n+1} \parallel \left(\int_\Omega \left(\int_{t_n}^{t_{n+1}} k|\frac{\partial^2 u_h}{\partial \tau^2}|\frac{d\tau}{k}\right)^2 dx\right)^{\frac{1}{2}} \\
&\leq \frac{\beta^2 \parallel e_h^{n+1} \parallel^2}{2} + \frac{1}{2\beta^2}\int_\Omega \left(\int_{t_n}^{t_{n+1}} k|\frac{\partial^2 u_h}{\partial \tau^2}(\tau) \mid \frac{d\tau}{k}\right)^2 dx \\
&\leq \frac{\beta^2 \parallel e_h^{n+1} \parallel^2}{2} + \frac{k^2}{2\beta^2}\int_\Omega \left(\int_{t_n}^{t_{n+1}} |\frac{\partial^2 u_h}{\partial \tau^2}(\tau) \mid \frac{d\tau}{k}\right)^2 dx \\
&\leq \frac{\beta^2 \parallel e_h^{n+1} \parallel^2}{2} + \frac{k^2}{2\beta^2}\int_\Omega \left(\int_{t_n}^{t_{n+1}} \mid \frac{\partial^2 u_h}{\partial \tau^2}(\tau) \mid^2 \frac{d\tau}{k}\right)dx \\
&\leq \frac{\beta^2 \parallel e_h^{n+1} \parallel^2}{2} + \frac{k}{2\beta^2}\int_{t_n}^{t_{n+1}}\int_\Omega |\frac{\partial^2 u_h}{\partial \tau^2}(\tau) \mid^2 dxd\tau \qquad (22)
\end{aligned}$$

where β is a constant which will be chosen in a suitable way in the following. Returning to (21), we can estimate $\parallel e_h^{n+1} \parallel^2$ from the coercivity of $a(t;\cdot,\cdot)$, the inequality (22) and the equality $a^2 - ab = \frac{a^2}{2} - \frac{b^2}{2} + \frac{1}{2}(a-b)^2$

$$\begin{aligned}
\frac{1}{2k} \parallel e_h^{n+1} \parallel^2 - \frac{1}{2k} \parallel e_h^n \parallel^2 + \frac{1}{2k} \parallel e_h^{n+1} - e_h^n \parallel^2 + \alpha \parallel e_h^{n+1} \parallel_1^2 \\
\leq \frac{\beta^2 \parallel e_h^{n+1} \parallel^2}{2} + \frac{k}{2\beta^2}\int_{t_n}^{t_{n+1}}\int_\Omega |\frac{\partial^2 u_h}{\partial \tau^2}(\tau) \mid^2 dxd\tau \qquad (23)
\end{aligned}$$

But $\| e_h^{n+1} \|^2 \leq \| e_h^{n+1} \|_1^2$ so we obtain

$$\begin{aligned} \| e_h^{n+1} \|^2 &- \| e_h^n \|^2 + \| e_h^{n+1} - e_h^n \|^2 + 2k\alpha \| e_h^{n+1} \|^2 \\ &\leq k\beta^2 \| e_h^{n+1} \|^2 + \frac{k^2}{\beta^2} \int_{t_n}^{t_{n+1}} \int_\Omega | \frac{\partial^2 u_h}{\partial \tau^2}(\tau) |^2 \, dx d\tau \end{aligned} \tag{24}$$

Now we can choose β such that $\beta^2 = 2\alpha$ and the inequality can be simplified to

$$\| e_h^{n+1} \|^2 - \| e_h^n \|^2 \leq \frac{k^2}{2\alpha} \int_{t_n}^{t_{n+1}} \int_\Omega | \frac{\partial^2 u_h}{\partial \tau^2}(\tau) |^2 \, dx d\tau \tag{25}$$

Summing up from e_h^0 to e_h^{n+1} and noticing that $e_h^0 = 0$ we obtain

$$\| e_h^{n+1} \| \leq Ck \left(\int_0^{t_{n+1}} \| \frac{\partial^2 u_h}{\partial \tau^2}(\tau) \|^2 \, d\tau \right)^{\frac{1}{2}}$$

with $C_2 = \frac{1}{2\alpha}$. This is true for all t_{n+1} so we can write

$$\| e_h^n \| \leq C_2 k \left(\int_0^{t_n} \| \frac{\partial^2 u_h}{\partial \tau^2}(\tau) \|^2 \, d\tau \right)^{\frac{1}{2}}$$

□

Theorem 2.1.4. *Let u be the exact solution of (3) such that $u \in C^1(0,T; H^{r+1}(\Omega))$, $r \geq 1$, $u_h \in C^2(0,T; L^2(\Omega))$ solution of the semi-discrete problem (10) and u_h^n the solution of the fully discrete problem (19) at time t_n. If (8) holds, then the error is given by*

$$\| u(t_n) - u_h^n \| \leq \| u_0 - u_{0,h} \| + C_1 h^{r+1} \| u \|_{C^1(0,T;H^{r+1})} + C_2 k \left(\int_0^{t_n} \| \frac{\partial^2 u_h}{\partial \tau^2}(\tau) \|^2 \, d\tau \right)^{\frac{1}{2}} \tag{26}$$

Proof. Combining **Theorem 2.1.2** and **Theorem 2.1.3** we get the result right away. □

2.2 Error estimate for the numerical solution of a time-periodic parabolic problem

In her paper [14], A. Hansbo proved the existence of a time-periodic solution for a linear parabolic equation with a symmetric operator. I will show that her results are

valid in the case of linear parabolic problems with a non-symmetric operator.
We consider the time-periodic parabolic problem

$$\begin{aligned} \frac{\partial u}{\partial t} + Lu &= f \quad in \quad (0,T)\times\Omega \\ u &= 0 \quad on \quad (0,T)\times\partial\Omega \\ u(0) &= u(T) \quad on \quad \Omega \end{aligned} \tag{27}$$

where T is the period and $f \in L^2(0,T;L^2(\Omega))$, f periodic with period T and L is a non-symmetric operator, eventually time-periodic.
The weak formulation of (27) writes as: Find $u \in W(V)$ such that

$$\begin{aligned} \frac{d}{dt} < u, v > + a(t;u,v) &= < f, v >_{V\times V'}, \quad for \quad any \quad v \quad \in V \\ u(0) &= u(T) \end{aligned} \tag{28}$$

where V is the space of test functions. It is assumed that the bilinear form $a(t;u,v) : V \times V \to \mathbb{R}$ is coercive in the Hilbert space V with a constant α and continuous with a constant M, both independent of time, namely

$$a(t;v,v) \geq \alpha \parallel v \parallel_1^2$$

$$a(t;u,v) \leq M \parallel u \parallel_1 \parallel v \parallel_1$$

The initial value problem associated with (28):Given $\phi \in L^2(\Omega)$, find $\widetilde{u} \in W(V)$ at any time t such that

$$\begin{aligned} \frac{d}{dt} < \widetilde{u}, v > + a(t;\widetilde{u},v) &= < f, v > \\ \widetilde{u}(0) &= \phi \end{aligned} \tag{29}$$

The solution can be written as (see [22])

$$\widetilde{u}(t) = E(t,0)\phi + \int_0^t E(t,s)f(s)ds = E(t,0)\phi + g(t) \tag{30}$$

$E(t,\tau)\phi$ is the solution of (29) with $f = 0$ and initial value ϕ given at $t = \tau$. The operator $E(t,\tau) : L^2(\Omega) \to L^2(\Omega)$ has the norm $\parallel \cdot \parallel$ in $L^2(\Omega)$. We will prove that $E(\cdot,\cdot)$ is a contraction.
Let $E(t,0)\phi$ be a solution of (29) with $f = 0$. We can prove the following Lemma

Lemma 2.2.1. $\| E(t,0) \| \leq c < 1$, *for all* $t > 0$.

Proof. We know that $E(t,0)\phi = v(t)$ is a solution of (29) with $f = 0$. Then

$$\frac{d}{dt} < E(t,0)\phi, v > + a(t; E(t,0)\phi, v) = 0$$

Because $a(t;\cdot,\cdot)$ is coercive and $\| \cdot \| \leq \| \cdot \|_1$

$$\frac{1}{2}\frac{d}{dt} \| v(t) \|^2 + \alpha \| v(t) \|^2 \leq \frac{1}{2}\frac{d}{dt} \| v(t) \|^2 + a(t; v(t), v(t)) = 0$$

From the last inequality we obtain that

$$\frac{d}{dt} \| v(t) \|^2 \leq -2\alpha \| v(t) \|^2$$

Applying the Gronwall's Lemma, we obtain:

$$\| v(t) \|^2 \leq e^{-2\alpha t} \| v(0) \|^2$$

In other words we have that

$$\frac{\| v(t) \|^2}{\| \phi \|^2} \leq e^{-2\alpha t} < 1$$

for all $t > 0$, so the operator $E(t,0)$ is a contraction. □

We may represent the solution $w = u(0)$ of the periodic problem at time zero in terms of $E(T,0)$ and g as

$$w = E(T,0)w + g(T) \tag{31}$$

using (30).

By **Lemma 2.2.1**, $E(T,0)$ is a contraction therefore $I - E(T,0)$ is invertible on $L^2(\Omega)$. We know that g is a solution of (29) with initial value $\phi = 0, f \in L^2(0,T; L^2(\Omega))$ implies that $g \in L^2(\Omega)$ and it follows that (31) has a unique solution w. The solution at time t of the periodic problem (27) is the solution of the initial value problem (29) at time t with $\phi = w$.

We define the semi-discrete problem as : Find $u_h \in S_h$, S_h a family of finite-dimensional subspaces $S_h \subset H_0^1$ as defined in (6) , such that

$$\begin{aligned} \frac{d}{dt} < u_h, v_h > + a(t; u_h, v_h) &= < f, v_h > \quad , \quad for \quad any \quad v_h \in S_h \quad and \quad t \in (0, T) \\ u_h(0) &= u_h(T) \end{aligned} \tag{32}$$

We associate to (32) the following problem : Given ϕ_h, find $\widetilde{u}_h \in S_h$ such that

$$\begin{aligned} \frac{d}{dt} < \widetilde{u}_h, v_h > + a(t; \widetilde{u}_h, v_h) &= < f, v_h >, \quad for \quad any \quad t > 0 \quad and \quad any \quad v_h \in S_h \\ \widetilde{u}_h(0) &= \phi_h \end{aligned} \tag{33}$$

Let $E_h(t, \tau) : S_h \to S_h, \quad t \geq \tau$, be the solution operator of the semi-discrete homogeneous equation with initial value given at $t = \tau$. This operator is contraction in $L^2(\Omega)$ with the norm $\| \cdot \|$.
Let $E_h(t, 0)\phi_h$ be the solution at time t of (33) with $f = 0$.

Lemma 2.2.2.

$$\| E_h(t, 0) \| \leq c < 1$$

with c independent of h.

Proof. $E_h(t, 0)\phi_h = v_h(t)$ is a solution of (33) with $f = 0$, then

$$\frac{d}{dt} < E_h(t, 0)\phi_h, v_h > + a(t; E_h(t, 0)\phi_h, v_h) = 0$$

Because $a(t; \cdot, \cdot)$ is coercive and $\| \cdot \| \leq \| \cdot \|_1$

$$\frac{1}{2}\frac{d}{dt} \| v_h(t) \|^2 + \alpha \| v_h(t) \|^2 \leq \frac{1}{2}\frac{d}{dt} \| v_h(t) \|^2 + a(t; v_h(t), v_h(t)) = 0$$

Or

$$\frac{d}{dt} \| v_h(t) \|^2 \leq -2\alpha \| v_h(t) \|^2$$

Using the Gronwall's Lemma, we obtain

$$\| v_h(t) \|^2 \leq e^{-2\alpha t} \| v_h(0) \|^2$$

In other words we have that

$$\frac{\| v_h(t) \|^2}{\| \phi_h \|^2} \leq e^{-2\alpha t} < 1 \tag{34}$$

So, $E_h(t, 0)$ is a contraction. □

This is true for all t. We can prove as in the continuous case that the solution of (33) is the same as the solution of the periodic problem (32), if $\phi_h = u_h(0)$, and that $u_h(0)$ is uniquely defined by $w_h = E_h(T,0)w_h + g_h(T)$, where $g_h(T) = \int_0^T E_h(T,s)f(s)ds$.

Theorem 2.2.3. *Let u and u_h be solutions of (28) and (32), respectively, with $u \in C^1(0,T;H^{r+1}(\Omega))$, $r \geq 1$, then if property (8) holds, we have the following estimation*

$$\| u(t) - u_h(t) \| \leq Ch^{r+1} \| u \|_{C^1(0,T;H^{r+1})}$$

for all $t \leq T$ and C a constant independent of h.

Proof. **Theorem 2.1.2** applied to $u(t)$ and $u_h(t)$ gives

$$\| u(t) - u_h(t) \| \leq \| u(0) - u_h(0) \| + Ch^{r+1} \| u \|_{C^1(0,T;H^{r+1})} \tag{35}$$

What we need is to estimate the first term on the right. This can be written as

$$\| u(0) - u_h(0) \| \leq \| u(0) - \Pi_h u(0) \| + \| \Pi_h u(0) - u_h(0) \| \tag{36}$$

By the approximation assumption (8) on Π_h, we have

$$\| u(0) - \Pi_h u(0) \| \leq \widetilde{C}h^{r+1} \| u \|_{C^1(0,T;H^{r+1})} \tag{37}$$

Let $\widetilde{u}_h(t)$ be the solution of the semi-discrete initial value problem (33) with initial value $\Pi_h(u(0))$ and $E_h = E_h(T,0)$.Then

$$\widetilde{u}_h(T) = E_h \Pi_h u(0) + g_h(T), \text{ where } g_h(T) = \int_0^T E_h(T,s)f(s)ds \tag{38}$$

The solution $w_h = u_h(0)$ of the periodic problem fulfills

$$w_h = E_h(T,0)w_h + g_h(T) = E_h u_h(0) + g_h(T) \tag{39}$$

Subtracting (38) and (39) we get

$$E_h(u_h(0) - \Pi_h u(0)) = u_h(0) - \widetilde{u}_h(T) = (u_h(0) - \Pi_h u(0)) + (\Pi_h u(0) - \widetilde{u}_h(T))$$

E_h is a contraction with $\| E_h \| \leq c < 1$ which gives

$$(I - E_h)(u_h(0) - \Pi_h u(0)) = \widetilde{u}_h(T) - \Pi_h u(0)$$
$$\Rightarrow \| u_h(0) - \Pi_h u(0) \| \leq (1-c)^{-1}(\| \widetilde{u}_h(T) - u(T) \| + \| u(0) - \Pi_h u(0) \|) \qquad (40)$$

But, by **Theorem 2.1.2**

$$\| u(T) - \widetilde{u}_h(T) \| \leq \| u(0) - \Pi_h u(0) \| + Ch^{r+1} \| u \|_{C^1(0,T;H^{r+1})}$$

Using (37) we have that

$$\| u(T) - \widetilde{u}_h(T) \| \leq 2\widetilde{C}h^{r+1} \| u \|_{C^1(0,T;H^{r+1})}$$

which, combined with (40) and (37) gives

$$\| u_h(0) - \Pi_h u(0) \| \leq Ch^{r+1} \| u \|_{C^1(0,T;H^{r+1})}$$

This, together with (35) and (36) gives

$$\| u(t) - u_h(t) \| \leq Ch^{r+1} \| u \|_{C^1(0,T;H^{r+1})}$$

□

We consider the backward Euler fully discrete scheme. Let k be the time step, with $Nk = T$, and U_n the approximation of u in S_h at time $t_n = nk$. The approximation can be written as

$$\begin{aligned} (\frac{U_n - U_{n-1}}{k}, v_h) + a(t_n; U_n, v_h) &= (f(t_n), v_h), \quad n = 1, 2, ..., N \quad for \quad any \quad v_h \in S_h \\ U_0 &= U_N \end{aligned} \qquad (41)$$

The fully discrete scheme for the initial value problem is

$$\begin{aligned} (\frac{\widetilde{U}_n - \widetilde{U}_{n-1}}{k}, v_h) + a(t_n; \widetilde{U}_n, v_h) &= (f(t_n), v_h), \quad v_h \in S_h \\ \widetilde{U}_0 &= \phi_h \end{aligned} \qquad (42)$$

Letting $\bar{E}_{hk}(t) = (I + kA_h(t))^{-1}$, the solution operator of the initial value problem with homogeneous equation is defined by

$$E_{hk}(t_j, t_i) = \bar{E}_{hk}(t_j) \cdot \bar{E}_{hk}(t_{j-1}) \cdot ... \cdot \bar{E}_{hk}(t_{i+1}), \ j > i$$

The solution of the time-periodic problem at time zero satisfies

$$\begin{aligned} U_0 = U_N &= E_{hk}(T,0)U_0 + k\sum_{j=1}^{N} E_{hk}(T,t_j)f(t_j) \\ &= E_{hk}(T,0)U_0 + g_{hk}^N(T) \end{aligned}$$

$E_{hk}(T,0)$ is a contraction in $L^2(\Omega)$ as stated in the following Lemma:

Lemma 2.2.4.

$$\| E_{hk}(T,0) \| \leq e^{-\varepsilon T} < 1. \tag{43}$$

with ε a constant.

For a proof see A.Hansbo [14, page 670].

Theorem 2.2.5. *Let U_n be solution of (41) and u solution of (28) at time t_j. Then, if (8) holds we have the following inequality*

$$\| u(t_j) - U_j \| \leq Ch^{r+1} \| u \|_{C^1(0,T;H^{r+1})} + Ck \left(\int_0^T \| \frac{\partial^2 u_h}{\partial \tau^2}(\tau) \|^2 \, d\tau \right)^{\frac{1}{2}} \tag{44}$$

with $j = 0, 1, ..., N$.

Proof. In a similar manner as in the proof of **Theorem 2.2.3** we apply **Theorem 2.1.4** to U_j and $u(t_j)$ to obtain

$$\| u(t_j) - U_j \| \leq \| u(0) - U_0 \| + Ch^{r+1} \| u \|_{C^1(0,T;H^{r+1})} + Ck \left(\int_0^T \| \frac{\partial^2 u_h}{\partial \tau^2}(\tau) \|^2 \, d\tau \right)^{\frac{1}{2}} \tag{45}$$

What we need is to estimate the first term on the right

$$\| u(0) - U_0 \| \leq \| u(0) - \Pi_h u(0) \| + \| \Pi_h u(0) - U_0 \| \tag{46}$$

By the approximation assumption (8) on Π_h, we have

$$\| u(0) - \Pi_h u(0) \| \leq Ch^{r+1} \| u \|_{C^1(0,T;H^{r+1})} \tag{47}$$

Let $\widetilde{U}_N$ be the solution of (42) with initial value $\Pi_h u(0)$, then

$$\widetilde{U}_N = E_{hk}(T,0)\Pi_h u(0) + g_{hk}^N \tag{48}$$

where $g_{hk}^N = k\sum_{j=1}^N E_{hk}(T,t_j)f(t_j)$.
The solution $w_{hk} = U_0$ of the periodic problem (41) fulfills

$$w_{hk} = E_{hk}(T,0)w_{hk} + g_{hk}^N \tag{49}$$

Subtracting (48) from (49) we get

$$E_{hk}(T,0)(U_0 - \Pi_h u(0)) = U_0 - \widetilde{U}_N = (U_0 - \Pi_h u(0)) + (\Pi_h u(0) - \widetilde{U}_N)$$

$\Rightarrow (I - E_{hk}(T,0))(U_0 - \Pi_h u(0)) = \widetilde{U}_N - \Pi_h u(0)$.
$E_{hk}(T,0)$ is a contraction with $\| E_{hk} \| \leq c < 1$ (by **Lemma 2.2.4**), so

$$\| U_0 - \Pi_h u(0) \| \leq (1-c)^{-1}(\| \widetilde{U}_N - u(T) \| + \| u(0) - \Pi_h u(0) \|) \tag{50}$$

Using **Theorem 2.1.4** and (47)

$$\| \widetilde{U}_N - u(T) \| \leq 2Ch^{r+1} \| u \|_{C^1(0,T;H^{r+1})} + Ck \left(\int_0^T \| \frac{\partial^2 u_h}{\partial \tau^2}(\tau) \|^2 \, d\tau \right)^{\frac{1}{2}}$$

which, combined with (50) and (47) gives

$$\| U_0 - \Pi_h u(0) \| \leq Ch^{r+1} \| u \|_{C^1(0,T;H^{r+1})} + Ck \left(\int_0^T \| \frac{\partial^2 u_h}{\partial \tau^2}(\tau) \|^2 \, d\tau \right)^{\frac{1}{2}} \tag{51}$$

This, together with (45), (47) and (46) gives

$$\| u(t_j) - U_j \| \leq Ch^{r+1} \| u \|_{C^1(0,T;H^{r+1})} + Ck \left(\int_0^T \| \frac{\partial^2 u_h}{\partial \tau^2}(\tau) \|^2 \, d\tau \right)^{\frac{1}{2}}$$

□

2.3 Applications of the general theory to time-periodic parabolic problems

In this section, we present two examples of PDEs, both of them showing some difficulties in handling the variational problem. The advection-diffusion equation is a nice example of a PDE with a non-symmetric operator. The difficulty to treat these

type of problems arises when we try to prove the **Projection Property** (8),which is an important hypothesis in the proofs of Section 2.2, and it is due mainly to the time dependence of the non-symmetric operator, as we shall see. As far as we know, in the literature there are no detailed proofs of (8) for an advection-diffusion operator. The Stokes problem, even though it possesses a symmetric operator, it contains the extra pressure term which forces us to modify the formulation of (8) if we make use of a mixed-formulation.

2.3.1 Application to the advection-diffusion equation

Consider the second order elliptic differential operator L

$$Lw := -\nabla \cdot (\sigma \nabla w) + \nabla \cdot (bw) + a_0 w$$

where $\sigma \in (L^\infty(\Omega))^{d\times d}$, $a_0 \in L^\infty(\Omega)$ and $b \in (C^2([0,T] \times \bar{\Omega}))^d$. We assume that $\frac{1}{2}\nabla \cdot b + a_0 \geq 0$ for all $x \in \Omega$.
L is an elliptic operator, i.e. there exists a constant $\alpha_0 > 0$ such that

$$\sum_{i,j} \sigma_{i,j}(x)\xi_i\xi_j \geq \alpha_0 |\xi|^2$$

for each $\xi \in \mathbb{R}^d$ and any $x \in \Omega$.
For the purpose of our analysis we consider the case of $\| \sigma \|_\infty << \| b \|_{C^2([0,T]\times\bar{\Omega})}$.
We associate to the operator L a **non-symmetric** bilinear form

$$a(t; w, v) := \int_\Omega [(\sigma \nabla w) \cdot \nabla v + (\nabla \cdot (bw))v + a_0 wv]dx \tag{52}$$

With the notations introduced in Section 2.1, let $V = H_0^1(\Omega)$ and $H = L^2(\Omega)$.
To apply the theory of Section 2.1 and Section 2.2 we prove that the bilinear form $a(t; \cdot, \cdot)$ is coercive in the Hilbert space V with a constant α and continuous with a constant M, both independent of time, as in (4) and (5). The coercivity is obtained

easily as follows

$$\begin{aligned} a(t;v,v) &= \int_\Omega [(\sigma\nabla v)\cdot\nabla v + (\nabla\cdot(bv))v + a_0|v|^2]dx \\ &\geq \alpha_0 \parallel \nabla v \parallel^2 + \int_\Omega \left[(\nabla\cdot(bv))v + a_0|v|^2\right] dx \\ &= \alpha_0 \parallel \nabla v \parallel^2 + \int_\Omega \left[|v|^2\nabla\cdot b + \frac{b\cdot\nabla(v^2)}{2} + a_0|v|^2\right] dx \\ &= \alpha_0 \parallel \nabla v \parallel^2 + \int_\Omega \left[\frac{1}{2}\nabla\cdot b + a_0\right] |v|^2 dx + \frac{1}{2}\int_{\partial\Omega} |v|^2 b\cdot n ds \\ &= \alpha_0 \parallel \nabla v \parallel^2 + \int_\Omega \left[\frac{1}{2}\nabla\cdot b + a_0\right] |v|^2 dx \end{aligned}$$

The last equality comes from the fact that $v|_{\partial\Omega} = 0$. Using the hypothesis $\frac{1}{2}\nabla\cdot b + a_0 \geq 0$ and the Poincaré inequality we have that there exist $\alpha > 0$ such that

$$a(t;v,v) \geq \alpha \parallel v \parallel_1^2 \tag{53}$$

Continuity can be obtained easily from the following inequalities

$$\begin{aligned} a(t;u,v) &= \int_\Omega [(\sigma\nabla w)\cdot\nabla v + (\nabla\cdot(bu))v + a_0 uv]dx \\ &\leq \parallel \sigma \parallel_\infty \parallel \nabla u \parallel \parallel \nabla v \parallel + \int_\Omega [(\nabla\cdot b)uv + (b\cdot\nabla u)v]dx + \parallel a_0 \parallel_\infty \parallel u \parallel \parallel v \parallel \\ &\leq max(\parallel \sigma \parallel_\infty, \parallel b \parallel_{C^2([0,T]\times\bar{\Omega})}, \parallel a_0 \parallel_\infty) \parallel u \parallel_1 \parallel v \parallel_1 = M \parallel u \parallel_1 \parallel v \parallel_1 \end{aligned}$$

The weak formulation of the initial value problem (1) reads as follows: Given $f \in L^2(0,T;L^2(\Omega))$ and $u_0 \in L^2(\Omega)$, find $u \in W(V)$, such that

$$\begin{aligned} \frac{d}{dt} < u(t), v >_{V'\times V} + a(t;u(t),v) &= < f(t), v >_{V'\times V} \\ u(0) &= u_0 \end{aligned} \tag{54}$$

Consider now the discretization of the problem (54). We consider a family of finite-dimensional subspaces $S_h \subset V$ with the Lagrange interpolation operator I_h defined as in (6).

For all $t \in [0,T]$ we introduce the projection operator $\Pi_h : V \to S_h$ such that $\Pi_h(w)$ is the solution of (7).

Theorem 2.3.1. *The projection operator* $\Pi_h(w)$ *satisfies*

$$\| w - \Pi_h(w) \|_{C^1(0,T;L^2(\Omega))} + h \| w - \Pi_h(w) \|_{C^1(0,T;H^1(\Omega))} \leq Ch^{r+1} \| w \|_{C^1(0,T;H^{r+1})} \tag{55}$$

Proof. **Part I)** First we prove that

$$h \| w - \Pi_h(w) \|_{C^0(0,T;H^1(\Omega))} \leq \widetilde{C} h^{r+1} \| w \|_{C^1(0,T;H^{r+1})} .$$

Adding and subtracting $a(t; I_h(w), v_h)$ in (7)

$$a(t; w - \Pi_h(w), v_h) = a(t; w - I_h(w), v_h) + a(t; I_h(w) - \Pi_h(w), v_h) = 0$$

which gives

$$a(t; I_h(w) - \Pi_h(w), v_h) = a(t; I_h(w) - w, v_h)$$

Setting $v_h = I_h(w) - \Pi_h(w)$, by the coercivity of $a(t; \cdot, \cdot)$ we get for all time t

$$\begin{aligned} \alpha \| I_h(w) - \Pi_h(w) \|_1^2 &\leq a(t; I_h(w) - \Pi_h(w), I_h(w) - \Pi_h(w)) \\ &= a(t; I_h(w) - w, I_h(w) - \Pi_h(w)) \\ &\leq M \| I_h(w) - w \|_1 \| I_h(w) - \Pi_h(w) \|_1 \end{aligned}$$

The last inequality comes from the continuity of $a(t; \cdot, \cdot)$.
Then we get from (6)

$$\begin{aligned} h \| I_h(w) - \Pi_h(w) \|_{C^0(0,T;H^1(\Omega))} &\leq h \frac{M}{\alpha} \| I_h(w) - w \|_{C^0(0,T;H^1(\Omega))} \\ &\leq C \frac{M}{\alpha} h^{r+1} \| w \|_{C^1(0,T,H^{r+1})} \end{aligned} \tag{56}$$

So from (6) we have that

$$\begin{aligned} h \| w - \Pi_h(w) \|_{C^0(0,T;H^1(\Omega))} &\leq h \| w - I_h(w) \|_{C^0(0,T;H^1(\Omega))} \\ &+ h \| I_h(w) - \Pi_h(w) \|_{C^0(0,T;H^1(\Omega))} \\ &\leq (1 + \frac{M}{\alpha}) C h^{r+1} \| w \|_{C^1(0,T;H^{r+1})} \end{aligned} \tag{57}$$

Part II) We need to prove that

$$\| \Pi_h(w) - w \|_{C^0(0,T;L^2(\Omega))} \leq Ch^{r+1} \| w \|_{C^0(0,T;H^{r+1})} . \tag{58}$$

Using Aubin-Nitsche duality argument as in [35] we consider the auxiliary problem: Given $s \in L^2(\Omega)$ find $\phi(s) \in V$ such that

$$a(t; v, \phi(s)) = (s, v), \quad \text{for all } v \in V \tag{59}$$

Then we can write

$$\| \Pi_h(w) - w \| = \sup_{s \in L^2(\Omega), s \neq 0} \frac{(s, \Pi_h(w) - w)}{\| s \|} = \sup_{s \in L^2(\Omega), s \neq 0} \frac{a(t, \Pi_h(w) - w, \phi(s))}{\| s \|} \tag{60}$$

Let $\phi_h \in S_h$ be such that

$$\| \phi(s) - \phi_h \|_1 = \inf_{v_h \in S_h} \| \phi(s) - v_h \|_1 \leq Ch \| \phi(s) \|_2 \tag{61}$$

From the regularity of $\phi(s)$ (see [35]) we have that

$$\| \phi(s) \|_2 \leq \bar{C} \| s \| \tag{62}$$

Since $\phi_h \in S_h$ we know that $a(t; \Pi_h(w) - w, \phi(s)) = a(t; \Pi_h(w) - w, \phi(s) - \phi_h)$. Then, using (61)

$$a(t; \Pi_h(w) - w, \phi(s) - \phi_h) \leq M \| \Pi_h(w) - w \|_1 \| \phi(s) - \phi_h \|_1 \leq CM \| \Pi_h(w) - w \|_1 \, h \| \phi(s) \|_2 \tag{63}$$

Combining the inequalities (57),(63),(60) and (62) we get

$$\sup_{t \in [0,T]} \| \Pi_h(w) - w \| \leq Ch \| \Pi_h(w) - w \|_{C^0(0,T;H^1(\Omega))} \leq Ch^{r+1} \| w \|_{C^1(0,T;H^{r+1})} \tag{64}$$

So we have that

$$\| \Pi_h(w) - w \|_{C^0(0,T;L^2(\Omega))} \leq Ch^{r+1} \| w \|_{C^1(0,T;H^{r+1})} \tag{65}$$

Part III) The third part of our proof consists in demonstrating that

$$h \| \partial_t(\Pi_h(w)) - \partial_t w \|_{C^0(0,T;H^1(\Omega))} \leq Ch^{r+1} \| w \|_{C^1(0,T;H^{r+1})} . \tag{66}$$

To prove this, we differentiate (7) with respect to t. Using the fact that v_h, σ and a_0 do not depend on time, we have

$$\begin{aligned} \partial_t a(t; \Pi_h(w), v_h) &= a(t; \partial_t(\Pi_h(w)), v_h) + \int_\Omega (\nabla \cdot ((\partial_t b)\Pi_h(w)))v_h dx \\ &= \partial_t a(t; w, v_h) = a(t; \partial_t(w), v_h) + \int_\Omega (\nabla \cdot ((\partial_t b)w))v_h dx \end{aligned}$$

with $b \in (C^2([0,T] \times \bar{\Omega}))^d$. Then we have

$$a(t; \partial_t \Pi_h(w) - \partial_t w, v_h) = \int_\Omega (\nabla \cdot ((\partial_t b)(w - \Pi_h(w)))) \, v_h dx \tag{67}$$

and

$$a(t; \partial_t \Pi_h(w) - \partial_t w, v_h) = a(t; \partial_t \Pi_h(w) - I_h(\partial_t w), v_h) - a(t; \partial_t w - I_h(\partial_t w), v_h)$$

So from the last two equalities we get

$$\begin{aligned} a(t; \partial_t \Pi_h(w) - I_h(\partial_t w), v_h) &= a(t; \partial_t \Pi_h(w) - \partial_t w, v_h) + a(t; \partial_t w - I_h(\partial_t w), v_h) \\ &= \int_\Omega (\nabla \cdot ((\partial_t b)(w - \Pi_h(w)))) \, v_h dx + a(t; \partial_t w - I_h(\partial_t w), v_h) \end{aligned}$$

Let $v_h = \partial_t \Pi_h(w) - I_h(\partial_t w)$ and by the coercivity and continuity of $a(t; \cdot, \cdot)$ we get

$$\begin{aligned} \alpha \parallel \partial_t \Pi_h(w) - I_h(\partial_t w) \parallel_1^2 &\leq a(t; \partial_t w - I_h(\partial_t w), \partial_t \Pi_h(w) - I_h(\partial_t w)) + \\ &+ \int_\Omega (\nabla \cdot ((\partial_t b)(w - \Pi_h(w)))) \, (\partial_t \Pi_h(w) - I_h(\partial_t w)) dx \\ &\leq M \parallel \partial_t w - I_h(\partial_t w) \parallel_1 \parallel \partial_t \Pi_h(w) - I_h(\partial_t w) \parallel_1 + \\ &+ (\parallel b \parallel_{C^2([0,T] \times \bar{\Omega})}) \parallel w - \Pi_h(w) \parallel_1 \parallel \partial_t \Pi_h(w) - I_h(\partial_t w) \parallel_1 \end{aligned}$$

Then from the above inequality and (6) we obtain

$$\begin{aligned} h \parallel \partial_t \Pi_h(w) - I_h(\partial_t w) \parallel_{C^0(0,T,H^1(\Omega))} &\leq h \frac{M}{\alpha} \parallel \partial_t w - I_h(\partial_t w) \parallel_{C^0(0,T;H^1(\Omega))} \\ &+ h \frac{\parallel b \parallel_{C^2(0,T,\bar{\Omega})}}{\alpha} \parallel w - \Pi_h(w) \parallel_{C^0(0,T;H^1(\Omega))} \\ &\leq C h^{r+1} \parallel w \parallel_{C^1(0,T;H^{r+1})} \end{aligned}$$

Then (6) gives

$$\begin{aligned} h \parallel \partial_t w - \partial_t \Pi_h(w) \parallel_{C^0(0,T;H^1(\Omega))} &\leq h \parallel \partial_t w - I_h(\partial_t w) \parallel_{C^0(0,T,H^1(\Omega))} \\ &+ h \parallel I_h(\partial_t w) - \partial_t \Pi_h(w) \parallel_{C^0(0,T;H^1(\Omega))} \\ &\leq C h^{r+1} \parallel w \parallel_{C^1(0,T;H^{r+1})} \end{aligned} \tag{68}$$

Part IV) The last thing left to prove is

$$\parallel \partial_t \Pi_h(w) - \partial_t w) \parallel_{C^0(0,T;L^2(\Omega))} \leq C h^{r+1} \parallel w \parallel_{C^1(0,T;H^{r+1})} . \tag{69}$$

Using an Aubin-Nitsche duality argument as before, we consider the auxiliary problem: Given $s \in L^2(\Omega)$ find $\phi(s) \in V$ such that

$$a(t; v, \phi(s)) = (s, v), \quad \text{for all } v \in V \tag{70}$$

This is true also if we replace v by $\partial_t v$ with $v \in C^1(0, T; V)$:

$$a(t; \partial_t v, \phi(s)) = (s, \partial_t v)$$

Then we can write

$$\begin{aligned} \| \partial_t \Pi_h(w) - \partial_t w \| &= \sup_{s \in L^2(\Omega), s \neq 0} \frac{(s, \partial_t \Pi_h(w) - \partial_t w)}{\| s \|} \\ &= \sup_{s \in L^2(\Omega), s \neq 0} \frac{a(t, \partial_t \Pi_h(w) - \partial_t w, \phi(s))}{\| s \|} \end{aligned} \tag{71}$$

Let $\phi_h \in S_h$ be such that

$$\| \phi(s) - \phi_h \|_1 = \inf_{v_h \in S_h} \| \phi(s) - v_h \|_1 \leq Ch \| \phi(s) \|_2 \tag{72}$$

with $\phi(s)$ satisfying the regularity argument

$$\| \phi(s) \|_2 \leq \bar{C} \| s \| \tag{73}$$

Since $\phi_h \in S_h$ the following holds

$$\begin{aligned} a(t; \partial_t \Pi_h(w) - \partial_t w, \phi(s)) &= a(t; \partial_t \Pi_h(w) - \partial_t w, \phi(s) - \phi_h) + a(t; \partial_t \Pi_h(w) - \partial_t w, \phi_h) \\ &= a(t; \partial_t \Pi_h(w) - \partial_t w, \phi(s) - \phi_h) + \int_\Omega \nabla \cdot ((\partial_t b)(w - \Pi_h(w)))\phi_h dx \end{aligned}$$

where the last equality comes from (67). Then using the continuity of $a(t; \cdot, \cdot)$

$$\begin{aligned} a(t, \partial_t \Pi_h(w) - \partial_t w, \phi(s) - \phi_h) &+ \int_\Omega \nabla \cdot ((\partial_t b)(\Pi_h(w) - w))(\phi(s) - \phi_h) dx \\ - \int_\Omega \nabla \cdot ((\partial_t b)(\Pi_h(w) - w))\phi(s) dx &\leq M \| \partial_t \Pi_h(w) - \partial_t w \|_1 \| \phi(s) - \phi_h \|_1 \\ + \int_\Omega \nabla \cdot ((\partial_t b)(\Pi_h(w) - w))(\phi(s) - \phi_h) dx &- \int_\Omega \nabla \cdot ((\partial_t b)(\Pi_h(w) - w))\phi(s) dx \end{aligned} \tag{74}$$

Using (72), the second term at the right is bounded as follows

$$\begin{aligned}
&\int_\Omega \nabla\cdot((\partial_t b)(\Pi_h(w)-w))(\phi(s)-\phi_h)dx\\
=\;&\int_\Omega(\nabla\cdot\partial_t b)(\Pi_h(w)-w)(\phi(s)-\phi_h)dx+\int_\Omega \partial_t b\cdot\nabla(\Pi_h(w)-w)(\phi(s)-\phi_h)dx\\
\le\;&\parallel b\parallel_{C^2(0,T;\bar\Omega)}\parallel \Pi_h(w)-w\parallel\parallel \phi(s)-\phi_h\parallel+\parallel b\parallel_{C^2(0,T;\bar\Omega)}\parallel \Pi_h(w)-w\parallel_1\parallel \phi(s)-\phi_h\parallel\\
\le\;&\parallel b\parallel_{C^2(0,T;\bar\Omega)}\parallel \Pi_h(w)-w\parallel\parallel \phi(s)-\phi_h\parallel_1+\parallel b\parallel_{C^2(0,T;\bar\Omega)}\parallel \Pi_h(w)-w\parallel_1\parallel \phi(s)-\phi_h\parallel_1\\
\le\;&\parallel b\parallel_{C^2(0,T;\bar\Omega)}\parallel \Pi_h(w)-w\parallel h\parallel \phi(s)\parallel_2+\parallel b\parallel_{C^2(0,T;\bar\Omega)}\parallel \Pi_h(w)-w\parallel_1 h\parallel \phi(s)\parallel_2
\end{aligned}$$

From (73) we obtain

$$\begin{aligned}
&\int_\Omega \nabla\cdot((\partial_t b)(\Pi_h(w)-w))(\phi(s)-\phi_h)dx\le C\parallel b\parallel_{C^2(0,T;H^1(\Omega))}\parallel \Pi_h(w)-w\parallel_1 h\parallel \phi(s)\parallel_2\\
\le\;&\bar C\parallel b\parallel_{C^2(0,T;\bar\Omega)}\parallel \Pi_h(w)-w\parallel_1 h\parallel s\parallel \qquad (75)
\end{aligned}$$

The last term can be bounded in a similar way

$$\begin{aligned}
-\;&\int_\Omega \nabla\cdot((\partial_t b)(\Pi_h(w)-w))\phi(s)dx\\
=\;&\int_\Omega(\partial_t b)(\Pi_h(w)-w)\nabla(\phi(s))dx-\int_{\partial\Omega}(\partial_t b\cdot n)(\Pi_h(w)-w)\phi(s)ds \qquad (76)
\end{aligned}$$

The term $\Pi_h(w)-w\in H_0^1(\Omega)$ which means that $(\Pi_h(w)-w)|_{\partial\Omega}=0$. This gives

$$\begin{aligned}
-\;&\int_\Omega(\partial_t b)(\Pi_h(w)-w)\nabla(\phi(s))dx\le\parallel b\parallel_{C^2(0,T;\bar\Omega)}\parallel \Pi_h(w)-w\parallel\parallel \phi(s)\parallel_1\\
\le\;&\parallel b\parallel_{C^2(0,T;\bar\Omega)}\parallel \Pi_h(w)-w\parallel\parallel \phi(s)\parallel_2\le\bar C\parallel \Pi_h(w)-w\parallel\parallel s\parallel \qquad (77)
\end{aligned}$$

where the last inequality comes from the regularity estimate (73) of $\phi(s)$.
Using the estimates (74), (75) and (77) we can estimate (71)

$$\begin{aligned}
\parallel \partial_t\Pi_h(w)-\partial_t w\parallel\;&=\;\sup_{s\in L^2(\Omega),s\neq 0}\frac{a(t;\partial_t\Pi_h(w)-\partial_t w,\phi(s))}{\parallel s\parallel}\\
&\le\;\sup_{s\in L^2(\Omega),s\neq 0}\frac{M\parallel \partial_t\Pi_h(w)-\partial_t w\parallel_1\parallel \phi(s)-\phi_h\parallel_1}{\parallel s\parallel}\\
&+\;\sup_{s\in L^2(\Omega),s\neq 0}\frac{\bar C\parallel b\parallel_{C^2(0,T;H^1(\Omega))}h\parallel \Pi_h(w)-w\parallel_1\parallel s\parallel}{\parallel s\parallel}\\
&+\;\sup_{s\in L^2(\Omega),s\neq 0}\frac{\bar C\parallel \Pi_h(w)-w\parallel\parallel s\parallel}{\parallel s\parallel}
\end{aligned}$$

Combining the inequalities (68), (73), (72) and the estimates for $\| \Pi_h(w) - w \|$, $\| \Pi_h(w) - w \|_1$ we obtain

$$\sup_{t\in[0,T]} \| \partial_t \Pi_h(w) - \partial_t w \| \leq C h^{r+1} \| w \|_{C^1(0,T;H^{r+1})} \tag{78}$$

So we have that

$$\| \partial_t \Pi_h(w) - \partial_t w \|_{C^0(0,T;L^2(\Omega))} \leq C h^{r+1} \| w \|_{C^1(0,T;H^{r+1})} \tag{79}$$

(57), (65), (68) together with (79) proves that

$$\| w - \Pi_h(w) \|_{C^1(0,T;L^2(\Omega))} + h \| w - \Pi_h(w) \|_{C^1(0,T;H^1(\Omega))} \leq C h^{r+1} \| w \|_{C^1(0,T;H^{r+1})}$$

□

With the **Projection-Property**(8) proven, the general theory of Section 2.2 directly applies. The coercivity constant α depends on the diffusion coefficient, σ. The operators $E(\cdot,\cdot)$, $E_h(\cdot,\cdot)$ and $E_{hk}(\cdot,\cdot)$ are contractions if $\sigma > 0$. In the case of pure advection the results obtained before do not apply.

In particular, if $b(t)$ and $f(t)$ are time periodic, the solution of the continuous semi-discrete and discrete problem are time periodic and any initial solution is attracted to the periodic solution. Moreover, from **Theorem 2.2.5**, the solution of the time-periodic discrete problem is at most at a distance of $O(k + h^{r+1})$ from the solution of the continuous time-periodic problem.

The error estimate obtained in **Theorem 2.2.3** holds for a Galerkin method provided the space step h is sufficiently smaller than the diffusion coefficient σ. If this is not the case a stable Petrov-Galerkin method must be used, but the above analysis and conclusions are expected to also hold in that latter case as Galerkin formulations are often stabilized by the addition of positive terms, increasing the coercivity constant α.

So far, we have used homogeneous Dirichlet boundary conditions. The results are true in the case of non-homogeneous boundary conditions if we extend the function on the boundary to the whole domain and then transform the problem into one with homogeneous boundary conditions.

2.3.2 Application to the Stokes problem

The Stokes problem has a more complex variational form because of the extra pressure term which involves no second order derivative in space and no time derivative for that variable. The error-estimates will depend on both the velocity and the pressure as we shall see.

Let Ω be an open, bounded Lipschtiz set in $\mathbb{R}^d$. The Stokes problem is defined by: Find a vector function

$$u = \{u_1, u_2, ..., u_d\} : [0,T] \times \Omega \to \mathbb{R}^d$$

and a scalar function

$$p : [0,T] \times \Omega \to \mathbb{R},$$

respectively equal to the velocity of the fluid and its pressure, such that

$$\begin{aligned} \frac{\partial u}{\partial t} - \nu \Delta u + \nabla p &= f \quad in \quad]0,T[\times\Omega & (80)\\ \nabla \cdot u &= 0 \quad in \quad]0,T[\times\Omega & (81)\\ u &= 0 \quad in \quad]0,T[\times\partial\Omega \\ u(x,0) &= u_0 \quad in \quad \Omega \end{aligned}$$

where the vector functions f and u_0 are given, f defined on $[0,T] \times \Omega$, u_0 defined on Ω. We define the following spaces

$$\mathscr{V} := \quad \{u \in \mathscr{D}^d, \quad \nabla \cdot u = 0\} \tag{82}$$

$$V := the \quad closure \quad of \quad \mathscr{V} \quad in \quad (H_0^1(\Omega))^d \tag{83}$$

$$H := the \quad closure \quad of \quad \mathscr{V} \quad in \quad (L^2(\Omega))^d \tag{84}$$

The space V is equipped with the norm of $(H_0^1(\Omega))^d$ denoted by $\| \cdot \|_1$. V is a Hilbert space with the scalar product

$$((u,v)) := \sum_{i=1}^{d} (D_i u, D_i v)_{(H_0^1(\Omega))^d} \tag{85}$$

The space H has the norm of $(L^2(\Omega))^d$ denoted by $\| \cdot \|$.

The space V is contained in H, and the injection is continuous. Let V' and H' denote

the dual spaces of V and H respectively. By the Riesz representation theorem, we can identify H and H' so we have the following inclusions

$$V \hookrightarrow H \equiv H' \hookrightarrow V'$$

We define the following bilinear form:
$a : (H_0^1(\Omega))^d \times (H_0^1(\Omega))^d \to \mathbb{R}$

$$a(u, v) := \nu((u, v)) \tag{86}$$

In addition to the bilinear form $a(\cdot, \cdot)$ defined above we introduce the following Hilbert space $L_0^2(\Omega)$ where

$$L_0^2(\Omega) := \{q \in L^2(\Omega) | \int_\Omega q = 0\} \tag{87}$$

and b a bilinear form such that $b : (H_0^1(\Omega))^d \times L_0^2(\Omega) \to \mathbb{R}$

$$b(v, p) := -(\nabla \cdot v, p) \tag{88}$$

Obviously $a(\cdot, \cdot)$ is coercive with a coercivity constant α and it is continuous with a continuity constant M. Also the bilinear form $b(\cdot, \cdot)$ satisfies the following inequality

$$|b(v, p)| \leq \bar{M} \parallel v \parallel_1 \parallel p \parallel \tag{89}$$

where $\bar{M}$ is a constant.
Then the weak **mixed-formulation** writes as : for $f \in L^2(0, T; (L^2(\Omega))^d$ and $u_0 \in H$, find $u \in L^2(0, T; (H_0^1(\Omega))^d) \cap L^\infty(0, T; H)$ and $p \in L^2(0, T; L_0^2(\Omega))$ such that

$$\begin{aligned} \frac{d}{dt} < u, v > + a(u, v) + b(v, p) &= < f, v >, \quad for \quad any \quad v \in (H_0^1(\Omega))^d \\ b(u, q) &= 0, \quad for \quad any \quad q \in L_0^2(\Omega) \\ u(0) &= u_0 \end{aligned} \tag{90}$$

Problem (90) admits a unique solution. For a proof, see [9, page 302].
We consider the spatial approximation of the Stokes problem: Let $(S_h)_{h>0}$ and $(Q_h)_{h>0}$ be two families of finite element spaces. Suppose that the couple (S_h, Q_h) are

uniformly compatible in the sense that they satisfy the Brezzi-Babuska-Ladyshenskaya condition, i.e. there exists a constant $\beta > 0$ independent of h such that

$$inf_{q_h \in Q_h} \sup_{v_h \in S_h} \frac{\int_\Omega q_h \nabla \cdot v_h}{\| v_h \|_1 \| q_h \|} \geq \beta \tag{91}$$

We suppose that S_h and Q_h satisfy the interpolation property, namely that there exists a constant $r \geq 1$ such that for all $w \in (H^{r+1}(\Omega))^d$ and $q \in H^r(\Omega) \cap Q$ there exist interpolation operators I_h and Q_h that satisfy

$$\| w - I_h(w) \|_{C^1(0,T;(L^2(\Omega))^d)} + h \| w - I_h(w) \|_{C^1(0,T;(H^1(\Omega))^d)} \leq Ch^{r+1} \| w \|_{C^1(0,T;(H^{r+1}(\Omega))^d)} \tag{92}$$

and

$$\| q - Q_h(q) \|_{C^1(0,T;L^2(\Omega))} \leq Ch^r \| q \|_{C^1(0,T;H^r(\Omega))} \tag{93}$$

We introduce the elliptic projections as in [9, page 304]: For all $t \in [0,T]$ fixed, $u(t) \in (H_0^1(\Omega))^d$ and $p(t) \in Q$ we define $\Pi_h(w) \in S_h$ and $\rho_h(p) \in Q_h$ such that

$$\begin{aligned} a(\Pi_h(w), v_h) + b(v_h, \rho_h(p)) &= a(w, v_h) + b(v_h, p), \quad for \quad any \quad v_h \in S_h \\ b(\Pi_h(w), q_h) &= b(w, q_h) \quad for \quad any \quad q_h \in Q_h \end{aligned} \tag{94}$$

Then we can prove the following theorem, given in [9] (without demonstration):

Theorem 2.3.2. *If (w,p) are such that $w \in C^1(0,T;(H^{r+1}(\Omega))^d)$ and $p \in C^1(0,T;H^r(\Omega))$ then*

$$\begin{aligned} \| w - \Pi_h(w) \|_{C^1(0,T;(L^2(\Omega))^d)} &\leq Ch^{r+1}(\| w \|_{C^1(0,T;(H^{r+1}(\Omega))^d)} + \| p \|_{C^1(0,T;H^r(\Omega))}) \\ \| w - \Pi_h(w) \|_{C^1(0,T;(H^1(\Omega))^d)} &+ \| p - \rho_h(p) \|_{C^1(0,T;L^2(\Omega))} \leq Ch^r(\| w \|_{C^1(0,T;(H^{r+1}(\Omega))^d)} \\ &+ \| p \|_{C^1(0,T;H^r(\Omega))}) \end{aligned} \tag{95}$$

From now on, to make the calculations clearer we shall define
$c(w,p) := \| w \|_{C^1(0,T;(H^{r+1}(\Omega))^d)} + \| p \|_{C^1(0,T;H^r(\Omega)}$.

Proof. Adding and subtracting $a(I_h(w), v_h)$ and $b(v_h, Q_h(p))$in the first equation of (94) we get

$$a(\Pi_h(w) - I_h(w), v_h) + b(v_h, \rho_h(p) - Q_h(p)) = a(w - I_h(w), v_h) + b(v_h, p - Q_h(p))$$

If we substitute $v_h = \Pi_h(w) - I_h(w)$ in the above equation and use the continuity and coercivity property of $a(\cdot,\cdot)$ the following inequality holds

$$\begin{aligned} \alpha \quad & \| I_h(w) - \Pi_h(w) \|_1^2 + b(\Pi_h(w) - I_h(w), \rho_h(p) - Q_h(p)) \\ \leq M \quad & \| I_h(w) - w \|_1 \| I_h(w) - \Pi_h(w) \|_1 + b(\Pi_h(w) - I_h(w), p - Q_h(p)) \end{aligned} \tag{96}$$

Using a similar argument as in [9, page 104] and the continuity of $b(\cdot,\cdot)$, the inequality (96) becomes

$$\begin{aligned} \alpha \quad & \| \Pi_h(w) - I_h(w) \|_1^2 + \beta \| \Pi_h(w) - I_h(w) \|_1 \| Q_h(p) - \rho_h(p) \| \\ \leq \quad & C(\| w - I_h(w) \|_1 \| \Pi_h(w) - I_h(w) \|_1 + \| \Pi_h(w) - I_h(w) \|_1 \| p - Q_h(p) \|) \end{aligned} \tag{97}$$

From (92) and (93) we obtain the following result

$$min(\alpha,\beta)(\| \Pi_h(w) - I_h(w) \|_1 + \| \rho_h(p) - Q_h(p) \|) \leq Ch^r(\| w \|_{(H^{r+1}(\Omega))^d} + \| p \|_{H^r(\Omega)})$$

This gives

$$\begin{aligned} \| w - \Pi_h(w) \|_{C^0(0,T;(H^1(\Omega))^d)} \quad + \quad & \| p - \rho_h(p) \|_{C^0(0,T;L^2(\Omega))} \\ \leq \quad & \widetilde{C}h^r(\| w \|_{C^0(0,T;(H^{r+1}(\Omega))^d)} + \| p \|_{C^0(0,T;H^r(\Omega))}) \end{aligned} \tag{98}$$

In a similar way we obtain the estimate on the derivative. Taking the partial derivative in time in the first equation of (94) the following equality is obtained

$$a(\partial_t \Pi_h(w), v_h) + b(v_h, \partial_t \rho_h(p)) = a(\partial_t w, v_h) + b(v_h, \partial_t p) \tag{99}$$

With the same kind of arguments as before we have the following estimate for the partial derivatives

$$\begin{aligned} \| \partial_t w - \partial_t \Pi_h(w) \|_{C^0(0,T;(H^1(\Omega))^d)} \quad + \quad & \| \partial_t p - \partial_t \rho_h(p) \|_{C^0(0,T;L^2(\Omega))} \\ \leq \quad & \widetilde{C}h^r(\| \partial_t w \|_{C^0(0,T;(H^{r+1}(\Omega))^d)} + \| \partial_t p \|_{C^0(0,T;H^r(\Omega))}) \end{aligned} \tag{100}$$

Combining (98) and (100) the second inequality of the theorem is proved

$$\begin{aligned} \| w - \Pi_h(w) \|_{C^1(0,T;(H^1(\Omega))^d)} \quad + \quad & \| p - \rho_h \|_{C^1(0,T;L^2(\Omega))} \\ \leq Ch^r(\| w - \Pi_h(w) \|_{C^1(0,T;(H^1(\Omega))^d)} \quad + \quad & \| q \|_{C^1(0,T;H^r(\Omega))}) \end{aligned} \tag{101}$$

To prove the first inequality we need to use an Aubin-Nitsche argument: Given $s \in (L^2(\Omega))^d$ find $\phi(s) \in V$ such that

$$a(v, \phi(s)) = (s, v) \text{ for all } v \in V \tag{102}$$

The definition of the projection operator(94) gives

$$\begin{aligned} \| \quad & w - \Pi_h(w) \| = \\ = \quad & \sup_{s \in (L^2(\Omega))^d, s \neq 0} \frac{a(w - \Pi_h(w), \phi(s))}{\| s \|} \\ = \quad & \sup_{s \in (L^2(\Omega))^d, s \neq 0} \frac{a(w - \Pi_h(w), \phi(s) - \phi_h) + a(w - \Pi_h(w), \phi_h)}{\| s \|} \\ = \quad & \sup_{s \in (L^2(\Omega))^d, s \neq 0} \frac{a(w - \Pi_h(w), \phi(s) - \phi_h) + b(\phi_h, \rho_h(p) - p)}{\| s \|} \end{aligned} \tag{103}$$

The term involving the bilinear operator $b(\cdot, \cdot)$ requires extra care, as follows

$$\begin{aligned} & \sup \quad_{s \in (L^2(\Omega))^d, s \neq 0} \frac{b(\phi_h, \rho_h(p) - p)}{\| s \|} \\ & = \quad \sup_{s \in (L^2(\Omega))^d, s \neq 0} \frac{b(\phi_h - \phi(s), \rho_h(p) - p) + b(\phi(s), \rho_h(p) - p)}{\| s \|} \end{aligned} \tag{104}$$

Because $\phi(s) \in V$, then the last term is $b(\phi(s), \rho_h(p) - p) = 0$. Using the continuity of $a(\cdot, \cdot)$ and $b(\cdot, \cdot)$, and the regularity argument as in (72) we obtain

$$\begin{aligned} \| \quad & w - \Pi_h(w) \| \\ \leq \quad & \sup_{s \in (L^2(\Omega))^d, s \neq 0} \frac{M \| w - \Pi_h(w) \|_1 \| \phi(s) - \phi_h \|_1 + \bar{M} \| \phi_h - \phi(s) \|_1 \| \rho_h(p) - p \|}{\| s \|} \\ \leq \quad & \sup_{s \in (L^2(\Omega))^d, s \neq 0} \left(\frac{M \| w - \Pi_h(w) \|_1 Ch \| \phi(s) \|_2}{\| s \|} + \frac{\bar{M} h \| \phi(s) \|_2 \| p - \rho_h(p) \|_{C^0(0,T;L^2(\Omega))}}{\| s \|} \right) \\ \leq \quad & \widetilde{C} h (\| w - \Pi_h(w) \|_{C^0(0,T;H^1(\Omega)^d)} + \| p - \rho_h(p) \|_{C^0(0,T;L^2(\Omega))}) \end{aligned} \tag{105}$$

So from (98) and (105) the following inequality is obtained

$$\| w - \Pi_h(w) \|_{C^0(0,T;(L^2(\Omega))^d)} \leq C h^{r+1} c(w, p) \tag{106}$$

In a similar way we can approximate the time derivative

$$\| \partial_t w - \partial_t \Pi_h(w) \|_{C^0(0,T;(L^2(\Omega))^d)} \leq C h^{r+1} c(w, p) \tag{107}$$

Then, (106) together with (107) gives

$$\| w - \Pi_h(w) \|_{C^1(0,T;(L^2(\Omega))^d)} \leq Ch^{r+1}c(w,p)$$

So the first inequality of the theorem is proven. □

Space-approximation Let

$$V_h := \{v_h \in S_h | b(v_h, q_h) = 0, \text{ for all } q_h \in Q_h\}$$

We approximate (90) as follows: Find $u_h \in C^1(0,T;S_h)$ and $p_h \in C^0(0,T;Q_h)$ such that

$$\begin{aligned} \frac{d}{dt} < u_h, v_h > + a(u_h, v_h) + b(v_h, p_h) &= < f, v_h > \text{ for all } v_h \in S_h \\ b(u_h, q_h) &= 0 \text{ for all } q_h \in Q_h \\ u_h(0) &= u_{0h} \end{aligned} \tag{108}$$

with $u_{0h} \in V_h$. The velocities u and u_h satisfy the following theorem:

Theorem 2.3.3. *The solutions u of (90) and u_h of (108), with $u \in C^1(0,T;(H^{r+1}(\Omega))^d)$, satisfy*

$$\| u(t) - u_h(t) \|_{C^0(0,T;(L^2(\Omega))^d)} \leq \| u_0 - u_{0h} \| + Ch^{r+1}c(u(t), p(t)) \tag{109}$$

Proof. For all $t \in [0,T]$, $u(t) \in (H_0^1(\Omega))^d$ and $p(t) \in L_0^2(\Omega)$, let $\Pi_h(u) \in S_h$ and $\rho_h(p) \in Q_h$ be the projection defined in (94). We can write $u_h(t) - u(t) = v_1(t) + v_2(t)$ such that $v_1(t) := u_h(t) - \Pi_h(u(t))$ and $v_2(t) := \Pi_h(u(t)) - u(t)$. Also we introduce the following notation $\delta(t) := p_h - \rho_h(p)$ corresponding to the pressure.
v_2 can be bounded using the inequality (95) on the projection operator

$$\sup_{0 \leq \tau \leq T} (\| v_2(\tau) \| + \| \frac{\partial v_2(\tau)}{\partial \tau} \|) \leq Ch^{r+1}c(u,p) \tag{110}$$

The next step is to bound $\| v_1(t) \|$. We subtract (90) from (108) to obtain

$$\frac{d}{dt} < u_h(t) - u(t), v_h > + a(u_h(t) - u, v_h) + b(v_h, p_h(t) - p(t)) = 0 \tag{111}$$

From the definition of the projection operators (94), the definition of $v_1(t)$, the definition of $\delta(t)$ and the use of (111) we have that

$$\begin{aligned}
< \frac{dv_1}{dt}(t), v_h > \; + \; & a(v_1(t), v_h) + b(v_h, \delta(t)) \\
= \; & < \frac{du_h}{dt}(t), v_h > + a(u_h(t), v_h) + b(v_h, p_h(t)) \\
- \; & < \frac{d\Pi_h(u(t))}{dt}, v_h > - a(\Pi_h(u(t)), v_h) - b(v_h, \rho_h(p(t))) \\
= \; & < \frac{du_h(t)}{dt}, v_h > + a(u_h(t), v_h) + b(v_h, p_h(t)) \\
- \; & < \frac{d\Pi_h(u(t))}{dt}, v_h > - a(u(t), v_h) - b(v_h, p(t)) \\
= \; & < \frac{du_h(t)}{dt}, v_h > - < \frac{d\Pi_h(u(t))}{dt}, v_h > - \frac{d}{dt} < u_h(t) - u(t), v_h > \\
= \; & < \frac{du(t)}{dt}, v_h > - < \frac{d\Pi_h(u(t))}{dt}, v_h > = < -\frac{dv_2(t)}{dt}, v_h > \qquad (112)
\end{aligned}$$

Choosing $v_h = v_1(t)$ from the last equality (112)

$$\frac{1}{2} \parallel v_1(t) \parallel^2 + a(v_1(t), v_1(t)) + b(v_1(t), \delta) = - < \frac{dv_2(t)}{dt}, v_1 > \qquad (113)$$

We know that $b(\Pi_h u(t), q_h) = b(u(t), q_h)$, from the definition of the projection operator (94). We have that $b(\Pi_h u(t), q_h) = 0$ because $b(u(t), q_h) = 0$, for all $u(t)$ solution of the Stokes problem. Also, for all $u(t) \in V$, $b(u(t), q_h) = 0$ is true and $b(u_h(t), q_h) = 0$ for all $u_h(t) \in V_h$. From here we can conclude that $b(v_1, q_h) = 0$, so $b(v_1, \delta(t)) = 0$. The rest of the proof follows the same steps as in **Theorem 2.1.2** and the error estimate for the semi-discrete problem is obtained. □

Fully-discrete problem Applying the backward Euler method, the space-time discretization of the Stokes problem writes as: Find $u_h^{n+1} \in S_h$, $p_h^{n+1} \in Q_h$ such that

$$\begin{aligned}
\frac{1}{k}(u_h^{n+1} - u_h^n, v_h) + a(u_h^{n+1}, v_h) + b(v_h, p_h^{n+1}) &= (f(t_{n+1}), v_h), \quad for \quad any \quad v_h \in S_h \\
b(u_h^{n+1}, q_h) &= 0, \quad for \quad any \quad q_h \in Q_h \\
u_h^0 &= u_{0,h} \qquad (114)
\end{aligned}$$

u_h^0 given in V_h.

Here u_h^{n+1}, p_h^{n+1} and u_h^n represent the solution of the discretized problem at time $t_{n+1} = k(n+1)$ and $t_n = nk$, respectively, k is the time step.

Theorem 2.3.4. *Assume that any solution u_h of the semi-discrete problem (108) is such that $u_h \in C^2(0,T;(L^2(\Omega))^d)$. The solution u_h^n of the fully discrete problem (114) and u_h satisfy*

$$\| u_h^n - u_h(t_n) \| \leq Ck \left(\int_0^{t_n} \| \frac{\partial^2 u_h(\tau)}{\partial \tau^2} \|^2 \, d\tau \right)^{\frac{1}{2}}$$

at any time t_n.

Proof. The semi-discretized equation (108) reads as

$$\begin{aligned} \frac{1}{k}(u_h(t_{n+1}) - u_h(t_n), v_h) \quad &+ \quad a(u_h(t_{n+1}), v_h) + b(v_h, p_h(t_{n+1})) = \\ (\frac{u_h(t_{n+1}) - u_h(t_n)}{k} \quad &- \quad \frac{\partial u_h}{\partial t}(t_{n+1}), v_h) + (f(t_{n+1}), v_h) \end{aligned} \tag{115}$$

Given the fact that $u \in C^2(0,T;H^{r+1}(\Omega))$, by the Taylor Theorem the first term on the right-hand side is equal to

$$\left(\frac{u_h(t_{n+1}) - u_h(t_n)}{k} - \frac{\partial u_h}{\partial t}(t_{n+1}), v_h \right) = -\frac{1}{k} \left(\int_{t_n}^{t_{n+1}} (\tau - t_n) \frac{\partial^2 u_h}{\partial \tau^2}(\tau) d\tau, v_h \right)$$

Defining $e_h^n := u_h^n - u_h(t_n)$ and subtracting (115) from (114)

$$\frac{1}{k}(e_h^{n+1} - e_h^n, v_h) + a(e_h^{n+1}, v_h) + b(v_h, p_h^{n+1} - p_h(t_{n+1})) = \frac{1}{k} \left(\int_{t_n}^{t_{n+1}} [\tau - t_n] \frac{\partial^2 u_h}{\partial \tau^2}(\tau) d\tau, v_h \right) \tag{116}$$

for all $v_h \in S_h$.If we set $v_h = e_h^{n+1}$ then $b(e_h^{n+1}, q_h) = 0$ for all $q_h \in Q_h$ so we can obtain an estimate of the velocity independent of the pressure. Then, the rest of the proof can be carried out with the same arguments as in **Theorem 2.1.3**. □

Time-periodic Stokes problem The problem writes as : Given f a time periodic function with period T, find $u(x,t)$ and $p(x,t)$ such that

$$\begin{aligned} \frac{\partial u}{\partial t} - \nu \Delta u + \nabla p &= f \quad in \quad]0,T[\times\Omega \\ \nabla \cdot u &= 0 \quad in \quad]0,T[\times\Omega \\ u &= 0 \quad in \quad]0,T[\times\partial\Omega \\ u(x,0) &= u(x,T) \quad in \quad \Omega \end{aligned} \tag{117}$$

The weak formulation of (117) writes as: Given $f \in L^2(0,T;(L^2(\Omega))^d)$, find $u \in L^2(0,T;(H_0^1(\Omega))^d) \cap L^\infty(0,T;H)$ and $p \in L^2(0,T;L_0^2(\Omega))$ such that

$$\begin{aligned} \frac{d}{dt} < u, v > + a(u,v) + b(v,p) &= < f, v > \quad for \quad any \quad v \in (H_0^1(\Omega))^d \quad (118) \\ b(u,q) &= 0, \quad for \quad any \quad q \in L_0^2(\Omega) \\ u(0) &= u(T) \end{aligned}$$

The initial value problem associated to (118) is :Given $\phi \in L^2(\Omega)$ and $f \in L^2(0,T;(L^2(\Omega))^d)$, find $\widetilde{u} \in V$ and $\widetilde{p}$ at any time t such that

$$\begin{aligned} \frac{d}{dt} < \widetilde{u}, v > + a(\widetilde{u},v) + b(v,\widetilde{p}) &= < f, v >, \quad for \quad any \quad v \in (H_0^1(\Omega))^d \quad (119) \\ b(\widetilde{u},q) &= 0, \quad for \quad any \quad q \in L_0^2(\Omega) \\ \widetilde{u}(0) &= \phi \end{aligned}$$

We approximate (118) as follows: Find $u_h \in C^1(0,T;S_h)$ and $p_h \in C^0(0,T;Q_h)$ such that

$$\begin{aligned} \frac{d}{dt} < u_h, v_h > + a(u_h,v_h) + b(v_h,p_h) &= < f, v_h > \text{ for all } v_h \in S_h \\ b(u_h,q_h) &= 0 \text{ for all } q_h \in Q_h \\ u_h(0) &= u_h(T) \quad (120) \end{aligned}$$

From the second equality of equation (119), $b(v,q) = 0$ for all $q \in L_0^2(\Omega)$, whenever $v \in V$, so we can estimate the time-periodic velocity without involving the pressure term, as long as we take the test function in V.
Then problem (118) becomes: Find $u \in L^2(0,T;V) \cap L^\infty(0,T;H)$ such that

$$\begin{aligned} \frac{d}{dt} < u, v > + a(u,v) &= < f, v > \quad for \quad any \quad v \in V \quad (121) \\ u(0) &= u(T) \end{aligned}$$

and the initial value problem (119): Given $\phi \in L^2(\Omega)$, find $\widetilde{u} \in V$ at any time t such that

$$\begin{aligned} \frac{d}{dt} < \widetilde{u}, v > + a(\widetilde{u},v) &= < f, v >, \quad for \quad any \quad v \in V \quad (122) \\ \widetilde{u}(0) &= \phi \end{aligned}$$

As in Section 2.2, the solution of (122) can be written as (see [22])

$$\widetilde{u}(t) = E(t,0)\phi + \int_0^t E(t,s)f(s)ds = E(t,0)\phi + g(t) \tag{123}$$

$E(t,\tau)\phi$ is the solution of (122)with $f = 0$ and initial value ϕ given at $t = \tau > 0$. We can prove the following Lemma as in **Lemma 2.2.1**

Lemma 2.3.5. $\| E(t,0) \| \leq c < 1$, *with c independent of h.*

The semi-discrete problem (120) can be treated as for going from problem (118) to problem (121), without involving the pressure term, if we take $v_h \in V_h$. Then problem (120) writes as : Find $u_h \in V_h$ such that

$$\begin{aligned} \frac{d}{dt} < u_h, \psi > + a(u_h, \psi) &= < f, \psi >, \quad for \quad any \quad \psi \in V_h, \quad and \quad t \in (0,T) \\ u_h(0) &= u_h(T) \end{aligned} \tag{124}$$

We associate to (124) the following semi-discrete problem : Given $\phi_h \in V_h$, find $\widetilde{u}_h \in V_h$ such that

$$\begin{aligned} \frac{d}{dt} < \widetilde{u}_h, \psi > + a(\widetilde{u}_h, \psi) &= < f, \psi >, \quad t \in (0,t) \quad and \quad any \quad \psi \in V_h \\ \widetilde{u}_h(0) &= \phi_h \end{aligned} \tag{125}$$

Let $E_h(t,\tau) : V_h \to V_h, \quad t \geq \tau$, be the solution operator of the semi-discrete homogeneous equation with initial value given at $t = \tau$. As in Section 2.2 we have the following result: Let $E_h(t,0)\phi_h$ be the solution at time t of (125) with $f = 0$, then

Lemma 2.3.6.

$$\| E_h(t,0) \| \leq c < 1$$

with c independent of h.

Theorem 2.3.7. *Let u and u_h be solutions of (121) and (124). Then*

$$\| u(t) - u_h(t) \| \leq Ch^{r+1}c(u,p), \ C \ constant$$

for all $t \leq T$.

Proof. Similar to proof of **Theorem 2.2.3**. □

The backward Euler fully discrete scheme writes as: Find $U_n \in V_h$ such that

$$\begin{aligned}(\frac{U_n - U_{n-1}}{k}, \psi) + a(U_n, \psi) &= (f(t_n), \psi), \quad n = 1, 2, ..., N \quad and \quad \psi \in V_h \\ U_0 &= U_N\end{aligned} \tag{126}$$

The fully discrete scheme for the initial value problem is: Given $\phi_h \in V_h$ find $\widetilde{U}_n \in V_h$ such that

$$\begin{aligned}(\frac{\widetilde{U}_n - \widetilde{U}_{n-1}}{k}, \psi) + a(\widetilde{U}_n, \psi) &= (f(t_n), \psi), \quad \psi \in V_h \\ \widetilde{U}_0 &= \phi_h\end{aligned} \tag{127}$$

E_{hk} is the solution operator of the initial value problem with $f = 0$, as defined in Section 2.2.

Lemma 2.3.8.

$$\| E_{hk}(T, 0) \| \leq c < 1, \ \textit{with } c \textit{ independent of } h.$$

Theorem 2.3.9. *Let U_n be solution of (126) and $u(T)$ solution of (121). Then*

$$\| U_N - u(T) \| \leq Ch^{r+1}c(u, p) + Ck \left(\int_0^T \| \frac{\partial^2 u_h}{\partial \tau^2}(\tau) \|^2 \, d\tau \right)^{\frac{1}{2}}$$

Proof. See proof of **Theorem 2.2.5** □

There are two important remarks to be underlined.

Remark1 The existence of the pressure can be proven as in Temam([31]) introducing the following functions $U(t) := \int_0^t u(s)ds$ and $F(t) := \int_0^t f(s)ds$. Integrating (121) over time we see that

$$< u(t) - u_0, v > + \nu((U(t), v)) =< F(t), v >, \quad for \quad any \quad t \in [0, T] \quad and \quad any \quad v \in V \tag{128}$$

or

$$< u(t) - u_0 - \nu \Delta U(t) - F(t), v >= 0 \quad for \quad any \quad t \in [0, T], \quad and \quad any \quad v \in V \tag{129}$$

For each $t \in [0,T]$ there exist some function $P(t) \in L^2(\Omega)$ such that

$$u(t) - u_0 - \nu \Delta U(t) + gradP(t) = F(t) \tag{130}$$

Observing that

$$gradP(t) = F + \nu \Delta U - u + u_0 \tag{131}$$

we conclude that $P \in C(0,T;L^2(\Omega))$ and we can differentiate (130) in the variable t, in the sense of distribution in $\Omega \times (0,T)$. Setting $p = \frac{\partial P}{\partial t}$ we obtain precisely (117). Regarding the periodicity of $p(t)$, this comes from (117) taking in consideration the fact that $u(x,t)$ and $f(x,t)$ are time-periodic.

Remark2 The case of linearized Navier-Stokes equations can be treated in a similar way as the Stokes problem with the extra difficulty which is created by the advective term. Consider the Navier-Stokes equations

$$\begin{aligned} \frac{\partial u}{\partial t} - \nu \Delta u + u \cdot \nabla u + \nabla p &= f \quad in \quad]0,T[\times\Omega && (132)\\ \nabla \cdot u &= 0 \quad in \quad]0,T[\times\Omega && (133)\\ u &= 0 \quad in \quad]0,T[\times\partial\Omega \\ u(x,0) &= u_0 \quad in \quad \Omega \end{aligned}$$

where the vector functions f and u_0 are given, f defined on $[0,T]\times\Omega$, u_0 defined on Ω. The Navier-Stokes equations (132) can be linearized around $\bar{u}$, by taking $u = \bar{u} + \widehat{u}$ with $\bar{u}, \widehat{u} : [0,T] \times \Omega \to \mathbb{R}^d$, e.g to look at the stability of $\bar{u}$. The Navier-Stokes equations becomes

$$\frac{\partial \bar{u}}{\partial t} + \frac{\partial \widehat{u}}{\partial t} + (\bar{u} + \widehat{u}) \cdot \nabla(\bar{u} + \widehat{u}) - \nu \Delta(\bar{u} + \widehat{u}) + \nabla(\bar{p} + \widehat{p}) = \bar{f} + \widehat{f} \tag{134}$$

where $\bar{u}$ satisfies the Navier-Stokes equations

$$\frac{\partial \bar{u}}{\partial t} + \bar{u} \cdot \nabla \bar{u} + \nabla \bar{p} = \bar{f} \tag{135}$$

Then the linearized Navier-Stokes equations writes as

$$\begin{aligned} \frac{\partial \widehat{u}}{\partial t} + \bar{u} \cdot \nabla \widehat{u} + \widehat{u} \cdot \nabla \bar{u} - \nu \Delta \widehat{u} + \nabla \widehat{p} &= \widehat{f} \\ \nabla \cdot \widehat{u} &= 0 && (136) \end{aligned}$$

Assuming the term $\widehat{u} \cdot \nabla \bar{u}$ is small, the linearized Navier-Stokes equations becomes

$$\begin{aligned} \frac{\partial \widehat{u}}{\partial t} + \bar{u} \cdot \nabla \widehat{u} - \nu \widehat{\Delta[6\ tu} + \nabla \widehat{p} &= \widehat{f} \\ \nabla \cdot \widehat{u} &= = 0 \end{aligned} \tag{137}$$

The analysis of the initial value and time-periodic problems for that linearized Navier-Stokes equations, and their discretizations, can be done by combining the techniques for the linear advection-diffusion and the Stokes equations. As a consequence, one notices that the linearized Navier-Stokes equations can only have stable periodic solutions under periodic forcing in the limit $t \to \infty$, and this is true both for the continuous and the discrete problems. If under periodic forcing, the full nonlinear Navier-Stokes equations show a non-periodic solution, this can only be the result of nonlinear effects.

2.4 1-D Advection-diffusion equation

Advection-diffusion equations are an important class of partial differential equations with linear operators that arise in fluid mechanics. Basically they describe physical phenomena involving the transport of physical quantities by moving continua. This section focuses on the numerical results of the 1-D time-periodic advection-diffusion problem. In Section 2.4.1. we study the effect of the coercivity of the associated bilinear form on the existence of a time-periodic solution, using a simple 1-D example. In Section 2.4.2, the numerical experiments intend to explore the relevant parameters that control the convergence to a time-periodic solution. We used a finite element method in space and the backward Euler method in time. The convergence of the solution towards a periodic solutions obtained in our numerical experiments is also confirmed through a spectral analysis of the method.

2.4.1 The necessity of the coercivity of the bilinear form on the existence of a time-periodic solution

As we have proven before in Section 2.2, the coercivity of the bilinear form $a(t;\cdot,\cdot)$ is a sufficient condition to obtain a time-periodic solution of the parabolic PDE involving that bilinear form and a periodic forcing term. As we know, the coercivity is dependent on the diffusion coefficient ν in the advection-diffusion equation. Basically, if $\nu = 0$ the equation is a purely hyperbolic one and the coercivity does not hold.

To study the impact of the coercivity on the existence of a periodic solution, we consider the 1-D advection-diffusion equation

$$\begin{aligned} \frac{\partial u}{\partial t} + c(x,t)\frac{\partial u}{\partial x} - \nu\frac{\partial^2 u}{\partial x^2} &= f, \quad 0 \le x \le 1 \\ u(0,t) &= 0 \\ u(1,t) &= 0 \\ u(x,0) &= 0 \end{aligned} \tag{138}$$

with $c(x,t) = \cos(2\pi t/T)$, $T = 1$ and $f(x,t) = 2.0$ for $x \in (0.4, 0.6)$ and $f(x,t) = 0$ elsewhere, at any time t. In case $\nu = 0$, we have a pure advection equation and the boundary conditions above will be imposed only on the inflow boundary, namely at $x = 0$ when $c(0,t) > 0$ and at $x = 1$ when $c(1,t) < 0$.

The numerical method used here is the explicit upwind finite difference method(which in 1-D case is similar to a Petrov-Galerkin method) with a time step $k = 10^{-3}$, a space step $h = 10^{-2}$ and a number of time steps per period $N = 10^3$. We present two cases:

The case $\nu > 0$

In the situation where $\nu \neq 0$ the solution is time-periodic with period 1. The results at time $t = 20$, 20.25, 20.5, 20.75 and 21 are represented in **Figure 1**. Also, we represent on the same graph the solutions at times 20.0, 25.0 and 30.0. After a transient period of time, the solution stabilizes and it becomes periodic in time. In the calculations, we use $\nu = 0.1$. The larger ν, the quicker the solution becomes periodic. From the theory developed in Section 2.2, it is guaranteed that a periodic solution exists and is asymptotically stable. Hence the numerical solutions behave as predicted by the

theory.

The case $\nu = 0$

In the case where $\nu = 0$ the solution is not time-periodic. The results at time $t = 20$, 21, 22, 23 and 24 are represented in **Figure 2**. Also, it is more evident that the solution tends to increase in time if we look at the graph of the solution at times $t = 20$, 25 and 30, which is an indication of the fact that in the pure advection case we cannot obtain a time-periodic solution. In the next section, a 1-D spectral analysis is used to study the effect of different parameters on the solution.

This example indicates that for some test cases the coercivity is a necessary condition for the existence and stability of a time-periodic solution.

2.4.2 Spectral analysis of a 1-D advection-diffusion equation

The time-periodic problem for the 1-D advection-diffusion equation on the whole real line writes as

$$\begin{aligned} \frac{\partial u}{\partial t} + b\frac{\partial u}{\partial x} &= \nu\frac{\partial^2 u}{\partial x^2} + f \\ u(0) &= u(T) \end{aligned} \tag{139}$$

We do not know the exact value of $u(0)$ so we are going to solve the following initial value problem: Find $\widetilde{u}$ such that

$$\begin{aligned} \frac{\partial \widetilde{u}}{\partial t} + b\frac{\partial \widetilde{u}}{\partial x} &= \nu\frac{\partial^2 \widetilde{u}}{\partial x^2} + f \\ \widetilde{u}(0) &= \widetilde{u}_0 \end{aligned} \tag{140}$$

for a given $\widetilde{u}_0$. Using the theoretical results of Section 2.2 and Section 2.3 we know that the solution of this problem tends to a time-periodic solution because the bilinear form associated to the equation is coercive.

Using the Galerkin FEM in space with $\widetilde{u}(x,t) = \sum_{j=1}^{N} \widetilde{U}_j(t)\Phi_j(x)$, as described in [28, Section 2.3], we approximate (140) on a finite interval $[x_1, ..., x_N]$

$$\begin{aligned} M\frac{d\widetilde{U}}{dt} + Q\widetilde{U} &= \bar{f} \\ \widetilde{U}(0) &= \widetilde{U}^0 \end{aligned} \tag{141}$$

where $\widetilde{U}^0$ is a given initial value and

$$\frac{1}{6}\frac{d\widetilde{U}_{j-1}}{dt}+\frac{2}{3}\frac{d\widetilde{U}_j}{dt}+\frac{1}{6}\frac{d\widetilde{U}_{j+1}}{dt}+(-\frac{b}{2h}-\frac{\nu}{h^2})\widetilde{U}_{j-1}+\frac{2\nu}{h^2}\widetilde{U}_j+(\frac{b}{2h}-\frac{\nu}{h^2})\widetilde{U}_{j+1}=f_N$$

with $1<j<N$. Splitting $\widetilde{U}=U+\bar{U}$ where U is the solution of a time-periodic semi-discrete problem approximating the solution of (139), it results that the transient part $\bar{U}$ solves the following system

$$\begin{aligned} M\frac{d\bar{U}}{dt}+Q\bar{U} &= 0 \\ \bar{U}(0) &= \widetilde{U}^0-U(0) \end{aligned} \tag{142}$$

The transient part $\bar{U}$ generally tends to zero in an infinite time. The question which arises is how fast is the transient going to zero, and which combination of the physical and numerical parameters controls the speed of convergence.

To fully discretize the system we use the backward Euler method and (142) becomes

$$\begin{aligned} (M+kQ)\bar{U}^{n+1}&=M\bar{U}^n \\ \bar{U}^0 &\text{ given.} \end{aligned} \tag{143}$$

The spectral analysis of this system is done using a method similar to the one presented in [34, Chapter 2]: For solutions of the form $\bar{u}(jh,t^n)=\bar{U}^n e^{ijh\xi}$ we have the following recurrence relation $\bar{U}^{n+1}e^{ijh\xi}=g(\xi h)\bar{U}^n e^{ijh\xi}$ where $-\frac{\pi}{h}<\xi<\frac{\pi}{h}$. Substituting this into (143) we have

$$\begin{aligned} g(\xi h)[(\frac{1}{6} &- k(\frac{b}{2h}+\frac{\nu}{h^2}))e^{i(j-1)h\xi}+(\frac{2}{3}+k\frac{2\nu}{h^2})e^{ijh\xi}+(\frac{1}{6}+k(\frac{b}{2h}-\frac{\nu}{h^2}))e^{i(j+1)h\xi}]= \\ &= \frac{1}{6}e^{i(j-1)h\xi}+\frac{2}{3}e^{ijh\xi}+\frac{1}{6}e^{i(j+1)h\xi} \end{aligned}$$

The amplification factor $g(\xi h)$ can be written as

$$g(\xi h)=\frac{\frac{1}{6}\cos(\xi h)+\frac{1}{3}}{(\frac{1}{6}-\frac{\lambda}{Pe_h})\cos(\xi h)+i\frac{\lambda}{2}\sin(\xi h)+\frac{1}{3}+\frac{\lambda}{Pe_h}}$$

where $Pe_h=\frac{bh}{\nu}$ and $\lambda=\frac{kb}{h}$ are the numerical Pechlet and Courant-Friedrich-Levy (CFL) number, respectively.

If we consider N the number of time steps within one period, then the evolution of each wave mode from period to period is given by the N^{th} power of the amplification factor $g(\xi h)$, and we have:

Theorem 2.4.1. *$|g(\xi h)|^N < 1$, for any $0 < Pe_h < \infty$.*

Proof. We can write $|g(\xi h)|$ as

$$\begin{aligned} |g(\xi h)| &= \left| \frac{\frac{1}{6}\cos(\xi h) + \frac{1}{3}}{\sqrt{[(\frac{1}{6} - \frac{\lambda}{Pe_h})\cos(\xi h) + \frac{\lambda}{Pe_h} + \frac{1}{3}]^2 + \frac{\lambda^2}{4}\sin^2(\xi h)}} \right| \\ &= \left| \frac{\frac{1}{6}\cos(\xi h) + \frac{1}{3}}{\sqrt{[(\frac{1}{6}\cos(\xi h) + \frac{1}{3}) + \frac{\lambda}{Pe_h}(1 - \cos(\xi h))]^2 + \frac{\lambda^2}{4}\sin^2(\xi h)}} \right| \end{aligned}$$

But $1 - \cos(\xi h) \geq 0$ and $\frac{\lambda^2}{4}\sin^2(\xi h) \geq 0$ so we can bound $|g(\xi h)|$ by

$$|g(\xi h)| < 1$$

assuming $\lambda \neq 0$. We obtain that $|g(\xi h)|^N < 1$. □

This result proves that the transient part converges to zero in an infinite numbers of periods, so we obtain a time periodic solution when the number of time steps $n \to \infty$. This is in complete agreement with the general theorem of Section 2.2 saying that any linear parabolic PDE, or its discrete version, subject to a periodic forcing admits a stable periodic solution attracting all solutions of the initial value problem. In case both $\lambda/Pe_h \to 0$ and $\lambda \to 0$, then $|g(\xi h)|^N \to 1$, so we should not obtain a time-periodic solution when $n \to \infty$. This will happen if the time step $k \to 0$, i.e. the number N of time steps per period goes to infinity, while h, b and ν, hence Pe_h, are kept constant. This result will be confirmed later in this section by numerical experiments.

If we apply the spectral decomposition $\bar{u}(x,t) = \bar{U}(t)e^{i\xi x}$ to the non-discretized transient problem, we can compare the evolution of the exact solution with the evolution of the solution for the fully-discrete system (143). To do this we need first to evaluate $\bar{u}(x,t)$ knowing that it satisfies the following equation:

$$\begin{aligned} \frac{\partial \bar{u}}{\partial t} + b\frac{\partial \bar{u}}{\partial x} &= \nu \frac{\partial^2 \bar{u}}{\partial x^2}, \\ \bar{u}(x,0) &= \bar{u}_0 \end{aligned} \tag{144}$$

Assuming the exact solution takes the form $\bar{u}(x,t) = \bar{U}(t)e^{i\xi x}$

$$\frac{d\bar{U}}{dt} + bi\xi\bar{U} = -\nu\xi^2\bar{U} \tag{145}$$

Solving (145) with the initial value $\bar{U}(0) = \bar{U}_0$, we get

$$|\bar{U}(T)| = |\bar{U}_0|e^{-\nu\xi^2 T} \tag{146}$$

After one period $T = N\,k$ and the solution can be written in the form

$$|\bar{U}(T)| = |\bar{U}_0|(e^{-\frac{\nu k}{h^2}(\xi h)^2})^N \tag{147}$$

or

$$|\bar{U}(T) = |\bar{U}_0|e^{-\frac{\lambda N}{Pe_h}(\xi h)^2} \tag{148}$$

From (148) it is obvious that the exact solution of the transient problem for each wave mode converges to zero with the increasing number of periods since initial time, as long as $\lambda N/Pe_h(\xi h)^2 > 0$. On the other hand if $\lambda N/Pe_h = 0$, the solution $|\bar{U}(T)| = |\bar{U}_0|$ and the transient solution no longer converges to a periodic solution. This happens when $\nu = 0$. Moreover, when k approaches 0 and Pe_h is kept constant, the damping factor $e^{-\frac{\lambda N}{Pe_h}(\xi h)^2}$ of the exact solution from period to period remains constant, as opposed to the amplification factor $|g(\xi h)|^N$ of the fully discrete solution going to 1 under similar conditions.

Numerical experiments

We investigate the consequences of the spectral analysis done in the previous section by solving numerically a simple 1-D advection-diffusion equation with a time-periodic forcing term. For our numerical experiment we consider $f = \sin(2\pi t/T)$ on $[0,1]$ and $u(0) = u(1) = 0$.

The strategy used to compute a periodic solution is the following:

- Start with an initial condition $U_j^0 = u_0(x_j)$, $x_j = jh \in [0,1]$, where $u_0(x) = 1-x$;
- Iterate in time by computing U^{n+1} from U^n, using N time steps $k = T/N$ per period, up to the point where the following stopping criteria on succesive iterations of the Poincaré map is met:

$$\| U^{(i+1)N} - U^{iN} \| \leq 10^{-8}. \tag{149}$$

where i is the number of periods computed since initial time.

We will compare the predictions of the spectral analysis and 1-D simulations with published numerical results obtained by M.Rosenfeld in [25]. The focus of that paper is on incompressible viscous flows in two-dimensional constricted channels with time-periodic inflow. The experiments show that the results depend on the Reynolds number ($Re = \frac{U_m d}{\nu}$) and the Strouhal number ($Str = \frac{d}{TU_m}$) where d is the width of the channel and U_m the mean velocity. The Navier-Stokes equations and the advection-diffusion equations belong to the same class of problems, with the extra-difficulty given by the non-linear term in the Navier-Stokes equations, hence the interest in comparing our conlusions with Rosenfeld's results. The data considered are

- $d = 1$, $h = 4.79 \times 10^{-2}$
- $Re = 360$, $U_m = 1.39$
- $k = T/200$ and $N = 200$

The number of periods needed to reach a periodic solution for Navier-Stokes equations for $Str = 0.386$, 0.011 and 11.787, are compared with the number of periods obtained for our 1-D advection-diffusion problem as we can see in **Table 1** and **Table 2**. When $Pe_h = 17.244$ and λ is small, e.g. $\lambda = 6.26 \cdot 10^{-3}$, the number of periods necessary to reach a time-periodic solution is large of order $O(10^2)$. When $\lambda = 6.784$, the time-periodic solution is obtained in two or three periods. If we increase $Pe_h = 1000$, we see that the number of periods is very large $O(10^3)$ when $\lambda = 6.26 \cdot 10^{-3}$. If $\lambda = 6.784$ the result is not affected by the increase of Pe_h, i.e. the time-periodic solution is obtained in two or three periods. It is surprising to see how well simple 1-D linear simulations predict the trends for the transients in 2-D nonlinear incompressible flow simulations. That 1-D analysis gives at least a lower bound on the number of periods needed to approach a periodic solution of the Navier-Stokes equations with a given accuracy, and will be used to analyze our flow simulations in Chapter 4.

In **Figure 3** the amplification factor $|g(\xi h)|^N$ is ploted keeping Pe_h at two constant values 17.244 and 1000, and taking for λ the values given in the table. We also plot the amplification factor corresponding to the exact solution of the problem (144) using

Table 1: Number of periods necessary to obtain a periodic solution if $Pe_h = 17.244$

Pe_h	λ	Str	T	2-D flows	1-D adv diff
17.244	0.208	0.387	2	20	5
17.244	6.784	0.011	65	3	2
17.244	6.26×10^{-3}	11.787	0.06	400	156

Table 2: Number of periods necessary to obtain a periodic solution if $Pe_h = 1000$

Pe_h	λ	Str	T	1-D adv diff
1000	0.208	0.387	2	12
1000	6.784	0.011	65	2
1000	6.26×10^{-3}	11.787	0.06	3327

the expression in (148) when $\lambda = 0.208$. As we can see, in the case of a small λ which also is associated to the small period $T = 0.06$, the amplification factor after one period does not drop sharply to zero. In fact it has values close to 1 for $Pe_h = 1000$. That means the transient part tends to zero very slowly so we need a large number of periods to obtain a time-periodic solution. On the contrary, when λ becomes larger and larger, the amplification factor is very close to zero for most ξh except near the origin, implying that a time-periodic solution is obtained in a relatively small number of periods. The graphs of the amplification factors are in complete agreement with the numerical simulations presented in the **Table 1** and **Table 2**: Larger Pe_h for a fixed λ, or smaller λ for a fixed Pe_h, both imply less damping from period to period, hence more periods are needed to converge to a periodic state. Moreover, the prediction of the transient by the numerical scheme can be quite wrong for some wave modes, if we compare the blue (numerical) with the black (exact) curves on each graph.

Spectral analysis on a bounded domain The 1-D spectral analysis has been done for an unbounded domain, i.e. $\mathbb{R}$, so we have to study the impact of restricting the

problem to an interval $[0, L]$. We consider the problem

$$\begin{aligned} \frac{\partial \bar{u}}{\partial t} + b\frac{\partial \bar{u}}{\partial x} - \nu\frac{\partial^2 \bar{u}}{\partial x^2} &= 0, \quad 0 < x < L \\ \bar{u}(0,t) = \bar{u}(L,t) &= 0 \\ \bar{u}(x,0) &= \bar{u}_0(x), \quad 0 < x < L \end{aligned} \tag{150}$$

The eigenvalues and eigenfunctions of the advection-diffusion operator with Dirichlet boundary conditions can be calculated, at least in the continuous case. Assuming $\bar{u}(x,t) = e^{-\delta_n t}u_n(x)$, this gives

$$-\delta_n u_n(x) + b\frac{\partial u_n(x)}{\partial x} - \nu\frac{\partial^2 u_n(x)}{\partial x^2} = 0 \tag{151}$$

This is a linear second order differential equation with constant coefficients with the associated characteristic equation

$$-\nu\gamma^2 + b\gamma - \delta_n = 0.$$

The solutions of this equation are

$$\gamma = \frac{b \pm \sqrt{b^2 - 4\nu\delta_n}}{2\nu}$$

Assuming that the γ's are complex, we can generate the solution $u_n(x) = e^{-\frac{bx}{2\nu}}\sin(\frac{\sqrt{b^2-4\nu\delta_n}x}{2\nu})$ that satisfies the boundary conditions $\bar{u}_n(0) = \bar{u}_n(L) = 0$. We obtain that

$$\sqrt{\frac{b^2 - 4\nu\delta_n}{4\nu^2}} = \frac{in\pi}{L} \tag{152}$$

which is an equation in the unknown δ_n. Solving this equation gives us

$$\delta_n(\nu) = \frac{b^2}{4\nu} + \frac{\nu n^2\pi^2}{L^2} \tag{153}$$

The solution $\bar{u}_n(x,t) = e^{-\delta_n t}u_n(x)$ of the problem (150) could be seen as the transient response of an advection-diffusion equation on $[0, L]$ with homogeneous Dirichlet boundary conditions, periodic volumic forcing and an initial solution $\widetilde{u}(0) = u(0) + u_n$. Here we use the decomposition of $\widetilde{u}$ into the periodic and transient responses presented in Section 2.4.2. Clearly, the transient response $\bar{u}_n$ decays exponentially in time to 0

over all $[0, L]$, with a rate controlled by δ_n.

From Equation (153), one can see that for a fixed diffusion coefficient ν, the eigenvalue $\delta_n(\nu)$ increases with the wave number n and the advection velocity b, but decreases with the domain length L. This is confirmed by the the graph presented on **Figure 4**, where the parameters $b = 1$, $L = 1$, $n = 1$ set the base case to which all the other cases are compared. The consequence is that the transient mode $\bar{u}_n$ will be damped more slowly on larger domains, but a higher advective velocity b easily compensates for that loss of damping. Also, highly oscillating modes are damped more rapidly in time, leaving in the transient solution for large time t only the first modes with small $\delta_n(\nu)$.

From **Figure 4**, one can see that as a function of ν, $\delta_n(\nu)$ monotonically decreases for small ν to reach a minimum, then to increases monotonically for large values of ν. These two situations correspond to an advection dominant equation and to a diffusion dominant equation, respectively. If ν is small, $\delta_n(\nu)$ is large because of the term $b^2/4\nu$: Transient waves are rapidly advected and washed out out the domain. If ν is large, $\delta_n(\nu)$ is large because of the term $\nu n^2\pi^2/L^2$: Transient waves are rapidly damped by diffusion very much like for the heat equation.

Chapter 3

Time-periodic solutions of the Navier-Stokes equations

The existence of time-periodic solutions of PDEs has been studied before. In his book [17], J.L.Lions proved the existence of a time-periodic solution for the Navier-Stokes equations subject to a periodic volumic force field.
In some industrial applications, the periodicity is enforced by a moving boundary rather than an external volumic force applied to the fluid. It seems natural to consider a periodic moving boundary when we think about lid-diven cavities. For example in biofluid applications, the flow in a portion of an artery is driven by the inflow boundary conditions. Therefore, the existence of a time-periodic solution for the Navier-Stokes equations subject to periodic boundary conditions will be investigated in this chapter.

3.1 Navier-Stokes equations with non-homogeneous Dirichlet boundary conditions

The main purpose of this section is to present the proof of the existence of solutions for problems with non-homogeneous boundary conditions. As we shall see the proof is long and requires some additional results, but it will give us a better idea of the

steps which have to be followed in the time-periodic case. The non-homogeneous case needs an extra treatment, i.e. to transform the problem into one with homogeneous boundary conditions by extending the function on the boundary into one on the whole domain, under some regularity conditions. To our knowledge there is one reference of such a proof,R. Temam [31], but he treats only the stationary problem. The following intends to be a demonstration of the solution's existence for a time-dependent problem with non-homogeneous Dirichlet boundary conditions.
Basically, the problem considered is: Let Ω be an open, bounded Lipschtiz set in $\mathbb{R}^d$. We denote by $Q :=]0,T[\times\Omega, T > 0$. The Navier-Stokes problem is defined by:
Find a vector function

$$u = \{u_1, u_2, ..., u_d\} : [0,T] \times \Omega \to \mathbb{R}^d$$

and a scalar function

$$p : [0,T] \times \Omega \to \mathbb{R},$$

respectively the velocity of the fluid and its pressure, such that

$$\begin{aligned} \frac{du}{dt} - \nu\Delta u + u \cdot \nabla u + \nabla p &= f \quad in \quad Q \\ \nabla \cdot u &= 0 \quad in \quad Q \\ u &= \phi \quad in \quad]0,T[\times\partial\Omega \\ u(x,0) &= u_0 \quad in \quad \Omega(\text{ i.e. } u_i(x,0) = u_{0i}(x),\ x \in \Omega) \end{aligned} \tag{154}$$

where the vector functions f, ϕ and u_0 are given, f defined on $]0,T[\times\Omega$, u_0 defined on Ω, ϕ defined on $]0,T[\times\partial\Omega$ and ν is a constant. We suppose that f is given in $L^2(0,T;(H^{-1}(\Omega))^d)$ and that ϕ is the restriction of a function ψ defined on Ω such that

$$\begin{aligned} \psi &\in L^2(0,T;(H^2(\Omega))^d) \\ \nabla \cdot \psi(t) &= 0 \\ \psi(t) &= \phi \quad on \quad \partial\Omega \end{aligned} \tag{155}$$

at any time t.
Then we look for a solution $\widehat{u} = u - \psi$ of a homogeneous problem. From (154) we

obtain

$$\begin{aligned} \frac{d\widehat{u}}{dt} - \nu\Delta\widehat{u} + \widehat{u}\cdot\nabla\widehat{u} + \widehat{u}\cdot\nabla\psi + \psi\cdot\nabla\widehat{u} + \nabla p &= \widehat{f} \quad in \quad Q \\ \nabla\cdot\widehat{u} &= 0 \quad in \quad Q \\ \widehat{u} &= 0 \quad in \quad]0,T[\times Q \end{aligned} \tag{156}$$

where $\widehat{f} = f + \nu\Delta\psi - \psi\cdot\nabla\psi - \frac{\partial\psi}{\partial t}$.
We introduce the following spaces

$$\mathscr{V} := \quad \{u \in \mathscr{D}^d(\Omega), \quad \nabla\cdot u = 0\} \tag{157}$$

$$V := the \quad closure \quad of \quad \mathscr{V} \quad in \quad (H_0^1(\Omega))^d \tag{158}$$

$$H := the \quad closure \quad of \quad \mathscr{V} \quad in \quad (L^2(\Omega))^d \tag{159}$$

with the same properties as in Section 2.3.2.
We define the following bilinear form
$a \in (V \times V; \mathbb{R})$

$$a(u,v) := \nu((u,v)) \tag{160}$$

and the following trilinear form

$$b(w,u,v) := \int_\Omega (w\cdot\nabla u)\cdot v dx = \sum_{i,j=1}^{n} \int_\Omega w_j (D_j u_i) v_i dx$$

In the weak sense, equations (156) can be written as: Find $\widehat{u} \in L^2(0,T;V) \cap L^\infty(0,T;H)$ such that

$$\begin{aligned} \frac{d}{dt} < \widehat{u}, v > + \nu((\widehat{u},v)) + b(\widehat{u},\widehat{u},v) + b(\widehat{u},\psi,v) + b(\psi,\widehat{u},v) &= < \widehat{f}, v > \\ \widehat{u}(0) &= \widehat{u}_0 \end{aligned} \tag{161}$$

for all $v \in L^2(0,T;V) \cap (L^d(\Omega))^d$, with $\widehat{f} \in L^2(0,T;V')$ (see [31]).
We state the following Lemmas which we are going to use in the proof of our theorem.

Lemma 3.1.1. *For $u \in V$, $v \in (H_0{}^1(\Omega))^d \cap (L^d(\Omega))^d$ we have that*

$$b(u,v,v) = 0 \tag{162}$$

Proof. For all u and $v \in V$ we know that

$$\int_\Omega u_i D_i v_j v_j = \int_\Omega u_i D_i \frac{(v_j)^2}{2} dx = -\frac{1}{2} \int_\Omega D_i u_i (v_j)^2 dx$$

Summing over all i and j we obtain

$$b(u, v, v) = -\frac{1}{2} \sum_{j=1}^{n} \int_\Omega \nabla \cdot u (v_j)^2 dx = 0$$

□

Lemma 3.1.2. *Consider the mapping $t \to B(w(t), u(t))$ defined a.e. on $[0, T]$ by*

$$\begin{aligned} B(w(t), u(t)) &\in [(H^1(\Omega))^d]' \\ < B(w(t), u(t)), v > &= b(w(t), u(t), v), \quad for \quad any \quad v \in H_0^1(\Omega) \end{aligned}$$

If $u, w \in L^2(0, T; (H^1(\Omega))^d) \cap L^\infty(0, T; H)$ then

$$\begin{aligned} B(w, u) &\in L^2(0, T; [(H^1(\Omega))^d]'), \text{ if } d = 2 \\ B(w, u) &\in L^{\frac{4}{3}}(0, T; [(H^1(\Omega))^d])', \quad if \quad d = 3 \end{aligned} \tag{163}$$

Proof. For a proof see [12, pages 157–158], the results follow the same way. □

Lemma 3.1.3. *The trilinear form $b(\cdot, \cdot, \cdot)$ is well defined and continuous on $(H^1(\Omega))^d \times (H^1(\Omega))^d \times (H^1(\Omega))^d \cap (L^d(\Omega))^d)$ at any time t.*

Proof. If $u \in (H^1(\Omega))^d$ we have that $u_i \in H^1(\Omega)$ so by the Sobolev's Theorem, $u_i \in L^q(\Omega)$, $\frac{1}{q} = \frac{1}{2} - \frac{1}{d}$ and we observe that

$$|\int_\Omega u_j (D_j v_i) w_i dx| \leq \| u_j \|_{L^q(\Omega)} \| D_j v_i \|_{L^2(\Omega)} \| w_i \|_{L^d(\Omega)}$$

which implies that $b(\cdot, \cdot, \cdot)$ is continuous. □

Lemma 3.1.4. *Let $u \in L^2(0, T; (H^1(\Omega))^d) \cap L^\infty(0, T; H))$, then u satisfies*

$$u \in L^4(0, T; (L^p(\Omega))^d), \quad \frac{1}{p} = \frac{1}{2} - \frac{1}{2d} \tag{164}$$

Proof. If $u = \{u_i\}$ we have that

$$u_i \in L^2(0,T;H^1(\Omega)) \cap L^\infty(0,T;L^2(\Omega)) \tag{165}$$

Two cases can be distinguished

1. $d = 2$ From Interpolation inequalities [17, page 71] and (165) we have that

$$\| u_i(t) \|_{L^4(\Omega)} \leq C(\Omega) \| u_i(t) \|^{\frac{1}{2}}_{H^1(\Omega)} \| u_i(t) \|^{\frac{1}{2}}_{L^2(\Omega)} \leq c \| u_i(t) \|^{\frac{1}{2}}_{H^1(\Omega)}$$

   From here we obtain that $u_i \in L^4(0,T;L^4(\Omega))$ and using (165) we obtain (164) with $p = 4$.

2. $d \geq 3$ Using the Sobolev's Theorem with $(H^1(\Omega) \hookrightarrow L^q(\Omega))$ and (165) implies that

$$u_i \in L^2(0,T;L^q(\Omega)) \cap L^\infty(0,T;L^2(\Omega))$$

   with $\frac{1}{q} = \frac{1}{2} - \frac{1}{d}$. Using Hölder inequality and (165)

$$\| u_i(t) \|_{L^p(\Omega)} \leq \| u_i(t) \|^{\frac{1}{2}}_{L^q(\Omega)} \| u_i(t) \|^{\frac{1}{2}}_{L^2(\Omega)} \leq c \| u_i(t) \|^{\frac{1}{2}}_{L^q(\Omega)}$$

   which gives $u_i \in L^4(0,T;L^p(\Omega))$ and this implies (164).

□

Lemma 3.1.5. *For all $\gamma > 0$, there exists some $\psi = \psi(\gamma)$ satisfying (155) and*

$$|b(v(t),\psi,v(t))| \leq \gamma \| v(t) \|^2_1 \tag{166}$$

at any time t.

Remark The existence of ψ which satisfies (155) was proven in [31, page 173].

Theorem 3.1.6. *If we chose any vector ψ with properties (155) and (166), there exists at least one u such that (154) hold.*

Proof. Setting $\widehat{u} = u - \psi$, the problem (154) writes as (156), which is equivalent to the variational problem (161).

The proof requires three main steps:

1) Estimation a priori I

We consider a basis $\{\widehat{w}_m\}_{m\geq 1}$ of V and we denote by $V_m := span\{\widehat{w}_1, ..., \widehat{w}_m\}$.

Remark The spectral problem $((\widehat{w}, v)) = \lambda(\widehat{w}, v), \quad v \in V$ admits a sequence of non zero solutions $\widehat{w}_j \in V$ corresponding to a sequence of eigenvalues λ_j that satisfies $((\widehat{w}_j, v)) = \lambda_j(\widehat{w}_j, v), \lambda_j > 0$, see [17, page 74]. The spectral basis members $\widehat{w}_i$ are orthogonal for both the L^2 and H^1 dot product.

We can replace the problem (156) by the following problem in $V_m \times [0, T]$: Find $\widehat{u}_m(t)$ of the form $\widehat{u}_m(t) = \sum_{j=1}^m g_{jm}(t)\widehat{w}_j$ satisfying the initial value problem for a system of first oder ODE.

$$\begin{aligned} \frac{d}{dt} < \widehat{u}_m(t), \widehat{w}_i > + a(\widehat{u}_m, \widehat{w}_i) + b(\widehat{u}_m, \widehat{u}_m, \widehat{w}_i) + b(\widehat{u}_m, \psi, \widehat{w}_i) + b(\psi, \widehat{u}_m, \widehat{w}_i) &= < \widehat{f}, \widehat{w}_i > \\ \widehat{u}_m(0) &= \widehat{u}_{0m} \quad (167) \end{aligned}$$

for $1 \leq i \leq m$.($\widehat{u}_{0m}$ can be the projection of $\widehat{u}_0$ on V_m for the norm of H)

But $\widehat{u}_m = \sum_{j=1}^m g_{jm}(t)\widehat{w}_j$ so (167) becomes

$$\begin{aligned} \sum_{j=1}^m < \widehat{w}_j, \widehat{w}_i > \frac{d}{dt} g_{jm}(t) &+ \sum_{j=1}^m a(\widehat{w}_j, \widehat{w}_i) g_{jm}(t) + \\ + \sum_{j=1}^m \sum_{k=1}^m b(\widehat{w_j}, \widehat{w}_k, \widehat{w}_i) g_{jm}(t) g_{km}(t) &+ \sum_{j=1}^m b(\widehat{w}_j, \psi, \widehat{w}_i) g_{jm}(t) + \\ + \sum_{j=1}^m b(\psi, \widehat{w}_j, \widehat{w}_i) g_{jm}(t) &= < \widehat{f}(t), \widehat{w}_i > \quad (168) \end{aligned}$$

for $1 \leq i \leq m$, with the starting value $g_{jm}(0) = g_{jm}^0$, where $g_{jm}(0) = g_{jm}^0$ are the coefficients of $\widehat{u}_{0m}$ in the basis $\widehat{w}_1, \ldots, \widehat{w}_n$.

The $m \times m$ matrix $[< \widehat{w}_j, \widehat{w}_i >]$ for $1 \leq i, j \leq m$ is nonsingular since $\widehat{w}_1, ..., \widehat{w}_m$ are linearly independent.

According to Caratheodory's theorem (see [7]), this system of ODEs has a local solution $\widehat{u}_m(t)$ on a maximal time interval $[0, t_m[$ for some $t_m \leq T$. If $t_m < T$ then necessarily $lim_{t \to t_m^-} \parallel \widehat{u}_m(t) \parallel = \infty$. Therefore, if we show that $\parallel \widehat{u}_m(t) \parallel$ is bounded

independently of m and t, then this will prove that $t_m = T$ for any m and that $\widehat{u}_m(t)$ is in fact a global solution of the initial value problem over the interval $[0, T]$.
For this, let $t \in [0, t_m[$, multiply (167) by $g_{im}(t)$ and sum over 1 to m. In view of $b(u, v, v) = 0$ we get

$$< \frac{d\widehat{u}_m}{dt}, \widehat{u}_m > + \nu \parallel \widehat{u}_m \parallel_1^2 + b(\widehat{u}_m, \psi, \widehat{u}_m) = < \widehat{f}, \widehat{u}_m > \tag{169}$$

Let us integrate both sides of this equation on $[0, t]$ and apply Green's formula ([9])

$$\begin{aligned} \frac{1}{2} \parallel \widehat{u}_m(t) \parallel^2 - \frac{1}{2} \parallel \widehat{u}_m(0) \parallel^2 \quad &+ \quad \nu \int_0^t \parallel \widehat{u}_m(s) \parallel_1^2 ds + \\ + \int_0^t b(\widehat{u}_m(s), \psi(s), \widehat{u}_m(s)) ds \quad &= \quad \int_0^t < \widehat{f}(s), \widehat{u}_m(s) > ds \end{aligned} \tag{170}$$

or

$$\begin{aligned} \parallel \widehat{u}_m(t) \parallel^2 \quad &+ \quad 2\nu \int_0^t \parallel \widehat{u}_m(s) \parallel_1^2 ds = \parallel \widehat{u}_m(0) \parallel^2 - 2 \int_0^t b(\widehat{u}_m(s), \psi, \widehat{u}_m(s)) ds \\ &+ \quad 2 \int_0^t < \widehat{f}(s), \widehat{u}_m(s) > ds \end{aligned} \tag{171}$$

Due to the assumption made on ψ (155), taking $\gamma = \frac{\nu}{4}$ we have that

$$|b(v, \psi, v)| \leq \frac{\nu}{4} \parallel v \parallel_1^2$$

Which proves that

$$\begin{aligned} \int_0^t (-b(\widehat{u}_m, \psi, \widehat{u}_m) + < \widehat{f}, \widehat{u}_m >) dt \quad &\leq \quad \int_0^t (\frac{\nu}{4} \parallel \widehat{u}_m \parallel_1^2 + \parallel \widehat{f} \parallel_{V'} \parallel \widehat{u}_m \parallel_1) dt \\ &\leq \quad \int_0^t (\frac{\nu}{4} \parallel \widehat{u}_m \parallel_1^2 + \frac{\nu}{4} \parallel \widehat{u}_m \parallel_1^2 + C \parallel \widehat{f} \parallel_{V'}^2) dt \end{aligned}$$

Then (171) becomes

$$\parallel \widehat{u}_m(t) \parallel^2 + \nu \int_0^t \parallel \widehat{u}_m(s) \parallel_1^2 ds \leq \parallel \widehat{u}_m(0) \parallel^2 + C \int_0^t \parallel \widehat{f}(s) \parallel_{V'}^2 ds$$

because $\parallel \cdot \parallel \leq \parallel \cdot \parallel_1$.
Therefore we can conclude that $\widehat{u}_m(t)$ can be bounded in $L^2(0, T; V) \cap L^\infty(0, T; H)$ with a bound independent from t and this proves that $t_m = T$, so $u_m(t)$ is a global

solution of (167) on $[0,T]$.

2) Estimation a priori II

We are going to demonstrate that $\frac{d}{dt}\widehat{u}_m$ is bounded in $L^2(0,T;V')$. Let us define the projection operator $\Pi_m : V' \to V_m \subset V$ as in [17, page 75]

$$\Pi_m h := \sum_{i=1}^{m} < h, \widehat{w}_i > \widehat{w}_i \tag{172}$$

As mentioned in the **Remark** made at the beginning of the proof, the eigenfunctions $\widehat{w}_i$ are in V. From the identification of the duality product $< \cdot, \cdot >$ with the dot product over H (because $V \hookrightarrow H = H' \hookrightarrow V'$), Π_m is nothing but the H-projection operator on the subspace V_m whenever the function h in taken in H, hence $\| \Pi_m \|_{\mathscr{L}(H,H)} \leq 1$. This can be proven in the following way

$$\| \Pi_m u \|_V^2 = \sum_{i,j=1}^{m} < u, \widehat{w}_i >< u, \widehat{w}_j > (\widehat{w}_i, \widehat{w}_j)_V = \sum_{i=1}^{m} (u, \widehat{w}_i)_H^2 \lambda_i$$

The last equality comes from the fact that $\widehat{w}_i$ and $\widehat{w}_j$ are the spectral basis member defined in the begining of our proof. From the spectral theorem we obtain

$$\sum_{i=1}^{m} (u, w_i)_H^2 \lambda_i = \| \nabla u \|_H^2$$

This can be bounded as follows

$$\| \nabla u \|_H^2 \leq \| u \|_V^2$$

Because $\Pi_m = \Pi_m^T : V' \to V'$ we obtain $\| \Pi_m \|_{\mathscr{L}(V',V')} = \| \Pi_m \|_{\mathscr{L}(V,V)}$.
By transposition and the fact that Π_m is self-adjoint, we obtain $\| \Pi_m \|_{\mathscr{L}(V',V')} \leq 1$.
Remark The fact that Π_m is self-adjoint can be proved easily as follows: For any u,

$v \in V'$

$$\begin{aligned} < \Pi_m u, v >_{V \times V'} &= < \sum_{i=1}^{m} < u, \widehat{w}_i > \widehat{w}_i, v >_{V \times V'} \\ &= \sum_{i=1}^{m} < u, \widehat{w}_i >< v, \widehat{w}_i > \\ &= < u, \sum_{i=1}^{m} < v, \widehat{w}_i > \widehat{w}_i >_{V' \times V} \\ &= < u, \Pi_m v >_{V' \times V}, \end{aligned}$$

thus $\Pi_m = \Pi_m^*$.

We define the operator A as follows

$$a(u, v) =< Au, v >, \quad A \in \mathscr{L}(V, V'). \tag{173}$$

Using the operators A, B and Π_m defined so far, the variational form (161) reformulates as an equation over V'

$$\frac{d}{dt}\widehat{u}_m = -\Pi_m(B(\widehat{u}_m, \widehat{u}_m)) - \Pi_m(B(\widehat{u}_m, \psi)) - \Pi_m(B(\psi, \widehat{u}_m)) - \nu \Pi_m A \widehat{u}_m + \Pi_m \widehat{f} \tag{174}$$

From **Lemma 3.1.2**, that equation makes sense in V' as

$$B(\widehat{u}_m, \widehat{u}_m), B(\widehat{u}_m, \psi), B(\psi, \widehat{u}_m) \in [(H^1(\Omega))^d]' \hookrightarrow V'.$$

Also $A\widehat{u}_m \in L^2(0, T; V')$.

From the fact that $\| \Pi_m \|_{\mathscr{L}(V', V')} \leq 1$ and the boundedness of $\widehat{u}_m$ in the space $L^2(0, T; V) \cap L^\infty(0, T; H)$, the equation (174) implies that $\frac{d}{dt}\widehat{u}_m$ is bounded in $L^2(0, T; V')$.

3) Convergence to the limit

The following inclusions hold

$$V \hookrightarrow H \hookrightarrow V'$$

and $V \hookrightarrow H$ is compact as in [17, page 76].

Using the weak- and weak* compactness of bounded sets in Sobolev spaces as well as a compactness theorem (see [17, page 58]), we can extract a subsequence $\widehat{u}_\mu$ of $\widehat{u}_m$ such that

(i) weak $lim_{\mu \to \infty} \widehat{u}_\mu = \widehat{u}$ in $L^2(0, T; V)$

(ii) weak* $lim_{\mu\to\infty}\widehat{u}_\mu = \widehat{u}$ in $L^\infty(0,T;H)$
(iii) a.e. and strong $lim_{\mu\to\infty}\widehat{u}_\mu = \widehat{u}$ in $L^2(0,T;H)$
(iv) weak $lim_{\mu\to\infty}\frac{d}{dt}\widehat{u}_\mu = \frac{d}{dt}\widehat{u}$ in $L^2(0,T;V')$
Item (i) and (ii) imply that $\widehat{u}_\mu(0) \to \widehat{u}(0)$ weak in V'.
From (164) we have the following limit

$$\text{weak } \widehat{u}_{\mu i}\widehat{u}_{\mu j} \to \xi_{ij} \text{ in } L^2(0,T;L^{\frac{p}{2}}(\Omega)) \text{ with } \frac{1}{p} = \frac{1}{2} - \frac{1}{2d} \tag{175}$$

which due to (iii) gives $\xi_{ij} = \widehat{u}_i\widehat{u}_j$.
This allows a passage to the limit in the nonlinear term as for any $\psi \in L^2(0,T)$, the following holds

$$\int_0^T b(\widehat{u}_\mu, \widehat{u}_\mu, \widehat{w}_j)\psi dt = -\int_0^T b(\widehat{u}_\mu, \widehat{w}_j, \widehat{u}_\mu)\psi dt$$

Taking the limit and using (175), we obtain

$$b(\widehat{u}_\mu, \widehat{u}_\mu, \widehat{w}_j) \to b(\widehat{u}, \widehat{u}, \widehat{w}_j) \text{ weak in } L^2(0,T)$$

The convergence of all the other terms (linear in u) in the variational formulation is a simple consequence of (i)-(iv). Taking $m = \mu$ in the limit we thus obtain

$$\frac{d}{dt} < \widehat{u}, \widehat{w}_i > + \nu((\widehat{u}, \widehat{w}_i)) + b(\widehat{u}, \widehat{u}, \widehat{w}_i) + b(\widehat{u}, \psi, \widehat{w}_i) + b(\psi, \widehat{u}, \widehat{w}_i) = < \widehat{f}, \widehat{w}_i >$$

The $\widehat{w}_i$ form a basis, hence the result. □

3.2 Time-periodic solutions of the Navier-Stokes equations

Theorem 3.2.1. *Given the functions f and ϕ time periodic with period T, $f \in L^2(0,T;V')$ and ϕ satisfying the property (155), there exists a function $u \in L^2(0,T;V) \cap L^\infty(0,T;H)$ that satisfies*

$$\begin{aligned} \frac{d}{dt} < u, v > + \nu((u,v)) + b(u,u,v) &= < f, v >, \text{ for any } v \in V \\ u(x,t) &= \phi, \text{ in } [0,T] \times \partial\Omega \\ u(0) &= u(T) \end{aligned} \tag{176}$$

Proof. Using the hypothesis of **Theorem 3.1.6** take ψ as in (155) and set $\widehat{u} := u - \psi$. From (176) we obtain

$$\frac{d\widehat{u}}{dt} - \nu\Delta\widehat{u} + \widehat{u}\cdot\nabla\widehat{u} + \widehat{u}\cdot\nabla\psi + \psi\cdot\nabla\widehat{u} + \nabla p = \widehat{f} \tag{177}$$

where $\widehat{f} = f + \nu\Delta\psi - \psi\cdot\nabla\psi - \frac{d\psi}{dt}$, $\widehat{f} \in L^2(0,T;V')$.
We must prove that there is a $\widehat{u} \in L^2(0,T;V) \cap L^\infty(0,T;(L^2(\Omega))^d)$ time-periodic such that

$$< \frac{d\widehat{u}}{dt}, \widehat{u} > + \nu((\widehat{u}, v)) + b(\widehat{u}, \widehat{u}, v) + b(\widehat{u}, \psi, v) + b(\psi, \widehat{u}, v) =< \widehat{f}, v > \tag{178}$$

for any $v \in V$.
We consider a basis $\{\widehat{w}_m\}_{m\geq 1}$ of V and we denote by $V_m := span\{\widehat{w}_1, ..., \widehat{w}_m\}$. Then we can replace the problem (178) by the following **Cauchy** problem in $V_m \times [0,T]$: Find $\widehat{u}_m(t)$ of the form $\widehat{u}_m(t) = \sum_{j=1}^m g_{jm}(t)\widehat{w}_j$ satisfying the initial value problem for the system of ODEs

$$\begin{aligned} \frac{d}{dt} < \widehat{u}_m(t), \widehat{w}_i > + a(\widehat{u}_m, \widehat{w}_i) + b(\widehat{u}_m, \widehat{u}_m, \widehat{w}_i) \quad &+ \quad b(\widehat{u}_m, \psi, \widehat{w}_i) + b(\psi, \widehat{u}_m, \widehat{w}_i) =< \widehat{f}, \widehat{w}_i > \\ \widehat{u}_m(0) \quad &= \quad \widehat{u}_0 \end{aligned} \tag{179}$$

with $\widehat{u}_0$ given, for $1 \leq i \leq m$.
We are going to prove that

$$\textbf{There exists an } R, \text{independent of } m, \text{ such that if } |\widehat{u}_0| \leq R \text{ then } |\widehat{u}_m(T)| \leq R \tag{180}$$

Multiplying (179) by $g_{im}(t)$ and summing over i from 1 to m, we have

$$\frac{du}{dt} < \widehat{u}_m(t), \widehat{u}_m(t) > + \nu((\widehat{u}_m(t), \widehat{u}_m(t))) + b(\widehat{u}_m(t), \psi, \widehat{u}_m(t)) =< \widehat{f}, \widehat{u}_m(t) > \tag{181}$$

or

$$\frac{1}{2}\frac{d}{dt} \parallel \widehat{u}_m(t) \parallel^2 + \nu((\widehat{u}_m(t), \widehat{u}_m(t))) = -b(\widehat{u}_m(t), \psi, \widehat{u}_m(t)) + < \widehat{f}, \widehat{u}_m(t) > \tag{182}$$

But $|b(\widehat{u}_m(t), \psi, \widehat{u}_m(t))| \leq \gamma \parallel \widehat{u}_m(t) \parallel_1^2$ (from **Lemma 3.1.5**) so (182) becomes

$$\frac{1}{2}\frac{d}{dt} \parallel \widehat{u}_m(t) \parallel^2 + \nu((\widehat{u}_m(t), \widehat{u}_m(t))) \leq \gamma \parallel \widehat{u}_m(t) \parallel_1^2 + < \widehat{f}, \widehat{u}_m(t) > \tag{183}$$

Taking $\gamma = \frac{\alpha\nu}{4}$,then the above inequality can be written as

$$\frac{1}{2}\frac{d}{dt} \parallel \widehat{u}_m(t) \parallel^2 + \nu((\widehat{u}_m(t), \widehat{u}_m(t))) \leq \frac{\alpha\nu}{4} \parallel \widehat{u}_m(t) \parallel_1^2 + \frac{\alpha\nu}{4} \parallel \widehat{u}_m(t) \parallel_1^2 + c_1 \parallel \widehat{f} \parallel_{V'}^2 \tag{184}$$

In particular, from Poincaré inequality, we have that $((\widehat{u}_m(t), \widehat{u}_m(t))) \geq \alpha \parallel \widehat{u}_m(t) \parallel_1^2$, which gives

$$\frac{d}{dt}|\widehat{u}_m(t)|^2 + \alpha\nu \parallel \widehat{u}_m(t) \parallel_1^2 \leq 2c_1 \parallel \widehat{f} \parallel_{V'}^2 \tag{185}$$

It follows that

$$e^{\alpha\nu T} \parallel \widehat{u}_m(T) \parallel^2 \leq \parallel \widehat{u}_0 \parallel^2 + 2c_1 \int_0^T e^{\alpha\nu T} \parallel \widehat{f}(t) \parallel_{V'}^2 dt \tag{186}$$

If we divide (186) by $e^{\alpha\nu T}$ we obtain

$$\parallel \widehat{u}_m(T) \parallel^2 \leq e^{-\alpha\nu T} \parallel \widehat{u}_0 \parallel^2 + 2c_1 \int_0^T \parallel \widehat{f}(t) \parallel_{V'}^2 dt$$

The integral term can be bounded and we obtain

$$\parallel \widehat{u}_m(T) \parallel^2 \leq e^{-\alpha\nu T} \parallel \widehat{u}_0 \parallel^2 + c_4 \tag{187}$$

From (187) we conclude that it is sufficient to take R such that

$$R^2 \geq \frac{c_4}{1 - e^{-\alpha\nu T}} \tag{188}$$

to achieve (180).

So the Cauchy problem (179), can be written as an application $\widehat{u}_0 \to \widehat{u}_m(T) = \mathscr{T}_m(\widehat{u}_0)$. Using the Brouwer's fixed point theorem (see [27, page 143]) every continuous map of a closed ball to itself has a fixed point.

So we have that

$$\textbf{There exist } \widehat{u}_{0m} \in B_R \text{ such that } \mathscr{T}_m(\widehat{u}_{0m}) = u_{0m}$$

This gives $\widehat{u}_m(0) = \widehat{u}_{0m}$.

From (180),$\widehat{u}_{0m}$ stays in a bounded subset of H so we have the same estimates as in the case of the initial value problem for the Navier-Stokes equations. In particular, we have that

$$\widehat{u}_\mu \to \widehat{u}(0), \quad \widehat{u}_\mu(T) \to \widehat{u}(T) \text{ in } V' \text{ weak} \tag{189}$$

But $\widehat{u}_\mu(0) = \widehat{u}_\mu(T)$ so we conclude that $\widehat{u}(0) = \widehat{u}(T)$.

□

There are two remarks to be made:

Remark 1 The condition (188) depends on $\widehat{f}$, T,ν and α. The function $\widehat{f}$ must be bounded. Also, if T or ν are too small, R will be very large.

Remark 2 The theorem does not guarante that the periodic solution is unique or asymptotically stable. Numerical simulations indicate that the periodic solution might be stable as well as unstable, depending on the value of the viscosity ν and the period T.

Chapter 4

Numerical study of pulsatile flows

4.1 The numerical methods

As a general method, the Navier-Stokes equations for time-periodic solutions can be discretized through mixed or stabilized finite-element methods combined with a finite-difference time-stepping scheme. This strategy would give rise to a large nonlinear algebraic system where the solutions at all time steps are coupled in an implicit way, a system too large to be solved with the current computational capabilities. A more tractable approach consists in solving a transient problem starting from an initial flow (we use a fluid that is at rest or a steady flow in our case) and iterate in time over the transient flow until the periodic solution is completely set, exactly like what we analyze with the 1-D advection-diffusion equation in Chapter2.
To solve the Navier-Stokes equations we use the SUPG-PSPG formulation as presented in [8]. The classical Galerkin formulation has some weaknesses, such as:

- In case of high order Reynolds numbers, the numerical velocity solution might be polluted with spurious oscillations if the grid is not fine enough to capture all boundary or internal layers across which large velocity gradients exist. This is due to the advection-diffusion character of the momentum equation.

- Equal-order velocity-pressure interpolation leads to spurious pressure wiggles. This is due to the violation of the Brezzi-Babuska-Ladyshenskaya condition for

the underlying Stokes problem.

- The velocity-pressure integrated approach leads to a matrix problem characterized by zero entries on the main diagonal of the system matrix. Therefore, pivoting is required if a direct solver is used.

The viscous incompressible Navier-Stokes equations are given by

$$\begin{aligned} \frac{\partial u}{\partial t} + u \cdot \nabla u + \nabla p - \nabla \cdot (\nu \nabla u) &= f, \quad in \quad \Omega \\ \nabla \cdot u &= 0, \quad in \quad \Omega \\ u &= \bar{u}, \quad on \quad \Gamma_{du} \\ (-pI + \nu \nabla u) \cdot n &= \bar{\theta}, \quad on \quad \Gamma_{nu} \end{aligned} \tag{190}$$

where ν is the kinematic viscosity, f a body force per unit mass, I the identity tensor, n is the outward normal unit vector. The boundary Γ consists of two complementary subsets Γ_{du} and Γ_{nu}, on which the Dirichlet type and Neumann type velocity boundary conditions apply.
The SUPG/PSPG method is a full Petrov-Galerkin formulation, in which a perturbed weight function is applied to all terms in the continuity and momentum equations, i.e. advection, diffusion and source terms as well as the pressure gradient.
We define the trial and weight function spaces for pressure and velocity as

$$\begin{aligned} S_p^h &= \{q^h | q^h \in H^{1h}\} \\ S_u^h &= \{u^h | u^h \in (H^{1h})^d, \quad u^h = \bar{u} \quad on \quad \Gamma_{du}\} \\ V_v^h &= \{v^h | v^h \in (H^{1h})^d, \quad v^h = 0 \quad on \quad \Gamma_{du}\} \end{aligned} \tag{191}$$

where $H^{1h} := \{\phi^h | \phi^h \in C^0(\bar{\Omega}), \phi^h|_{\Omega_e} \in P^1, \quad for \quad any \quad \Omega_e \in \mathscr{T}_h\}$, with Ω_e an element with boundary Γ_e and diameter h_e, $\mathscr{T}_h$ the discretization of the domain Ω.
Then, the SUPG/PSPG method can then be formulated as follows: Find $(u^h, p^h) \in S_u^h \times S_p^h$ such that for any $(v^h, q^h) \in V_v^h \times S_p^h$

$$\begin{aligned} \frac{d}{dt} < u^h, v^h > + (\nabla v^h, \nu \nabla u^h)_\Omega &- (\nabla \cdot v^h, p^h)_\Omega + (q^h, \nabla \cdot u^h)_\Omega \\ + ST = (v^h, f)_\Omega &+ (v^h, \bar{\theta})_{\Gamma_{nu}} \end{aligned} \tag{192}$$

with $ST = \sum_e (\tau_{SUPG} u^h \cdot \nabla v^h + \tau_{PSPG} \nabla q^h, R(p^h, u^h))_{\Omega_e}$. Note that ST contains the residual of the momentum equation $R(p^h, u^h) = u^h \cdot \nabla u^h + \nabla p^h - \nabla \cdot (\nu \nabla u^h) - f$ and some intrinsic time scales τ_{SUPG} and τ_{PSPG}.

The time scales τ_{SUPG} and τ_{PSPG} are usually defined in analogy to the stability parameters for the scalar advection-diffusion and Stokes problems, respectively. For the SUPG part this gives $\tau_{SUPG} := \alpha_u \frac{h_e}{2\|u_h\|}\xi$, where ξ is a function of the element Reynolds number ($Re_h = \frac{\|u_h\| h_e}{2\nu}$) and could be given as $\xi(Re_h) = max[0, min(\frac{Re_h}{3}, 1)]$. Often τ_{PSPG} is taken as $\tau_{PSPG} := \alpha_p \frac{h_e}{2\|u_h\|}\xi$. The typical values for α_u and α_p are between 1 and 5. As opposed to the SUPG part, the PSPG stabilization is still required for low Reynolds numbers.

After we discretize the system in space we obtain a system of ODEs of the form

$$\frac{dU}{dt} = F(U, P)$$

which is solved using an implicit second order Gear time-stepping scheme

$$\frac{\frac{3}{2}U_{n+1} - 2U_n + \frac{1}{2}U_{n-1}}{k} = F(U_{n+1}, P_{n+1})$$

The resulting nonlinear system is solved using PETSC (see [24]) applying the Newton-Raphson's method and a direct LU decomposition at each Newton iteration. As stopping criteria we use the default option given in PETSC with a tolerance of 10^{-10}. The time step is always set to $k = 10^{-2}$. At each time step the solver performs about 6 Newton's iterations.

To find the solution at large Reynolds numbers, we calculate first the solution of the Navier-Stokes equations for a small Reynolds number, starting with a solution at rest. Then, we increase the Reynolds number. For each new Reynolds number we start with the solution obtained at the previous Reynolds number and then iterate over time. Also, at each time step we store the solution obtained at a given point. When the error in the L^2 norm, between the solutions calculated at two consecutive periods is smaller than a given tolerance, we stop. For comparison purposes, on each figure we provide the Womersley number, but we can calculate it from the following formula $Wo = \left(\frac{\pi ReStr}{2}\right)^{\frac{1}{2}}$.

4.2 Periodically driven cavity flows

Periodically driven flows occur in several important applications such as flows in the blood circulatory system, the respiratory system, industrial mixers, etc. For example, the flow of blood in any portion of the arterial tree is driven in a periodic or almost periodic way by the heart from heartbeat to heartbeat. Despite their practical interest, relatively few literature is available on periodically driven flows, and several questions remain open: Why does the structure of periodically driven flows tend to be more complex than steady flows in the same geometry? Under what circumstances a viscous flow driven by periodic boundary conditions ceases to be periodic? Which sequence of bifurcations transforms a periodic periodically-driven flow into a fully turbulent flow?

Most periodically-driven flows that are of physical interests are driven through time-periodic boundary conditions. As a result of the theory developed in Chapter 3 , a periodic solution exists when the boundary is moving in a periodic way, no matter how small is the viscosity ν or how large is the Reynolds number. But the uniqueness and stability of that periodic solution is not guaranteed by the **Theorem 3.2.1**. Few attempts at looking at the stability of periodically-driven flows have been done [3, 19, 33, 20]. To our knowledge, only two papers[3, 33] address the case of a periodic lid-driven 3-D cavity among the abundant literature on lid-driven cavities (for a review see [30]). Those few studies show that periodic periodically-driven flows become unstable while increasing the Reynolds number.

Efficiently computing the periodic solutions for periodically-driven flows is another important problem. Computing periodic flows requires an enormous amount of CPU time compared to the simulation of steady flows on the same mesh. Again a limited literature is available on the computation of time-periodic solution of PDE problems [14, 23], mostly for symmetric PDEs with symmetric operators. A common strategy is to start from some initial solution, compute a transient solution and expect that this transient solution converges to the periodic solution.

Lid-driven cavity problems are standard test cases for the Navier-Stokes equations. For example, bifurcation from steady to periodic solutions have been thoroughly

studied with a steady lid-driven velocity on the upper boundary [10]. To ensure the validity of our code we used one example studied in [10]. This test case will also be a comparison case with the periodic lid-driven examples that we will consider in the following.

4.2.1 Steady lid-driven cavity

As mentioned before, the square cavity problem is one of the most standard test case used for the analysis of numerical methods for the Navier-Stokes equations. Although it is not possible to give an analytic solution, the geometry is so simple that most numerical codes have been tested on this problem. It is relatively easy to calculate solutions at high Reynolds numbers with a good precision.
The problem states as: Find the velocity u and the pressure p that satisfy the equation (190). The domain Ω is the unit square $[0,1] \times [0,1]$ and as boundary conditions we assume

$$\begin{aligned} U(x,y,t) &= (0,0), \text{ if } y < 1 \\ U(x,y,t) &= (1,0), \text{ if } y = 1 \end{aligned}$$

The boundary conditions are singular at the upper corners. We have assumed that the velocity is $(1,0)$ on the upper wall, including both corners.
We have used a mesh with $100 \times 100 \times 4$ elements, a finer grid than the meshes used in the article [10]. The streamlines are represented in **Figure 5** and the results are similar to those obtained by [10]. A close look at the solution shows a slight pulsation of the corner vortices on the left wall. These two vortices interact among themselves, while the core of the flow remains almost stationary. When the Reynolds number is further increased, the amplitude of the oscillations increases. At $Re = 8000$, just after the Hopf bifurcation has taken place, the numerical solution tends to stabilize to a time-periodic solution as can be seen in **Figure 6**, where the horizontal velocity at the point $(0.2, 0.5)$ (a point closed to the left wall) is ploted at each time step. We know from [10] that the critical Reynolds number Re_{cr} for the square lid-driven cavity is above 8000 and this result is confirmed by our experiments.

4.2.2 Periodically time-symmetric lid-driven cavity

A tractable approach to compute time-periodic flows consists in solving a transient problem starting from an initial flow (e.g. using a fluid initially at rest) and iterate in time over the transient flow until the periodic solution is completely set, exactly like what we analyze for the advection-diffusion equation in **Chapter 2**. In the paper of Rosenfeld [25], the numerical experiments showed that the number of periods necessary to reach a periodic solution depends on the Reynolds number Re but also on the Strouhal number Str. This is also in agreement with our linear stability analysis.

In this test case, the boundary conditions are time-periodic and they are given by:

$$\begin{aligned} U(x,y,t) &= (0,0), \text{ on the boundary where } y<1 \\ U(x,1,t) &= (\cos(2\pi t/T),0) \end{aligned}$$

where T is the period. The lid is driven in a periodic fashion by time-symmetric boundary conditions in the sense that $U(x,1,t+T/2) = -U(x,1,t)$ for all t.

Period T=1, Str=1

The mesh we consider has $200 \times 200 \times 4$ elements which increase the CPU time to 46 hours per period.

For that test case we calculated the solutions at $Re = 3000$, 5000, 8000 and 12000 and the streamlines of the velocity fields are shown in **Figure 7**, **Figure 8**, **Figure 9** and **Figure 10**. The results show clearly that larger Re induce more pronounced vortices at the left and right walls. At $Re = 8000$ and $Re = 12000$ on **Figure 9** and **Figure 10**, multiple vortices appear close to the left wall.

In **Figure 11** to **Figure 18**, the time-periodic solution is shown at a full, quarter, half and three quarters of a period within a time period interval. At the beginning of the period $t = 14T$, as seen in **Figure 11** and **Figure12**, pronounced vortices at the upper corner of the left and right wall are observed. This corresponds to the time where the lid moves with the largest positive x-velocity. There are two vortices at the left wall, the large one is moving counterclockwise and the other one clockwise. The vortex at the right moves in a clockwise direction as it is the vortex the closest

to the lid. In **Figure 11** the streamlines are colored with respect to the x-velocity. As we can see the highest value of the x-velocity is at the top of the cavity. **Figure 12** presents the streamlines colored by the y-velocity and it is easier to observe the fluid motion and the vortices that appear.

At $t = 14T + \frac{T}{4}$, the upper wall is at rest. As we can observe in **Figure 13** and **Figure 14** there are only two vortices, one close to the upper left corner and the other one at the upper right corner. The orientation of these two vortices remain the same as at the beginning of the period. The fluid descends mostly on the right wall. When we reach half of the period, the upper wall has a horizontal velocity of -1,(see **Figure 15**), meaning that the motion of the moving lid is reversed. The fluid has two corner vortices and descends at the left wall as we can see in **Figure 16**.

In **Figure 17** and **Figure 18**, at the three-quarters of a period, the upper boundary is at rest. The fluid has only a nearly reversed behavior as opposed to the case of a quarter of a period.

After one complete period, at $t = 15T$, on **Figure 19** and **Figure 20**, the flow returns almost to the same state as it was at $t = 14T$ and the solution seems to be time-periodic. Further investigations have been conducted for $Re = 8000$, value at which a bifurcation of the solution was observed in the steady lid-driven cavity test. The x-velocity computed at the point $(0.2, 0.75)$ (close to the upper left corner), shows a time periodic behavior, as can be seen on the time history of the x-velocity presented in **Figure 21** for $Re = 8000$ and **Figure 22** for $Re = 12000$. If $Re = 8000$, the difference between the solutions at period 13 and period 14 is of order 1.001×10^{-4} in the L^2 norm. That means we are close to a time-periodic solution. In **Figure 23** we represented the y-Velocity with respect to the x-Velocity for the last four periods, when $Re = 8000$. The solutions are almost overlapping, meaning we are close to a time-periodic solution. In the case of $Re = 12000$, the solution is almost periodic as it can be observed from **Figure 22** and **Figure 24** but of course more periods are needed to confirm the exact periodicity of the solution. The difference between the solutions at period 9 and 8 is of order 10^{-3}. From the linear analysis we need at least 20 periods to reach a time-periodic solution for $Re = 8000$ and 30 periods for $Re = 12000$, assuming a difference of 10^{-8} in the solution from period to period.

Period T=10, Str=0.1

With a period of $T = 10$, the solutions for $Re = 5000$ and $Re = 8000$ are presented in **Figure 25** and **Figure 26**, respectively. There are four main vortices each one close to a corner of the square and another two small vortices on the top right and bottom right. The difference between these two solutions is not so large, the solution at $Re = 8000$ has a larger lower right vortex compared to the solution at $Re = 5000$. On **Figure 27** to **Figure 30**, the time-periodic solution is shown at a full, quarter, half and three quarters of a period for a $Re = 5000$. At the beginning of the period $t = 11T$, on **Figure 27**, there are four vortices, two of them moving counterclockwise and the others, clockwise. The vortex at the top left corner moves in a counterclockwise direction, while the vortex at the top right corner moves in a clockwise direction. At $t = 11T + \frac{T}{4}$, the upper wall is at rest. As we can observe in **Figure 28** the vortex situated at the bottom left corner has moved to the center of the square, while the big vortex at the bottom right corner retracts to the right. There is also a new small vortex situated at the right wall. The orientation of the four big vortices remains the same as at the beginning of the period.

On **Figure 29**, when we reach half of the period, the upper wall has an horizontal velocity of -1, that means the motion of the moving boundary is reversed. The small right vortex disappeared. The solution is nearly reversed compared to the solution on **Figure 27** which means a possible break-up in the space-time symmetry. The size of the four vortices changes from full period to half period.

In **Figure 30**, at the three-quarters of a period, the upper boundary is at rest. The small vortex at the right wall, from **Figure 28**, disappeared . The fluid has an almost reversed behavior as opposed to the solution at a quarter of a period, but not exactly the same.

In case we increase the Reynolds number to $Re = 8000$, the behavior of the solution within one period does not change very much, as we can see from **Figure 31**, **Figure 32**, **Figure 33** and **Figure 34**, comparing with the case of $Re = 5000$.

We must mention that we modified the mesh, taking a smaller number of elements $100 \times 100 \times 4$ because of the long CPU time required for a mesh of $200 \times 200 \times 4$

elements which was used in the case of a period of $T = 1$. The number of time steps per period is 1000.

In **Figure 35** the x-velocity at the point (0.8,0.5) is represented in the case of $Re = 5000$ and in **Figure 36** the horizontal velocity was calculated for $Re = 8000$. When $Re = 5000$, the difference between period 7 and 6, in the L^2 norm, is of order 10^{-2}, while in the case of $Re = 8000$ a time periodic solution is not obtained even after 20 periods. This fact is more obvious if we look at the graph of the y-velocity versus the x-velocity. In the case of $Re = 5000$, the solutions are close to each other, even if they are not perfectly overlapping as we can see in **Figure 37**. When $Re = 8000$, the solutions calculated at the last four periods are far from overlapping, see **Figure 38**, so no time-periodic solution has been obtained up to time $t = 20$. According to the linear spectral analysis performed in Chapter 2 for the 1-D advection diffusion problem, a minimum of 20 periods is needed to obtain a time-periodic solution for $Re = 8000$ and 15 periods for $Re = 5000$ if we assume a difference of 10^{-8} in the solution from period to period. There are two possibilities, either we need to perform more than 20 periods or we are around a critical Reynolds Re_{cr} for a bifurcation.

4.2.3 Time-asymmetric periodically lid-driven cavity

In the introduction we presented several ways a solution can lose its stability and becomes unstable. One of the possibilities is to break the space-time symmetry of the boundary conditions and excite an unstable mode appearing after the bifurcation of the time-periodic solution. We change the boundary conditions so that they will not be symmetric in time, by taking

$$\begin{aligned} U(x,y,t) &= (0,0), \text{ if } y < 1 \\ U(x,1,t) &= (max(\cos(\frac{2\pi t}{T}),0),0) \end{aligned}$$

As before we consider two test cases, one with $T = 1$ and the other one with $T = 10$.

Period T=1, Str=1

The solution at $Re = 5000$, **Figure 39**, is in a way different from the solution at

$Re = 8000$, **Figure 40**. Both of them have a large recirculation area in the middle of the domain and a small vortex at the bottom near the right corner, but the center of the big vortex at $Re = 8000$ is situated closer to the center of the domain. Also the small right bottom corner vortex is larger when $Re = 8000$.

At $Re = 5000$, within one period there is not much change in the solution's streamlines as can be seen on **Figure 41** to **Figure 44**. At the beginning of the period T, the upper wall has a maximum velocity of 1. The velocity of the lid decreases from $t = 6T$ to $t = 6T + \frac{T}{4}$, resulting in reduced speed of the flow without much impact on the qualitative aspect of the streamlines. From $6T + \frac{T}{4}$ to $6T + \frac{3T}{4}$ there is no motion induced by the lid. The flow keeps dissipating energy and slowing down. At $6T + \frac{3T}{4}$ there are two new vortices appearing at the left bottom corner and at the left upper corner as we can see on **Figure 44**. The corner vortex at the bottom right reaches its maximal extend just before the lid starts moving again. From $6T + \frac{3T}{4}$ to $7T$ the lid's velocity rises again.

The solutions at full,quarter, half and three quarters of a period for $Re = 8000$ are represented on **Figure 45** to **Figure 48**. The solution does not change too much within one period, in a similar fashion as for the flow at $Re = 5000$. The secondary vortex at the right bottom corner changes its size during one period. At $30T + \frac{3T}{4}$ we notice the appearance of two vortices, at the left top and bottom corners as seen on **Figure 48**.

The mesh used here, consists of $200 \times 200 \times 4$ elements, the same as for the case of the time-symmetric periodically lid-driven cavity with $Str = 1$.

At $Re = 5000$, on **Figure 49** and **Figure 51** we have not iterated over many periods so we might still be in a transient state. The 1-D spectral analysis tell us that we need to perform at least 15 periods for $Re = 5000$ to obtain a time-periodic solution. The horizontal velocity calculated at the point $(0.2, 0.75)$ near the top left corner for $Re = 8000$ does not stabilize after 35 periods as we can see in **Figure 50**. The graph of the y-Velocity with respect to the x-Velocity, **Figure 52** for the last 4 periods is far from overlapping from one period to another. At $Re = 8000$ the solution is far from being stabilized. According to the 1-D spectral analysis, we need at least 20 periods to obtain a time periodic solution for $Re = 8000$. We might be around a

critical Reynolds Re_{cr} for a bifurcation point.

Period T=10, Str=0.1

The solution at $Re = 5000$, **Figure 53** presents a main clockwise rotating vortex in the center of the domain and three secondary vortices, two of them at the bottom left and right corner and one at the top close to the right wall. At the right bottom corner we can notice the existence of a ternary vortex. The solution at $Re = 8000$ has the same structure, except that the main vortex has its center closer to the center of the domain and there are two small vortices (a secondary and a ternary one) at the left bottom corner (see **Figure 54**).

Solutions at the full, quarter, half and three quarters of a period are represented on **Figure 55** to **Figure 58** for $Re = 5000$. At the beginning of the period $19T$, the upper wall has a maximum velocity of 1. From $19T$ to $19T + \frac{T}{4}$ the velocity of the lid decreases and the right upper corner vortex is drained by the moving lid into the core vortex, which recirculates and damps it over the rest of the period as we can see in **Figure 56**. Also the flow slows down and energy dissipates, creating a new small vortex situated at the top left wall. The ternary vortex at the right bottom corner disappears. From $19T + \frac{T}{4}$ to $19T + \frac{3T}{4}$, there is no motion induced by the boundary and at $19T + \frac{T}{2}$, on **Figure 57**, we see the small left top vortex increasing to dissipate the kinetic energy. A new right top corner vortex starts to grow while the remains of the upper right corner vortex can be found in the main vortex. At $19T + \frac{3T}{4}$, **Figure 58**, the boundary is still at rest and the solution is almost the same as the solution at half of the period. The secondary corner vortices situated at the left and right bottom corners pulsate over the period, with the peak lid velocity inducing a maximal vorticity in the core vortex and in return producing a ternary vortex at the lower right corner. The top left corner vortex which appears when the lid stops moving, slowly decreases when the lid starts to move again, to eventually completely disappear when the lid reaches its maximal velocity.

Solutions at full, quarter, half and three quarters of a period are represented on **Figure 59** to **Figure 62**, for $Re = 8000$. There are only minor differences between the

solution at $Re = 5000$ and at $Re = 8000$. At $t = 16T + \frac{T}{4}$ on **Figure 60**, the secondary left bottom corner vortex is replaced by two small vortices. At $t = 16T + \frac{T}{2}$, on **Figure 61**, the small right top vortex moves closer to the center of the domain. It is almost at the center of the domain, see **Figure 62** at $t = 16T + \frac{3T}{4}$.
The mesh used here is of $100 \times 100 \times 4$ elements, the same as the mesh used for the time-symmetric problem with $Str = 0.1$.
The horizontal velocity calculated at the point $(0.8, 0.5)$ for $Re = 5000$ and $Re = 8000$ are showed in **Figure 63** and **Figure 64**. In both cases the solution does not seem to stabilize after 20 and 16 periods, respectively. The y-velocity with respect to the x-velocity for the last four periods does not stabilize as we can see in **Figure 65** and **Figure 66**. According to our 1-D spectral analysis, a minimum of 20 periods must be performed to obtain a time-periodic solution for $Re = 8000$ and 15 periods for $Re = 5000$, with a difference of 10^{-8} in successive periods. We should consider two possibilities, either we need to continue calculations until a time-periodic solution is obtained or we are around a critical Reynolds Re_{cr} for a bifurcation .

4.2.4 Comparison of solutions at $Re = 8000$

The last analysis made on the lid-driven cavities is a comparison between the solutions obtained at $Re = 8000$, in all four cases, and the solution obtained in the steady lid-driven cavity case.
When the boundary conditions on the upper boundary are time-periodic and time-symmetric, we use as time reference, the time where the lid reaches its peak positive velocity. The core vortex which can be seen on **Figure 5** becomes much smaller, see **Figure 67** and **Figure 68**. On **Figure 67**, the solution at $Str = 1$ has in fact two main vortices situated at the top left and right corners. A third vortex appears close to the left wall. The solution at $Str = 0.1$ has four main vortices at the top and bottom right and left corners, as in **Figure 68**.
When we apply an asymmetric time-periodic conditions on the upper boundary, the solutions at $Str = 1$ and $Str = 0.1$, represented in **Figure 69** and **Figure 70**, have a core vortex, very much like in the case of steady lid-driven cavity, see **Figure 5**.

The left top corner vortex of **Figure 5** disappears. When $Str = 1$, the secondary left bottom vortex also disappears as we can see on **Figure 69**. On **Figure 70**, the solution at $Str = 0.1$ does not have the top left corner vortex but it has a new right top corner vortex. There are still the two secondary vortices situated at the bottom left and right corners. We can see also the appearances of another two ternary vortices at the bottom left and right corners.

If we compare the x-velocity at $Str = 1$, (see **Figure 21** and **Figure 50**) with the x-velocity at $Str = 0.1$, (see **Figure 36** and **Figure 64**), it seams that a short period gives rise to a flow response closer to a sinusoidal wave than a long period, even in the case of the time-asymmetric cosines boundary conditions. Also, looking at **Figure 21** and **Figure 50**, we notice that in the case of time-asymmetric boundary conditions it is harder to achieve a time-periodic solution. The transient is longer or a bifurcation to a time-periodic solution is more likely to appear. If we look on the effect produced by a longer period, we notice a period of $T = 10$ produces a less stable periodic solution as we can see on **Figure 35** and **Figure 63** compared with a period of $T = 1$ on **Figure 49**, for $Re = 5000$. The same phenomena happens for $Re = 8000$ if we compare **Figure 36**, **Figure 64** with **Figure 21** and **Figure 50**.

4.3 Pulsatile flow in a constricted channel

Atherosclerosis is a disease of the cardiovascular system which involves hardening of arteries due to the deposition of fat. Atherosclerotic constrictions in arteries are known as arterial stenoses and they are found especially in the internal carotid artery which supplies blood to the brain, cardiac muscle and the femoral artery which supplies blood to the lower limbs. Moderate as well as severe stenoses can have long term health consequences. First, the presence of a constriction results in head losses which can reduce the blood supply through the artery and also impose additional load on the heart. The pressure losses are significant only when the internal diameter is reduced beyond half of the nominal value (see [21]).

The fluid dynamics of the post-stenotic flow plays an important role in the progression of the atherosclerosis and therefore we concentrate our experiments on the flow

motion in a stenosis. The geometry of the computational domain is composed of two straight parallel plates which have been "squeezed" in the middle. In our studies, the channel has been modified at the upper and the lower wall, comparing with previous studies (see [21] and [25]) where the modifications are made just for the upper wall. The effects of the constriction size and the waveform will not be considered. Under these conditions two non-dimensional parameters, the Reynolds and Strouhal numbers govern the flow field ($Re = \frac{U_m d}{\nu}$, $Str = \frac{d}{TU_m}$). The mesh is shown in **Figure 71**. We start our computations from a steady solution which we compute first and then we march in time until a time-periodic flow was attained. We play with different values of the Reynolds number with ranges from $Re = 200$ to $Re = 1200$ and different values of the Strouhal number, $Str = 0$ to $Str = 2$. The portion of the artery has an adimensional length of 5 and a width of 1. The ratio of the diameter at the stenosis compared to the diameter of the unconstricted channel is 1/2. The number of elements is $200 \times 40 \times 4$.

4.3.1 Flow in a constricted channel with steady inflow

First we compute a flow with the inflow $u(0, y, t) = [U(0, y, t), 0]$ where $U(0, y, t)$ is given by

$$U(0, y, t) = 1.0$$

We consider no slip boundary conditions at the upper and lower boundary and free exit at the outflow. The solutions are calculated for $Re = 200$, $Re = 400$ and $Re = 1200$ and are shown on **Figure 72**, **Figure 73** and **Figure 74**, respectively. The solution presents two vortices, right after the constriction. These vortices increases as Re increases. When $Re = 200$ and $Re = 400$ the solutions are nearly symmetric with respect to the axis of the pipe, as we can see in **Figure 72** and **Figure 73**. When $Re = 1200$, the symmetry with respect to the x-axis is broken which is most likely the consequence of a bifurcation. The size of the vortices grows with Re probably resulting in a less stable flow for higher Re numbers. When $Re = 1200$, the horizontal velocity at the point $(3.2, 0.75)$, a point just after the constriction where some vorticity appears, is represented on **Figure 75** and **Figure 76**. The x-velocity presents very

large variations at the beginning of the simulations but then it tends to decrease. Through a closer look over a smaller time interval (see **Figure 76**), one can see that the solution at that point is likely to be periodic. This could result from a bifurcation from a steady to a periodic solution while increasing Re. Therefore, our future calculations will experiment with Reynolds numbers up to $Re = 1200$.

4.3.2 Flow in a constricted channel with time-periodic inflow

The incoming axial velocity velocity is set to

$$U(0, y, t) = 1 - \sin(\frac{2\pi t}{T})$$

where T is the period. We consider three cases, one with a period $T = 1$, one with period $T = 0.5$ and another with period $T = 2$.

Period T=1, Str=1

At different Re the streamlines of the solution look like those in **Figure 77** for $Re = 200$, **Figure 78** for $Re = 400$ and **Figure 79** for $Re = 1200$. There are four vortices that can be observed, two of them right after the constriction and the other two further downstream in the channel. Their size decreases as Re increases. The solutions are almost symmetric about the line $y = 0.5$.

It is interesting to see what happens with the solution within one period. The results are presented for $Re = 400$ in figures **Figure 80**, **Figure 81**, **Figure 82** and **Figure 83**. At the beginning of a period $8T$, the solution presents four vortices, two of them just after the constriction. This situation corresponds to an axial velocity of 1. Follows a deceleration phase, up to $8T + \frac{T}{4}$ where the inflow axial velocity reaches its minimal value of 0. At that time, the flow exhibits large vortical structures both upstream and downstream of the constriction. From $8T + \frac{T}{4}$ to $8T + \frac{3T}{4}$ there is an acceleration phase. The incoming velocity is back to the value of 1 at $8T + \frac{T}{2}$. All the large vortices created during the peak systole have been washed out by the rapid axial flow. Only two small vortices remain on the downstream side of the constriction. The velocity is at its maximum when $t = 8T + \frac{3T}{4}$. This c orresponds to the peak systole. The flow looks very much like a Poiseuille flow, except for the small

disturbance created by the constriction.

The same phases can be observed when $Re = 1200$ on **Figure 84**, **Figure 85**, **Figure 86** and **Figure 87**. Symmetry is even less apparent at the peak diastole, at $11T + \frac{T}{2}$ as some large vortices that were present at $Re = 400$ break into smaller vortices. We might be above a bifurcation point.

The horizontal velocity at the point $(3.2, 0.75)$ for $Re = 400$, **Figure 88**, seems periodic, with a difference between solution at successive periods of 10^{-2} in L^2 norm, while in the case of $Re = 1200$ (**Figure 89**) the solution has not reached a periodic state after 12 periods. The y-velocity with respect to the x-velocity is represented on **Figure 90** and **Figure 91** for $Re = 400$ and $Re = 1200$, respectively. On **Figure 90** the solutions at the last three periods are shown. As we can see they are close to each other, almost overlapping. On **Figure 91** the solutions for the last four periods appear to be further apart from each other, as could result from the bifurcation of a periodic solution to a non-periodic solution. This would have to be confirmed by simulations over more periods, to be sure that the solution has gone over the transient.

Period T=0.5, Str=2

At different Re the streamlines of the solution look like those in **Figure 92** for $Re = 200$, **Figure 93** for $Re = 400$ and **Figure 94** for $Re = 1200$. There are six vortices that can be observed, four right after the constriction and other two downstream the channel. The two vortices situated close to the constriction seem to increase as Re increases. The solutions look symmetric about the line $y = 0.5$.

The solution within one period is presented for $Re = 400$ on **Figure 95**, **Figure 96**, **Figure 97** and **Figure 98**. At the beginning of a period $3T$, the solution presents six vortices, four of them just after the constriction, this situation corresponds to an axial velocity of 1. Follows a deceleration phase, when the inflow velocity decreases to 0 at $3T + \frac{T}{4}$. At that time, the flow is reversed after the constriction. At peak diastole there are six larger vortices, compared to fewer vortices for the case of $Str = 1$. From $3T + \frac{T}{4}$ to $3T + \frac{3T}{4}$ there is an acceleration phase, the incoming velocity is 1 at $3T + \frac{T}{2}$ and we notice the increase in the number of vortices after the constriction. The velocity is at its maximum when $t = 3T + \frac{3T}{4}$. It can be remarked an increase

in the number of vortices at $3T + \frac{T}{4}$ and at $3T + \frac{T}{2}$ for $Str = 2$ compared to the case $Str = 1$.

The same phases can be observed when $Re = 1200$, **Figure 99**, **Figure 100**, **Figure 101** and **Figure 102**. There are some slight modifications in the streamlines compared to the case of $Re = 400$, in the sense that the number of vortices increases.

The horizontal velocity at the point $(3.2, 0.75)$ for $Re = 400$ (**Figure 103**) becomes periodic, with difference between solution at successive periods of 10^{-2}, while in the case of $Re = 1200$, **Figure 104**, the solution has not reached a periodic state after 10 periods. On **Figure 105**, the graph of the y-velocity with respect to the x-velocity for the last four periods shows that solutions are close to each other, so we might be close to a time-periodic solution. On **Figure 106**, the solutions do not stay close to each other so we did not obtain yet a time-periodic solution. It is possible that we are above a bifurcation point.

Period T=2, Str=0.5

The solution at $Re = 400$ is shown on **Figure 107**. We can see four vortices close to the constriction, two of them larger and two smaller. Within one period we can observe the two large vortices at $6T + \frac{T}{4}$ and at $6T + \frac{T}{2}$, on **Figure 108** and **Figure 109**, respectively. At peak systole, on **Figure 110**, there are no vortices, they have been washed up by the rapid axial flow.

The x-velocity is represented on **Figure 111** and the y-velocity with respect to x-velocity is shown on **Figure 112**. The second graph shows clearly that the solutions of the last two periods almost overlap and we are very close to a time-periodic solution.

4.3.3 Comparison of solutions at $Re = 400$

On **Figure 113** to **Figure 115** we compare the solutions obtained at $Re = 400$ and for $Str = 0.5$, $Str = 1$ and $Str = 2$. The large two vortices rig ht after the constriction from **Figure 113** become smaller and smaller when we increase the Strouhal number Str. For $Str = 2$ we notice these vortices are very small and they basically change into four small vortices. Also, if we compare the solutions at peak diastole,

we observe that for small $Str = 0.5$, on **Figure 108** there are two large vortices right after the constriction . These vortices decrease in size when $Str = 1$, **Figure 81** and they become very small when $Str = 0.5$, **Figure 96**. In all three cases it seems that we are close to a time-periodic solution, as we can observe from **Figure 105**, **Figure 90** and **Figure 112**.

4.3.4 Blood flow in an artery

As presented at the beginning of the thesis, a nondimensional frequency parameter, the Womersley number, governs the relationship between the inertial and viscous forces for blood flows in arteries. This parameter is used widely in the description of cardiovascular flows. The Womersley number is given by $Wo = (\frac{\pi ReStr}{2})^{\frac{1}{2}}$ and corresponds to the non-dimensional frequency of the inlet flow pulsation. The simulations done so far in this section used a uniform velocity profile varying sinusoidally in time at the inlet. However, the pulsatile flow profile in a channel is different from a uniform or parabolic profile for Womersley numbers greater than one.

In [21], the authors suggest that reasonable inflow conditions can be obtained as a solution of the following equation:

$$\frac{\partial U}{\partial t} - \nu \frac{\partial^2 U}{\partial y^2} = -A - Be^{\frac{i2\pi t}{T}}$$

where A and B correspond to the steady and oscillatory pressure gradients (see [21]), T is the period and $U(x, y, t)$ is the horizontal velocity.

The solution of the above equation is given by (see [21])

$$U(y,t) = \frac{3}{4}\left(1 - 4(y-0.5)^2\right) + \frac{B}{A} - if(Wo)\left(1 - \frac{\cosh(2Wo\sqrt{i}(y-0.5))}{\cosh(Wo\sqrt{i})}\right)$$

where $f(\alpha)$ is a function of α which appears as a consequence of matching the volume flux conditions (see [29]).

The ratio of the length of the channel with respect to the width is 8:1. The mesh is increased to $400 \times 80 \times 4$ elements and the constriction appears close to the beginning of the channel. The experiments done so far in this study considered a shorter

channel, but we want a perspective on what happens with the flow downstream of the constriction, in case the channel is longer and the inflow boundary conditions are varied. The velocity profile at the inflow is given in **Figure 116** within one period. The horizontal velocity at a point, in this case $(4.02, 0.875)$, for $Re = 400$ and $T = 1$ is pictured in **Figure 117**. As we can see, after 11 periods we have not reached a time-periodic solution. The solutions at time $t = 6$ and $t = 11$ are represented in **Figure 118** and **Figure 119**, respectively. We can notice the appearence of some vortices after the constriction. These vortices are slightly different from those observed with the shorter pipe (compare **Figures 118** and **Figure 119** with **Figure 78**). More interestingly, with the longer pipe, the vortices are advected further downstream, and their size and number keep growing with time. This suggest that we should continue our simulations for that test case. The use of a longer pipe in all our test cases would have been desired, but would have somewhat limited our ability to vary the Reynolds and Strouhal numbers given the large CPU time then required. On the other hand, the inflow boundary conditions do not seem to have a very strong impact.

Chapter 5

Summary and conclusions

5.1 Summary of the research and conclusions

This thesis presents a theoretical and numerical study of time-periodic parabolic problems with an emphasis on the Navier-Stokes equations. More specifically,

- We extended previous results on the existence and stability of time-periodic solutions for periodically forced parabolic equations to the case of non-symmetric and time-dependent operators. We obtained an error estimate for finite element methods approximating those time-periodic parabolic problems.

- The results are true only when the projection operator defined from some Sobolev space to the finite-element subspace has some special properties and when the bilinear form, associated to our operator, is coercive. We proved that the projection operator associated to the advection-diffusion operator has these special properties, even when the advective velocity is time-dependent. The handling of a time-dependent advective velocity required a special Aubin-Nitsche argument that we have not seen in the literature.

- We extended that general theory to the time-periodic Stokes problem. Even if we only obtained an error estimate on the velocity, that extension required some care to properly handle the pressure.

- The 1-D advection-diffusion problem has been studied as an example of a linear problem. First, a numerical study of an advection-diffusion problem has been done in the presence and in the absence of coercivity. The absence of coercivity did not produce a time-periodic solution, indicating the necessity of the coercivity to guarantee the existence of a time-periodic solution under time-periodic forcing, even in the linear case. Second, through a spectral analysis of the 1-D advection-diffusion problem, we identified two relevant parameters, namely the local Peclet Pe_h and the CFL number λ, controlling the convergence of the solution of the initial value problem toward the solution of the time-periodic problem. Numerical experiments for different values of these two parameters gave us an idea on the number of periods needed to obtain a time-periodic solution. Through comparison with published results on time-periodic flows, we verified that the linear stability analysis provides a lower bound on the number of periods needed to reach a periodic viscous incompressible flow within a given accuracy. Finally, a spectral analysis of the advection-diffusion operator on a bounded interval showed that the length of the domain, the advective velocity and the diffusion coefficient all have impact on the decay rate of the transient solution toward the periodic solution.

- We obtained the existence of a solution for the initial boundary value problem for the Navier-Stokes equations subject to non-homogeneous Dirichlet boundary conditions by merging two proofs available in the literature, one is the proof of the existence of a steady solution for the Navier-Stokes equations subject to non-homogeneous Dirichlet boundary conditions and the other is the proof of the existence of a unsteady solution for the Navier-Stokes equations subject to homogeneous Dirichlet boundary conditions. Those two proofs are available in books, but we have not found anywhere the proof for the initial boundary value problem with non-homogeneous Dirichlet boundary conditions. Using that result, we proved the existence of a time-periodic solution for the Navier-Stokes problem with time-periodic non-homogeneous Dirichlet boundary conditions,

extending a previous result of Lions where only homogeneous boundary conditions were considered. The solution exists but we do not know if the solution is stable or unique.

- Numerical experiments for the 2-D lid-driven cavity were carried out for time-symmetric and time-asymmetric periodically driven problems. In each case we considered two relevant parameters, the Reynolds and the Strouhal numbers. The Reynolds number was varied over a range of 5000 to 8000 and the Strouhal number considered were 1 or 0.1. For the time-symmetric case, when $Str = 1$, we notice that the solution tends to be time-periodic. If $Str = 0.1$ the solution seems to lose its periodicity. The analysis of the streamlines within one period showed that the time-symmetry could be broken. We might be above the critical Reynolds number for a bifurcation. When we break the time-symmetry of the boundary conditions, the solution for both $Str = 1$ and $Str = 0.1$ does not seem to be time-periodic at $Re = 5000$ or at $Re = 8000$. Looking at the solution within one period, we could not observe any time-symmetry.

- In all cases, the solutions of cavity flows with a time-periodic lid differ very much from the usual steady lid-driven cavity flows, with the larger differences observed when the lid eventually reverses the direction of its movement (time-symmetric cases). In that latter case, we observed that the large vortex appearing in the steady lid disappears. The solution then has a totally different structure with four equal-size vortices, in case the period is long enough (when $Str = 0.1$).

- The study of 2-D flows in a stenosis has been done using a time-periodic inflow. Three different cases were considered, $Str = 1$, $Str = 2$ and $Str = 0.5$. The critical Reynolds number to lose the time-periodicity of the flow seems to be around $Re = 1200$. The stenosis allows the appearance of some vortices, the size of these vortices depending on the Strouhal number.

5.2 Recommendations for future work

The analysis of the stability and uniqueness of the time-periodic solution for the Navier-Stokes equations under periodic forcing would be an interesting but difficult avenue. It would also be interesting to do a more comprehensive qualitative stability analysis of some of the sensitive cases identified in the thesis, e.g. the time-symmetric periodically lid driven cavity with $Str = 0.1$ and $Re = 8000$, all time-asymmetric lid driven cavity problems and the flows in the stenosis near $Re = 1200$. One way to clarify whether or not we are close to a bifurcation point would be to perform a Floquet analysis. Also, we should consider 3-D experiments with more complicated geometries closer to real life arteries.

Bibliography

[1] C.K.Aidun, N.G. Triantafillopoulos, J.D. Benson: *Global stability of a lid-driven cavity with through flow: Flow visualization studies*, Phys. Fluids, A 3: 2081-91, (1991)

[2] B.F. Armaly, F.T. Durst,. F.J. Pereira, B. Schnonung: *Experimental and theoretical investigations of backward-facin g step flow*, J.Fluid Mech. 127, 473-496, (1983)

[3] H.M. Blackburn and J.M. Lopez:*The onset of three-dimensional standing and modulated traveling waves in a periodically driven cavity flow*, J. Fluid Mech. 497, pp. 289-317, (2003)

[4] C. Bernardi: *Numerical approximation of a periodic linear parabolic problem*, SIAM J. Numer. Anal., vol. 19,no. 6, December, (1982)

[5] P.S.Casas and A.Jorba: *Hopf bifurcations to quasi-periodic solutions for the two-dimensional Poiseuille flow*, preprint version, Universidad Politécnica de Cataluna

[6] P.G. Ciarlet:*The Finite-Element methods for elliptic problems*, Elsevier North-Holland, (1978)

[7] E.A. Coddington, N. Levinson:*Theory of Ordinary Differential Equations* Mc Graw-Hill, (1955)

[8] T. De Mulder: *Stabilized finite element methods (SUPG,GLS,...) for incompressible flows*, Lecture Series, von Karman Institute for Fluid Dynamics, March 3-7, (1997)

[9] A. Ern, Jean-Luc Guermond:*Theory and Practice of Finite Elements*, Chapter 6, Springer-Verlag, (2004)

[10] A. Fortin, M. Jardak and J.J. Gervais: *Localization of Hopf bifurcations in fluid flow problems*, Int. J. for Numerical Methods in Fluids 24, pp. 1185-1210, (1997)

[11] Y.C.Fung: *Biodynamics: Circulation*, New York, Springer-Verlag, (1984)

[12] V.Girault, P.A Raviart: *Finite Element Approximation of the Navier-Stokes Equations* Lecture Notes in Mathematics,Springer-Verlag, (1979)

[13] J. Guckenheimer, B. Meloon: *Computing periodic orbits and their bifurcations with automatic differentiation*, SIAM J.Sci. Comput., Vol. 22, No.3, pp . 951-985, (2000)

[14] A.Hansbo:*Error estimates for the numerical solution of a time-periodic linear parabolic problem*,BIT 31, pp. 664-685, (1991)

[15] T.J.R. Hughes and M. Mallet: *A new finite element formulation for computational fluid dynamics: III The generalized streamline operator for multidimensional advective-diffusive systems*, Computer Methods in Applied Mechanics and Engineering 58, pp. 305-328, (1986)

[16] K. Lust: *Numerical bifurcation analysis of periodic solutions of partial differential equations*, PhD thesis, Department of Computer Science, K.U. Leuven, B elgium, (1997)

[17] J.L. Lions: *Quelques méthodes de résolution des problèmes aux limites non linéaires*, Dunod, (1969)

[18] D.A.McDonald: *Blood Flow in Arteries*, London : Edward Arnold, (1974)

[19] F. Marquez and J.M. Lopez: *Spatial and temporal resonance in a periodically forced hydrodynamical system*, Physica D. 136, pp. 340-352, (2000)

[20] A. Meseguer, F. Marques: *On the competition between centrifugal and shear instability in spiral Poiseuille flow*, J. Fluid Mech.455, pp. 129-148, (2002)

[21] R. Mittal, S.P. Simmons, F. Najjar: *Numerical study of pulsatile flow in a constricted channel*, J. Fluid Mech., vol 485, pp 337-378, (2003)

[22] A. Pazy: *Semigroups of Linear Operators and Applications to Partial Differential Equations*, Springer-Verlag,New-York, (1983)

[23] V.V. Pao: *Numerical methods for time-periodic solutions of nonlinear parabolic boundary value problems*, SIAM J. Numer. Anal. 39, pp. 647-667, (2001)

[24] PETSC:*Portable, extensible toolkit for scientific computing*, http://www-unix.mcs.anl.gov/petsc/petsc-as/

[25] Rosenfeld: *A numerical study of pulsating flow behind a constriction*,J. Fluid Mechanics,vol. 301, pp. 203-223, (1995)

[26] W.Rudin:*Real and Complex Analysis*, Springer-Verlag,New-York, (1987)

[27] W.Rudin: *Functional Analysis* Second Edition, McGraw-Hill Inc., (1991)

[28] P.M. Gresho, R.L. Sani: *Incompressible flow and the finite element method* John Wiley and Sons, Ltd, Volume I-II, (2000)

[29] S.P.Simmons: *Numerical study of pulsatile flow in a modelled arterial stenosis* MS Thesis, Dept. Mech. Engng, University of Florida, (2001)

[30] P.H. Shankar and MD.D. Deshpande: *Fluid mechanics in the driven cavity*, Annu. Rev. Fluid Mech. 32, pp. 93-136, (2000)

[31] R. Temam: *Navier-Stokes equations*, North-Holland, Amsterdam, (1977)

[32] O. Vejvoda, L. Herrmann: *Partial differential equations:Time-periodic solutions* The Hague, Boston : M. Nijhoff ; Hingham, MA : Distributor for the U.S. and Canada, Kluwer Boston, (1982)

[33] M.J. Vogel, A.H. Hirsa and J.M. Lopez: *Spatio-temporal dynamics of a periodically driven cavity flow*, J. Fluid Mech. 478, pp. 197-226, (2003)

[34] R.Vichnevetsky,J.B. Bowles: *Fourier analysis of numerical approximations of hyperbolic equations* SIAM Studies in Applied Mathematics, (1982)

[35] A. Quarteroni, A. Valli:*Numerical Approximation of Partial Differential Equation*,Chapter 11, Springer Verlag, New-York, (1994)

[36] JR Womersley: *Method for the calculation of velocity,rate of flow and viscous drag in arteries when their pressure gradient is known*, J.Physiol., 127:553-5 63, (1955)

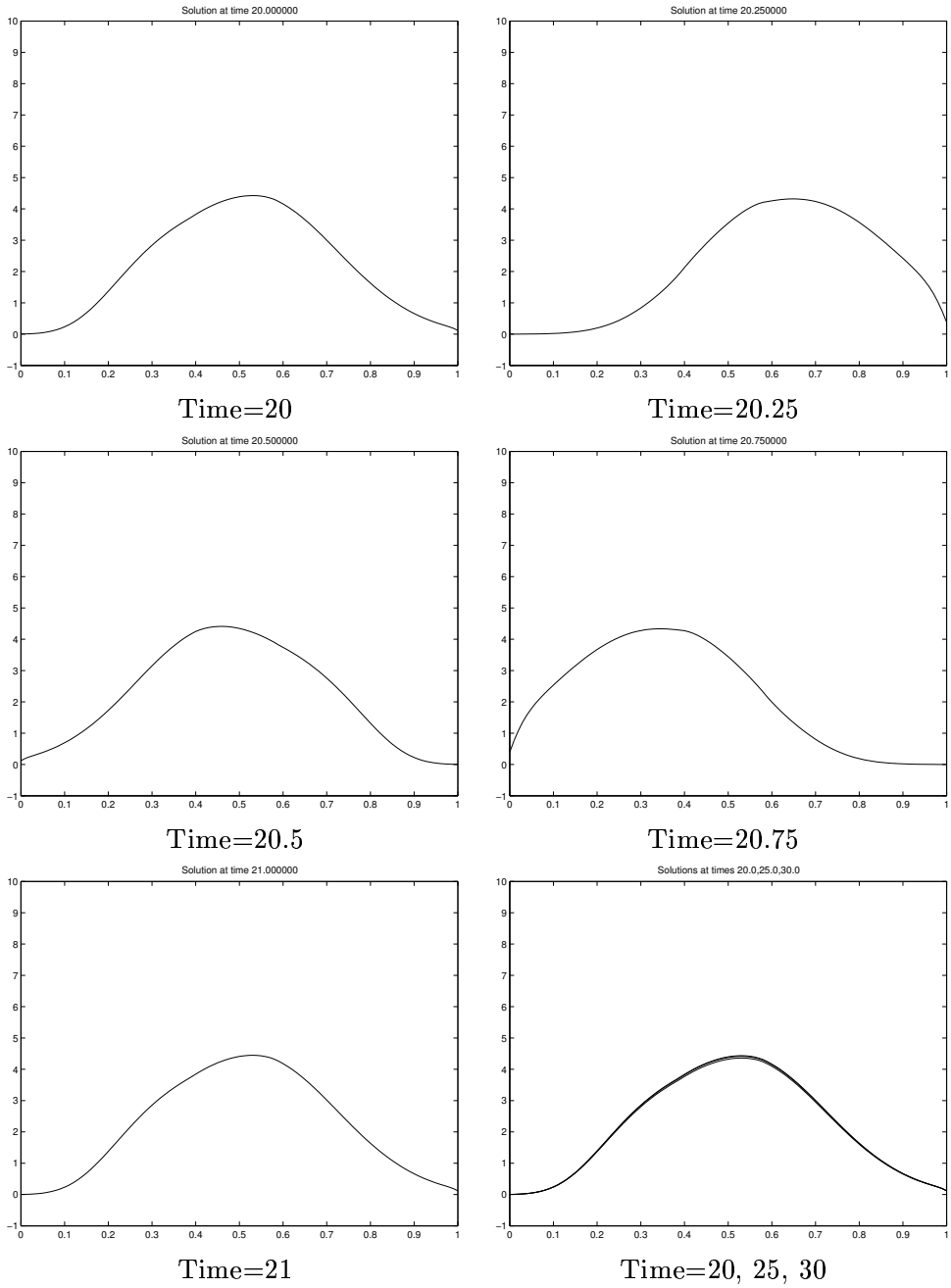

Figure 1: Solution of the advection-diffusion equation for $\nu = 0.1$

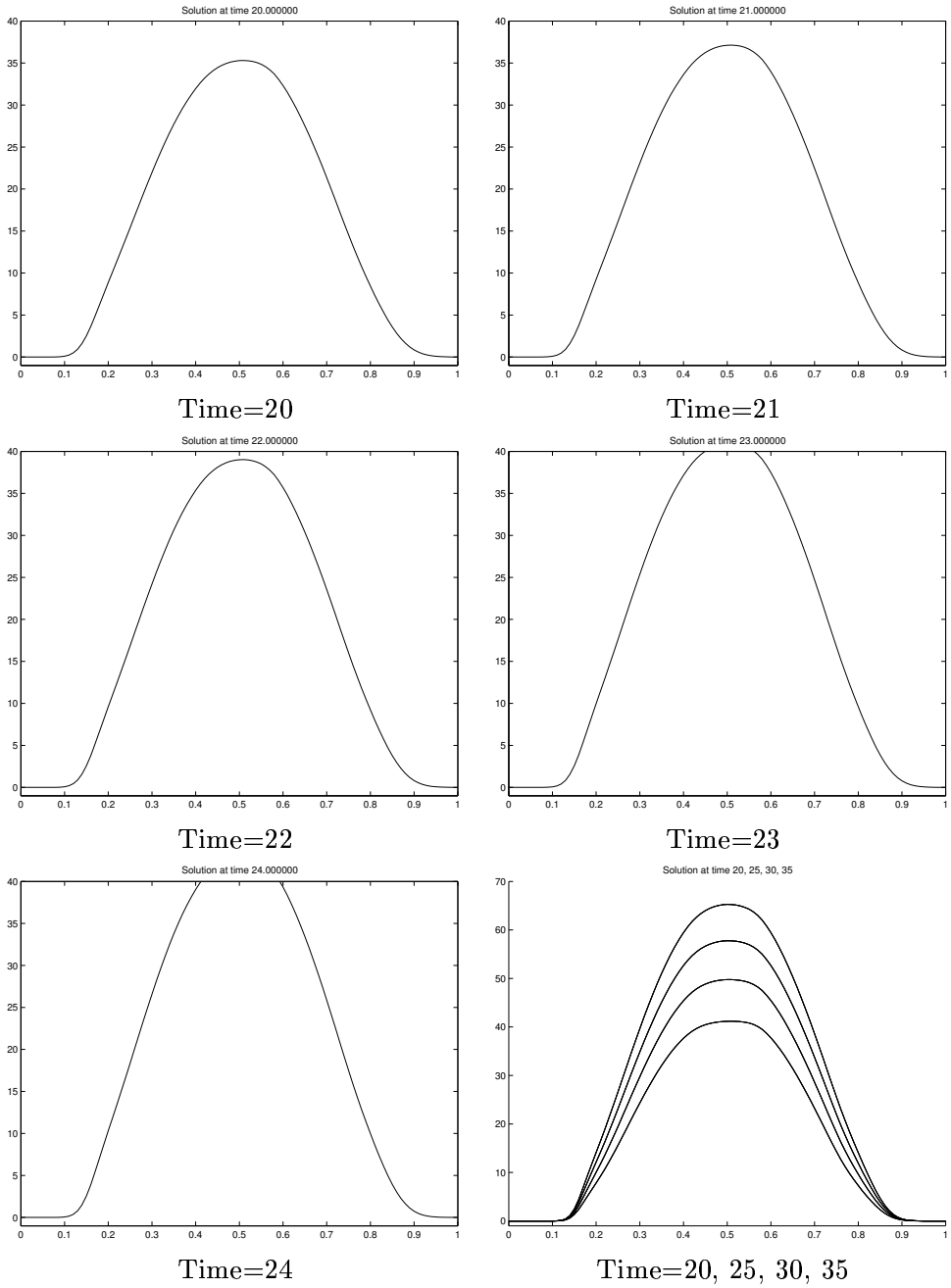

Figure 2: Solution of the advection-diffusion equation for $\nu = 0.0$

$Pe_h = 17.244$

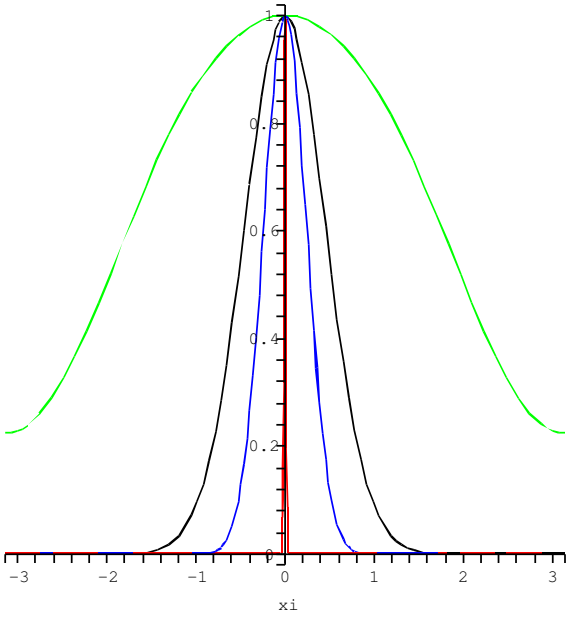

$Pe_h = 1000$

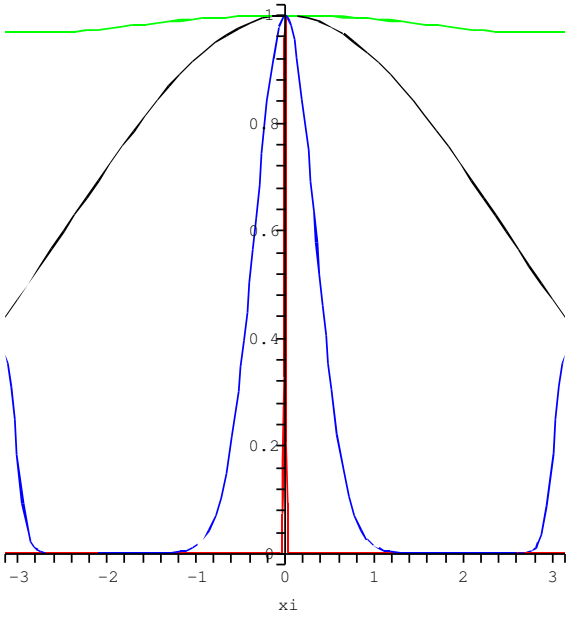

Figure 3: Amplification factor $|g(\xi h)|^N$: red-$\lambda = 6.784$, blue-$\lambda = 0.208$, black-$\lambda = 0.208$-exact, green-$\lambda = 6.26 \times 10^{-3}$

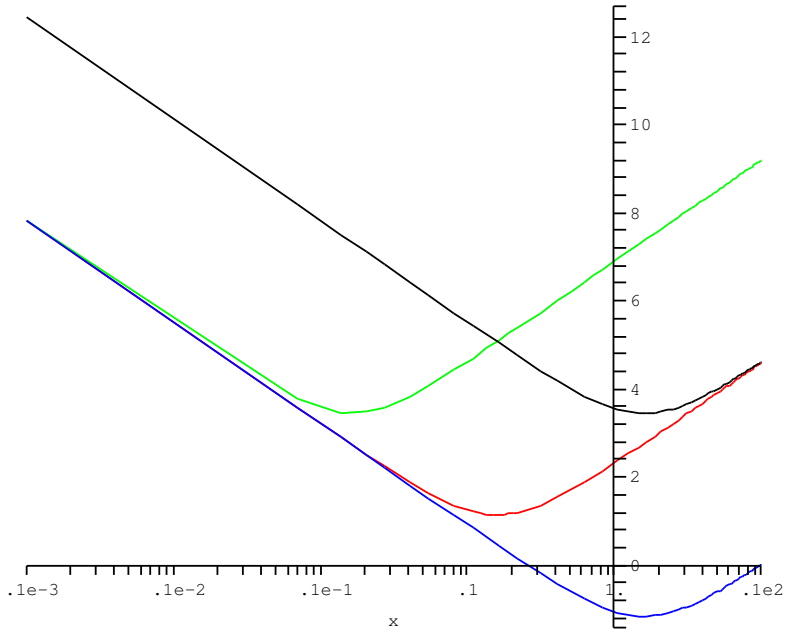

Red $L = 1$, $b = 1$, $n = 1$
Blue $L = 10$, $b = 1$, $n = 1$
Black $L = 1$, $b = 10$, $n = 1$
Green $L = 1$, $b = 1$, $n = 10$

Figure 4: The graph of $log(\delta_n)$ as a function of $log(\nu)$

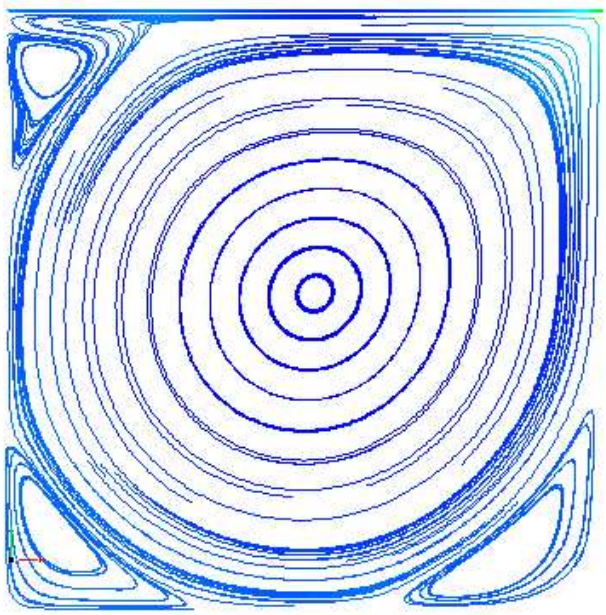

Figure 5: Streamlines colored by the $\| u \|$, $Re = 8000$, $Str = 0$, $(Wo = 0)$, $t = 480$

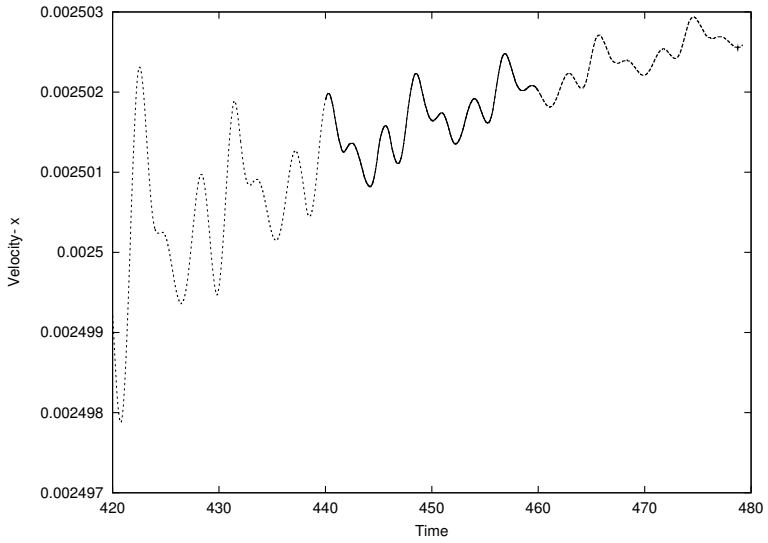

Figure 6: x-Velocity at (0.02,0.5), $Re = 8000$, $Str = 0$, $(Wo = 0)$, $t \in [420, 480]$, $U(x, 1, t) = 1$

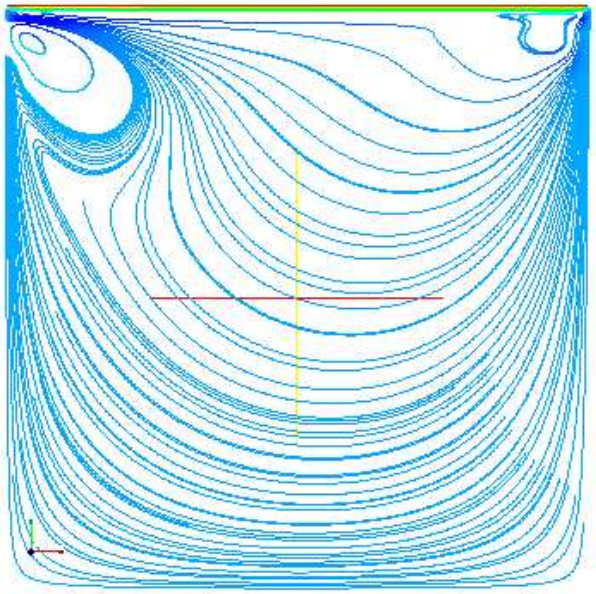

Figure 7: Streamlines colored by the $\| u \|$, $Str = 1$, $Re = 3000$, $(Wo = 68.62)$, $t = 9$, $U(x, 1, t) = \cos(\frac{2\pi t}{T})$

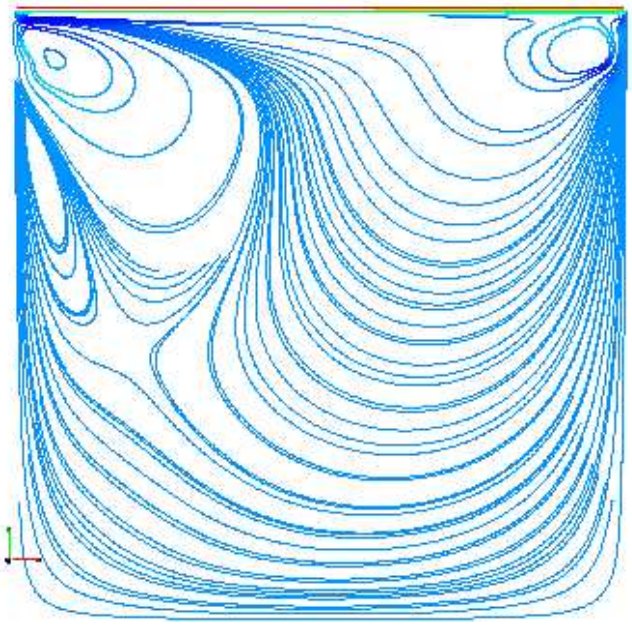

Figure 8: Streamlines colored by the $\| u \|$, $Str = 1$, $Re = 5000$, ,$(Wo = 88.6)$, $t = 9$, $U(x, 1, t) = \cos(\frac{2\pi t}{T})$

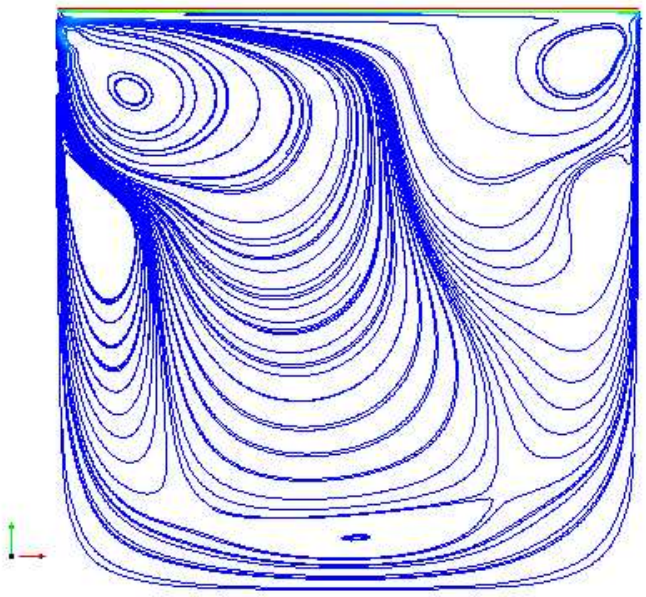

Figure 9: Streamlines colored by the $\| u \|$, Str=1, $Re = 8000$, ($Wo = 112.07$), $t = 14$, $U(x, 1, t) = \cos(\frac{2\pi t}{T})$

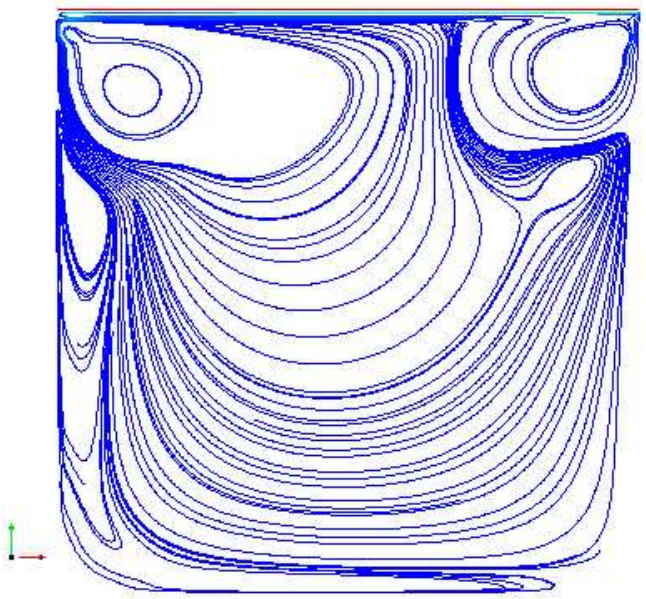

Figure 10: Streamlines colored by the $\| u \|$, Str=1, $Re = 12000$, ($Wo = 137.25$), $t = 9$, $U(x, 1, t) = \cos(\frac{2\pi t}{T})$

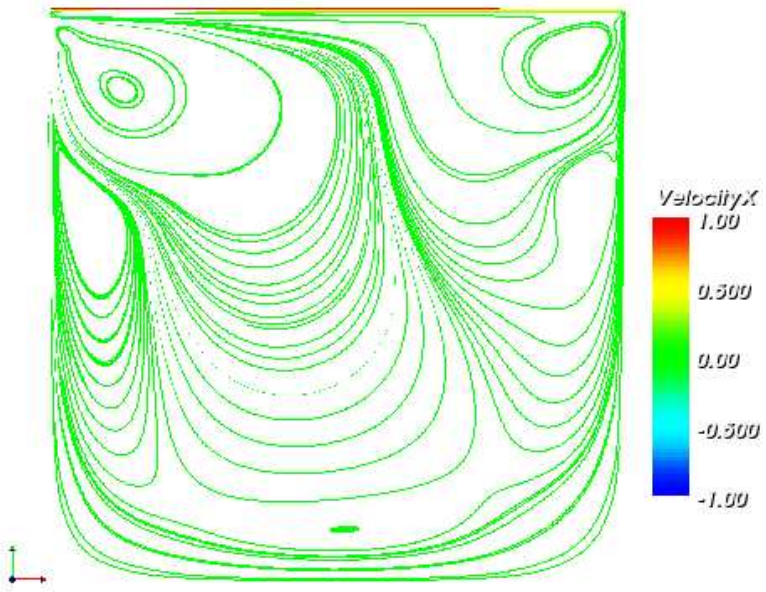

Figure 11: Streamlines colored by the x-velocity, $Str = 1$, $Re = 8000$, $(Wo = 112.07)$, $t = 14$, $U(x, 1, t) = \cos(\frac{2\pi t}{T})$

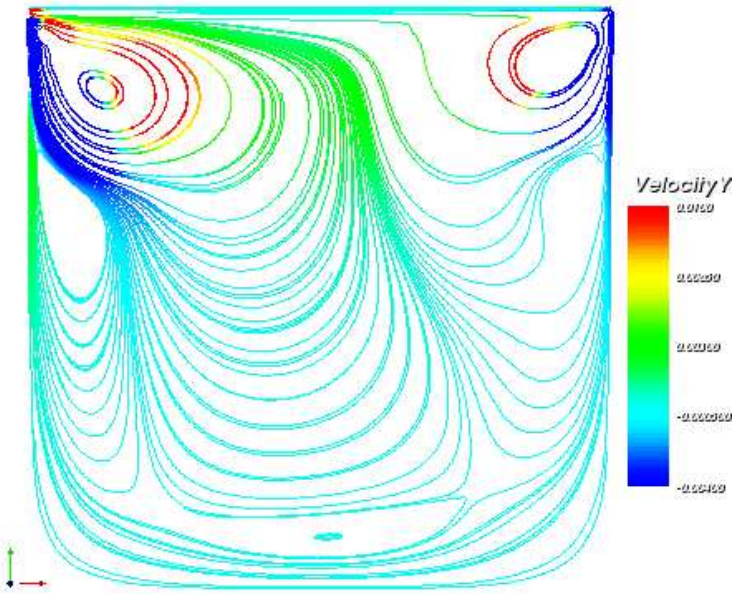

Figure 12: Streamlines colored by the y-velocity, $Str = 1$, $Re = 8000$, $(Wo = 112.07)$, $t = 14$, $U(x, 1, t) = \cos(\frac{2\pi t}{T})$

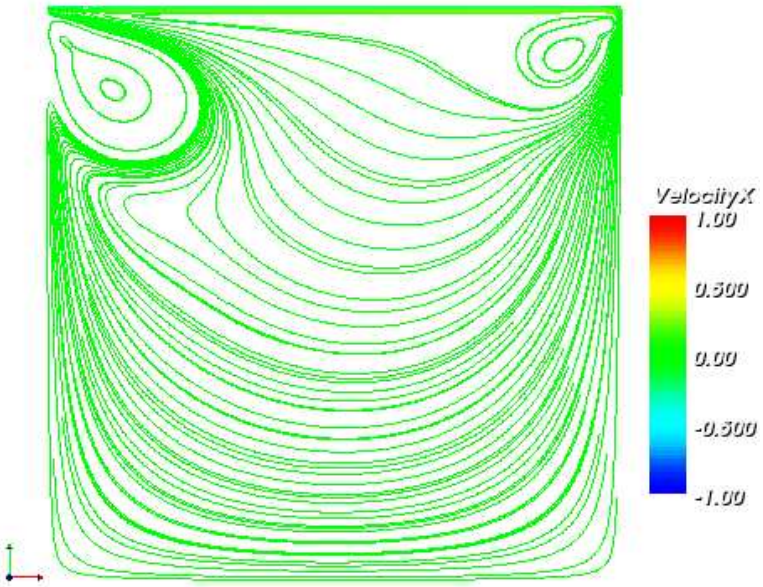

Figure 13: Streamlines colored by the x-velocity, $Str = 1$, $Re = 8000$, $(Wo = 112.07)$, $t = 14 + \frac{T}{4}$, $U(x, 1, t) = \cos(\frac{2\pi t}{T})$

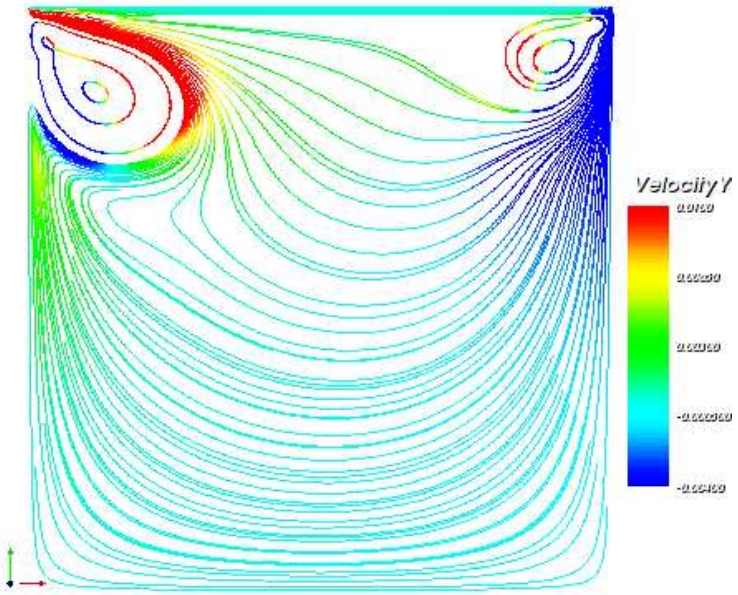

Figure 14: Streamlines colored by the y-velocity, $Str = 1$, $Re = 8000$, $(Wo = 112.07)$, $t = 14 + \frac{T}{4}$, $U(x, 1, t) = \cos(\frac{2\pi t}{T})$

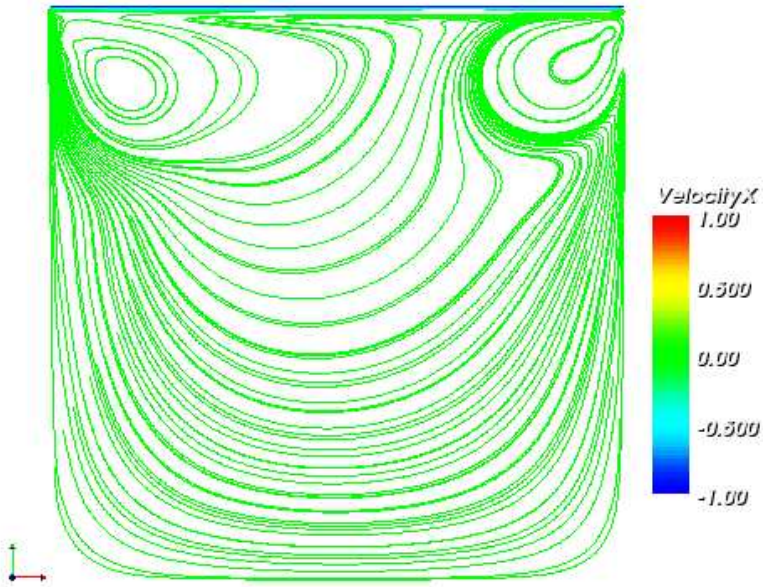

Figure 15: Streamlines colored by the x-velocity, $Str = 1$, $Re = 8000$, $(Wo = 112.07)$, $t = 14 + \frac{T}{2}$, $U(x, 1, t) = \cos(\frac{2\pi t}{T})$

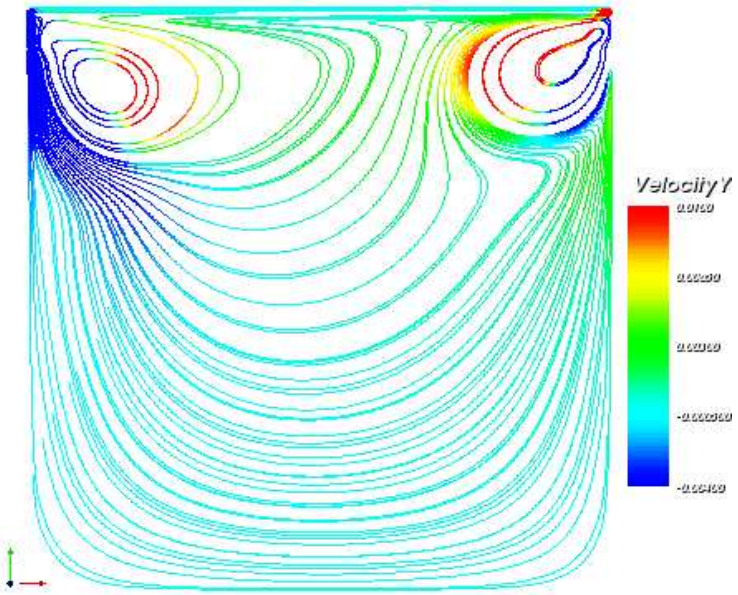

Figure 16: Streamlines colored by the y-velocity, $Str = 1$, $Re = 8000$, $(Wo = 112.7)$, $t = 14 + \frac{T}{2}$, $U(x, 1, t) = \cos(\frac{2\pi t}{T})$

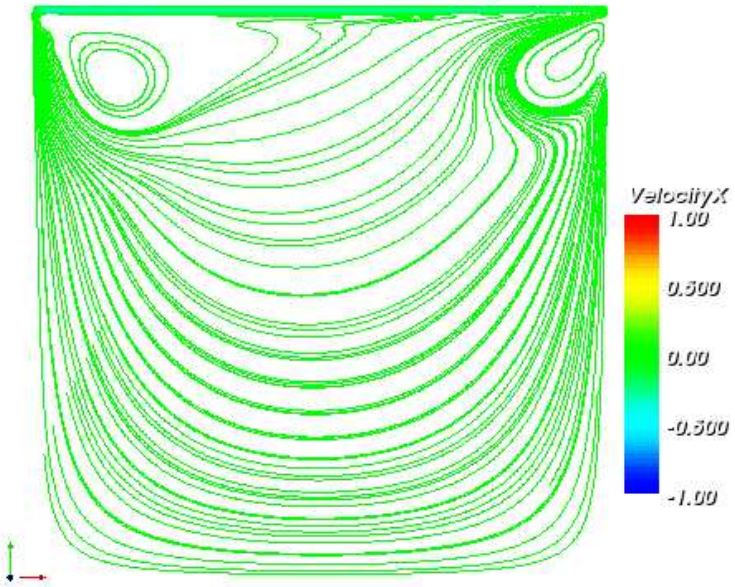

Figure 17: Streamlines colored by the x-velocity, $Str = 1$, $Re = 8000$, $(Wo = 112.07)$, $t = 14 + \frac{3T}{4}$, $U(x, 1, t) = \cos(\frac{2\pi t}{T})$

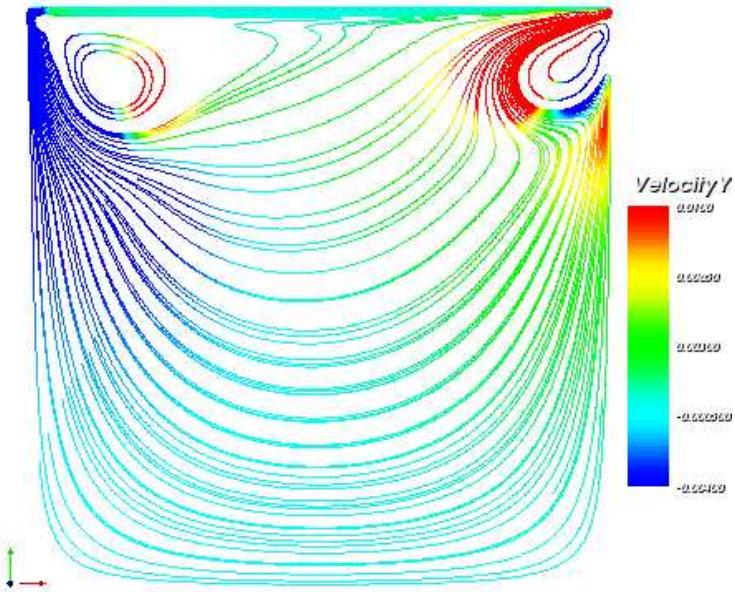

Figure 18: Streamlines colored by the y-velocity, $Str = 1$, $Re = 8000$, $(Wo = 112.07)$, $t = 14 + \frac{3T}{4}$, $U(x, 1, t) = \cos(\frac{2\pi t}{T})$

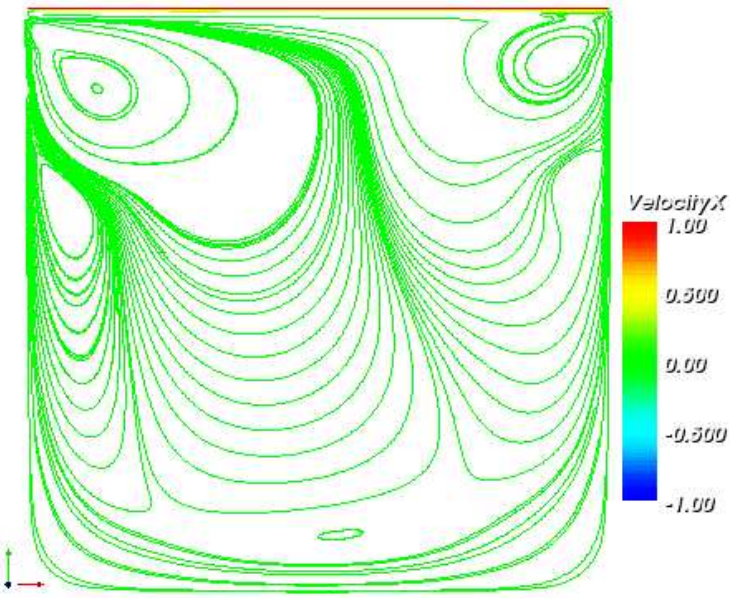

Figure 19: Streamlines colored by the x-velocity, $Str = 1$, $Re = 8000$, $(Wo = 112.07)$, $t = 15$, $U(x, 1, t) = \cos(\frac{2\pi t}{T})$

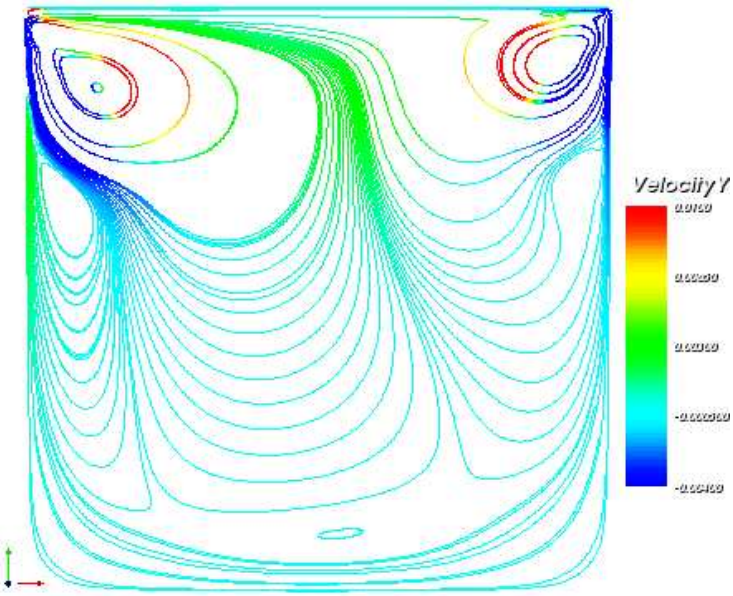

Figure 20: Streamlines colored by the y-velocity, $Str = 1$, $Re = 8000$, $(Wo = 112.07)$, $t = 15$, $U(x, 1, t) = \cos(\frac{2\pi t}{T})$

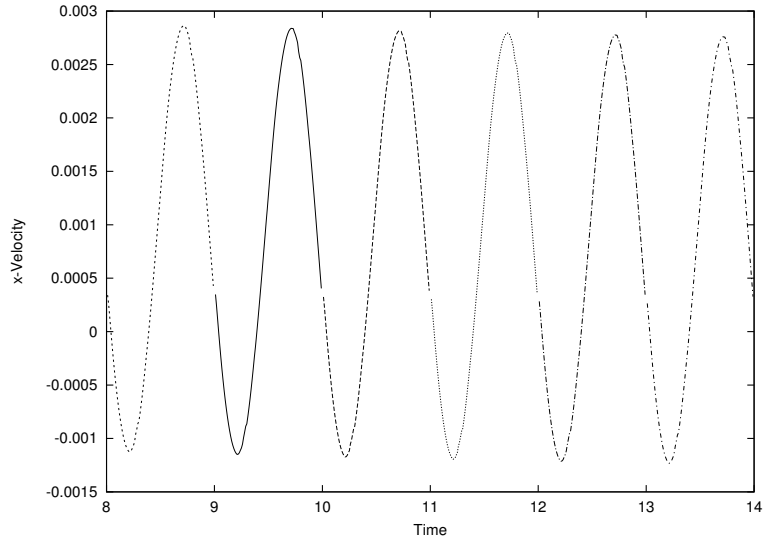

Figure 21: x-Velocity at (0.2,0.75), $Str = 1$, $Re = 8000$, $(Wo = 112.07)$, $t \in [8, 14]$, $U(x, 1, t) = \cos(\frac{2\pi t}{T})$

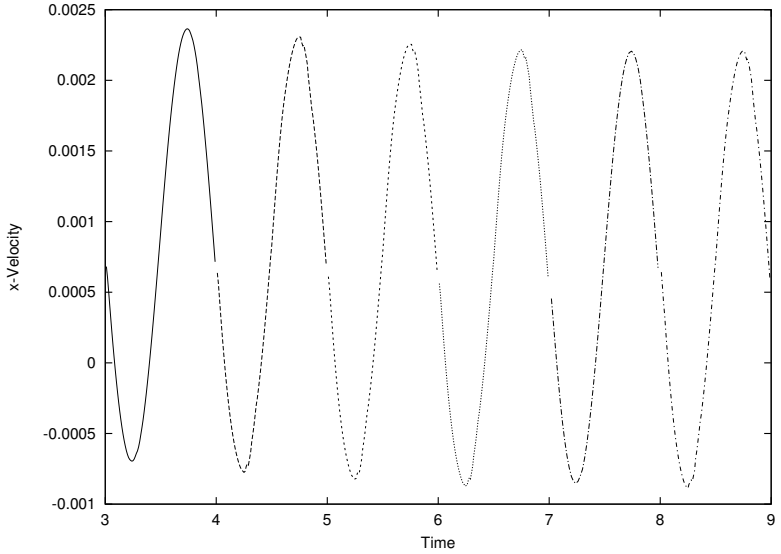

Figure 22: x-Velocity at (0.2,0.75), $Str = 1$, $Re = 12000$, $(Wo = 137.25)$, $t \in [3, 9]$, $U(x, 1, t) = \cos(\frac{2\pi t}{T})$

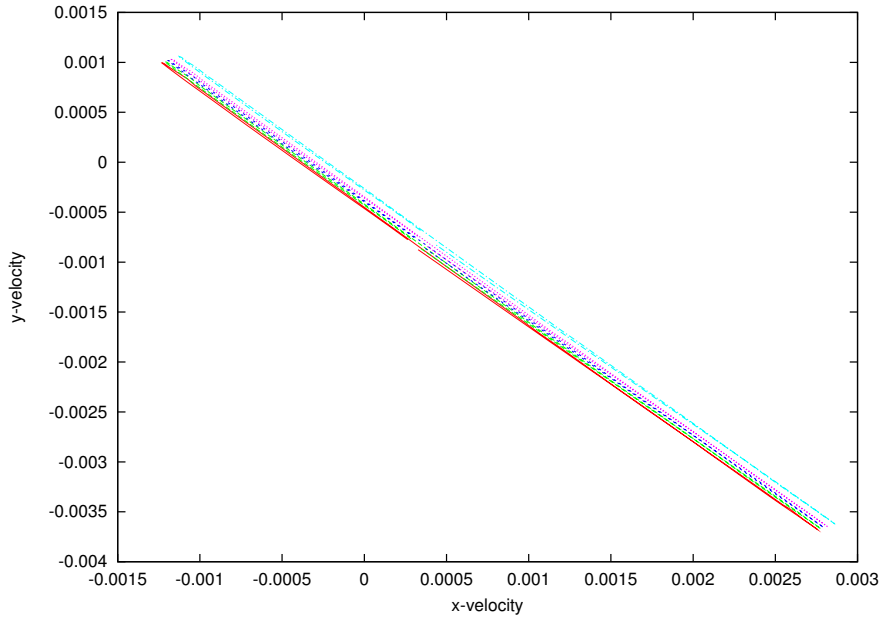

Figure 23: y-Velocity wrt x-Velocity at (0.2,0.75), $Str = 1$, $Re = 8000$, ($Wo = 112.07$), $t \in [11, 14]$, $U(x, 1, t) = \cos(\frac{2\pi t}{T})$

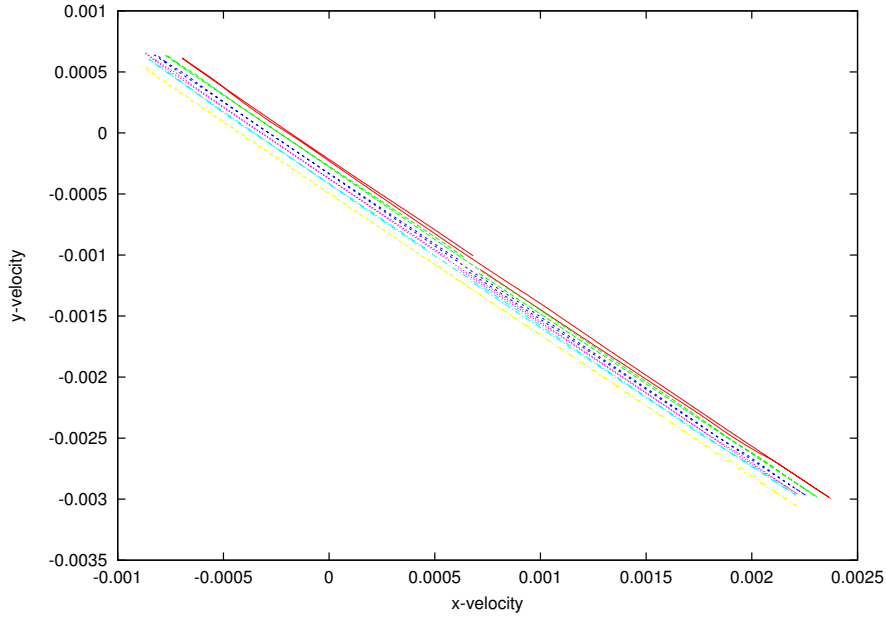

Figure 24: y-Velocity wrt x-Velocity at (0.2,0.75), $Str = 1$, $Re = 12000$, ($Wo = 137.25$), $t \in [6, 9]$, $U(x, 1, t) = \cos(\frac{2\pi t}{T})$

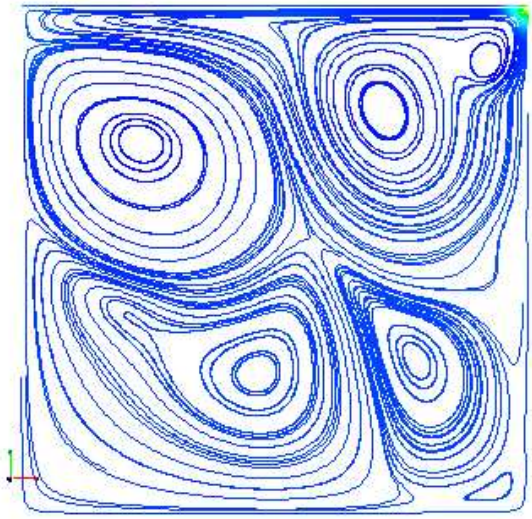

Figure 25: Streamlines colored by the $\| u \|$, $Str = 0.1$, $Re = 5000$, $(Wo = 28.01)$, $t = 110$, $U(x, 1, t) = \cos(\frac{2\pi t}{T})$

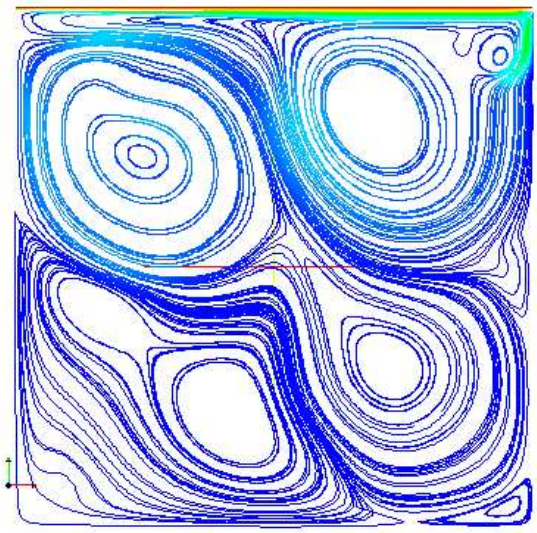

Figure 26: Streamlines colored by the $\| u \|$, $Str = 0.1$, $Re = 8000$, $(Wo = 35.44)$, $t = 190$, $U(x, 1, t) = \cos(\frac{2\pi t}{T})$

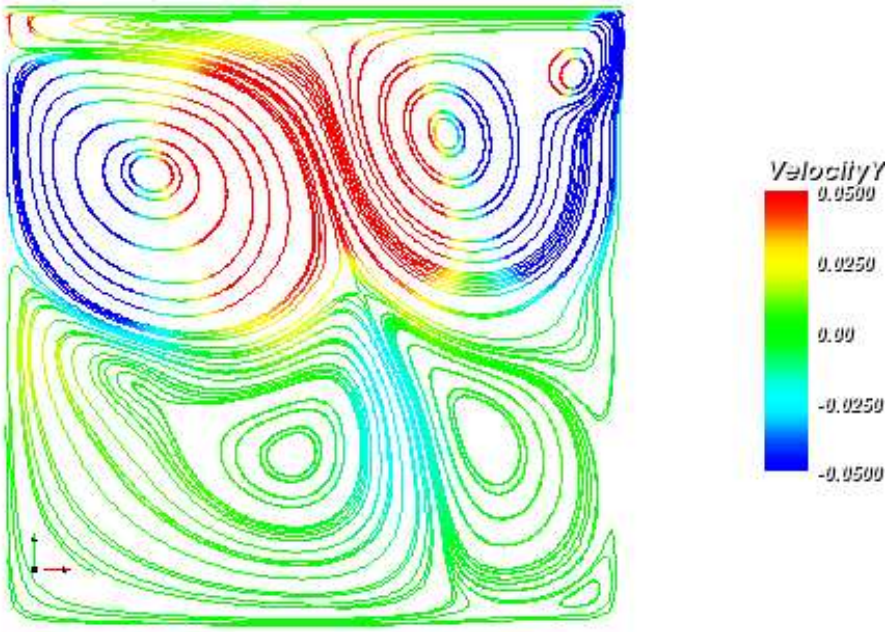

Figure 27: Streamlines colored by the y-velocity, $Str = 0.1$, $Re = 5000$, $(Wo = 28.01)$, $t = 110$, $U(x, 1, t) = \cos(\frac{2\pi t}{T})$

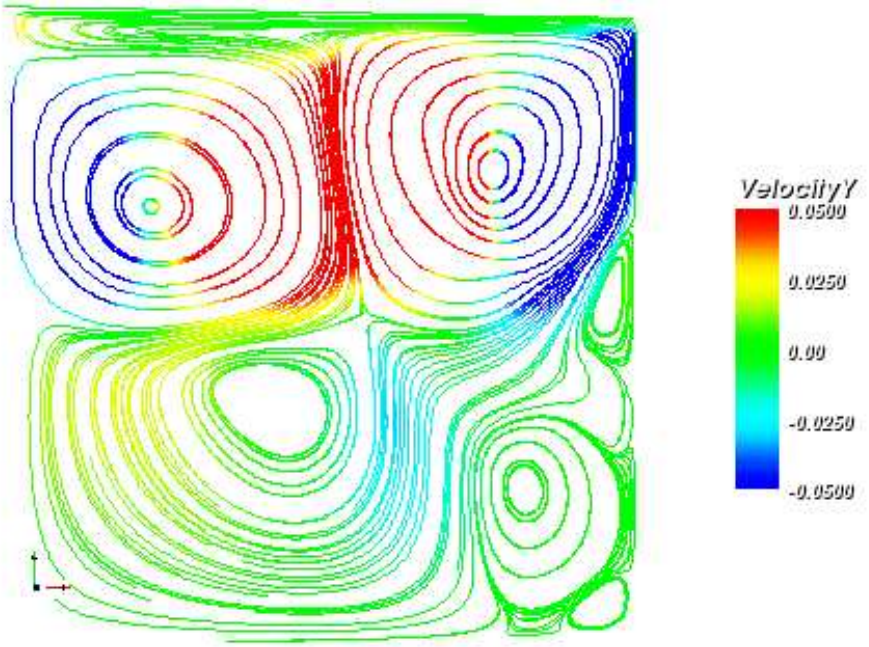

Figure 28: Streamlines colored by the y-velocity, $Str = 0.1$, $Re = 5000$, $(Wo = 28.01)$, $t = 110 + \frac{T}{4}$, $U(x, 1, t) = \cos(\frac{2\pi t}{T})$

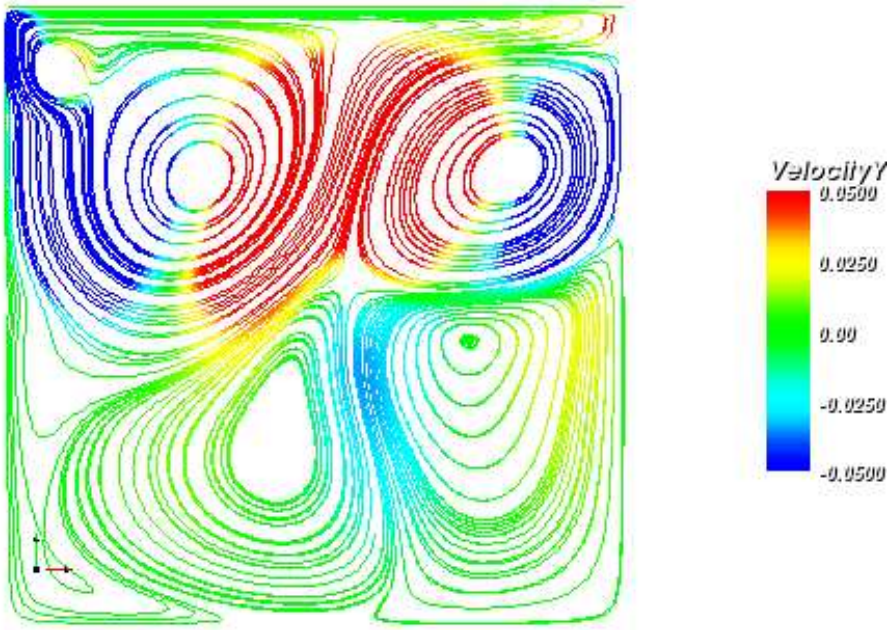

Figure 29: Streamlines colored by the y-velocity, $Str = 0.1$, $Re = 5000$, $(Wo = 28.01)$, $t = 110 + \frac{T}{2}$, $U(x, 1, t) = \cos(\frac{2\pi t}{T})$

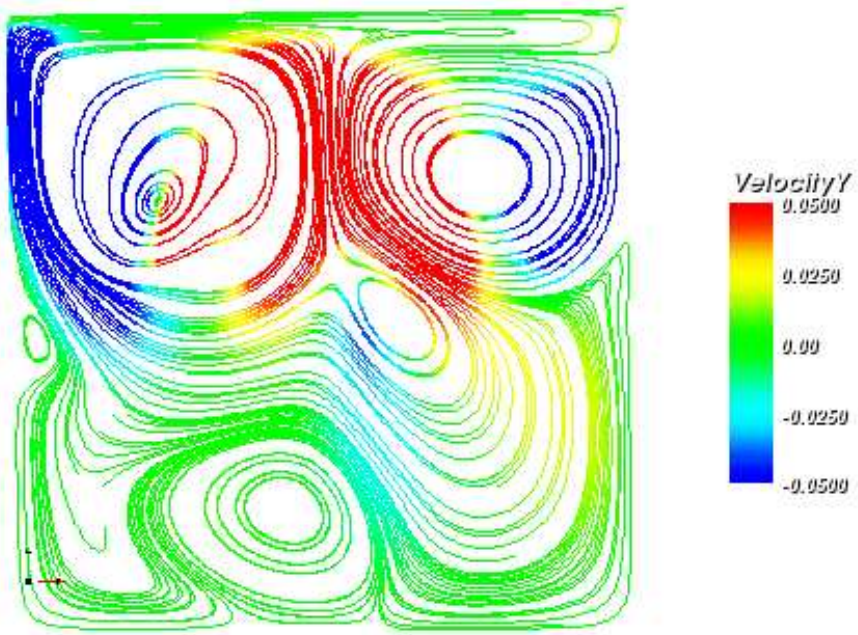

Figure 30: Streamlines colored by the y-velocity, $Str = 0.1$, $Re = 5000$, $(Wo = 28.01)$, $t = 110 + \frac{3T}{4}$, $U(x, 1, t) = \cos(\frac{2\pi t}{T})$

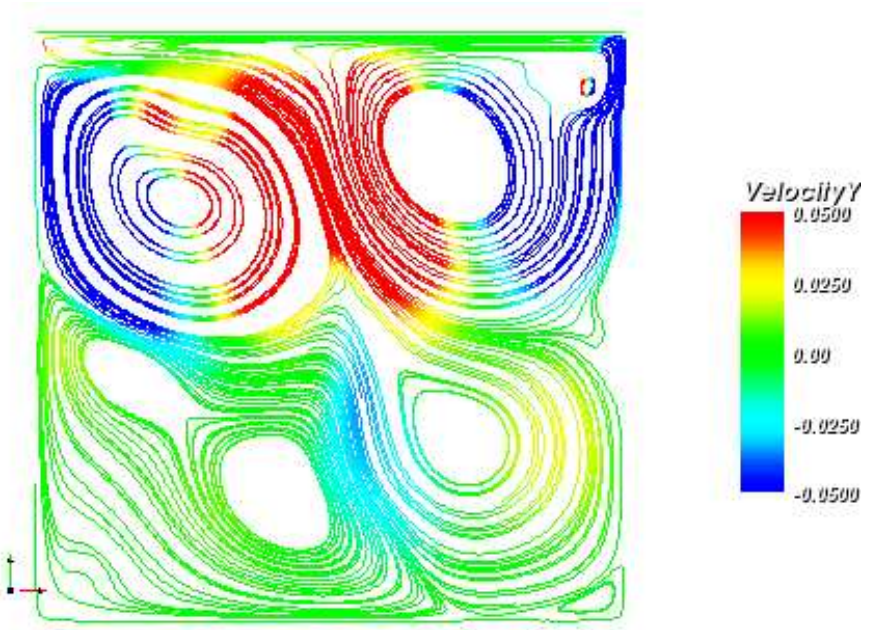

Figure 31: Streamlines colored by the y-velocity, $Str = 0.1$, $Re = 8000$, $(Wo = 35.44)$, $t = 190$, $U(x, 1, t) = \cos(\frac{2\pi t}{T})$

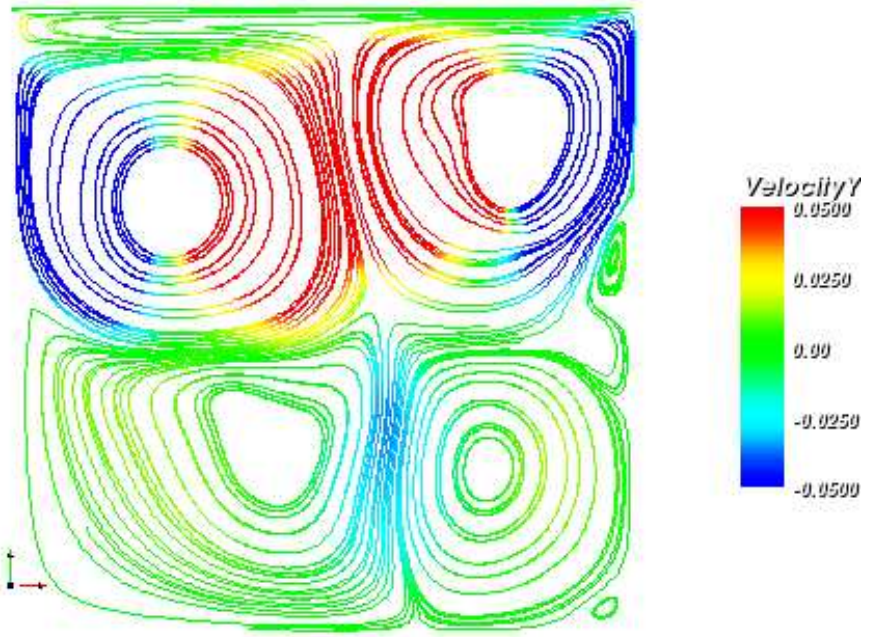

Figure 32: Streamlines colored by the y-velocity, $Str = 0.1$, $Re = 8000$, $(Wo = 35.44)$, $t = 190 + \frac{T}{4}$, $U(x, 1, t) = \cos(\frac{2\pi t}{T})$

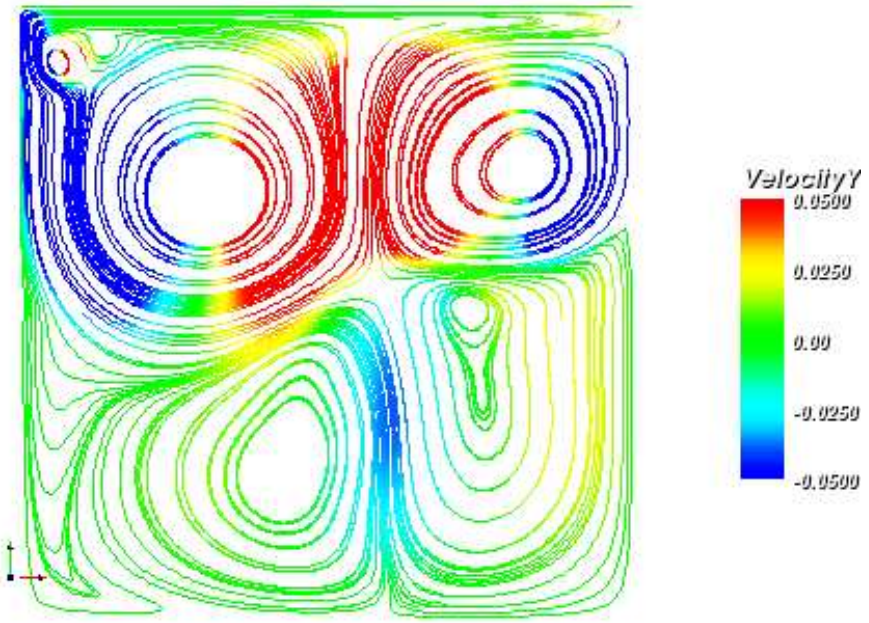

Figure 33: Streamlines colored by the y-velocity, $Str = 0.1$, $Re = 8000$, $(Wo = 35.44)$, $t = 190 + \frac{T}{2}$, $U(x, 1, t) = \cos(\frac{2\pi t}{T})$

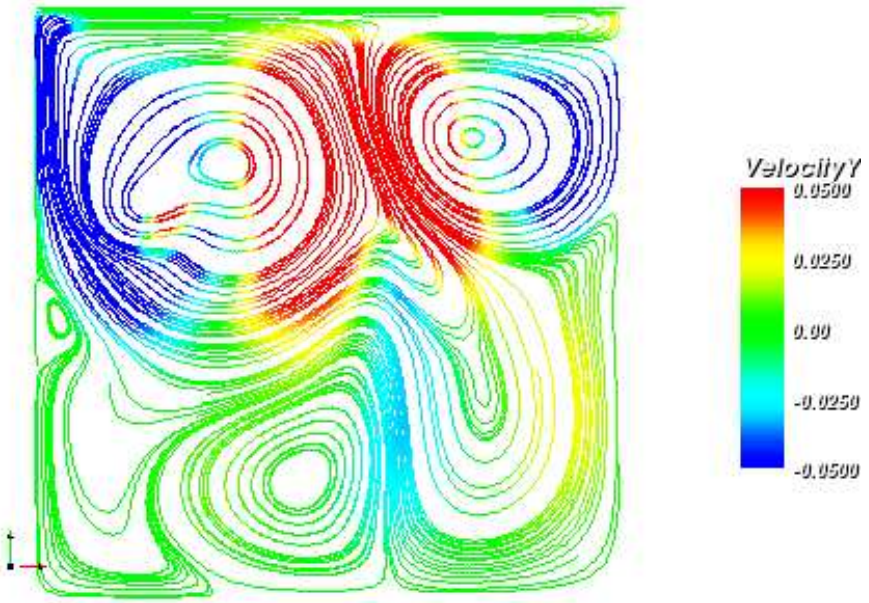

Figure 34: Streamlines colored by the y-velocity, $Str = 0.1$, $Re = 8000$, $(Wo = 35.44)$, $t = 190 + \frac{3T}{4}$, $U(x, 1, t) = \cos(\frac{2\pi t}{T})$

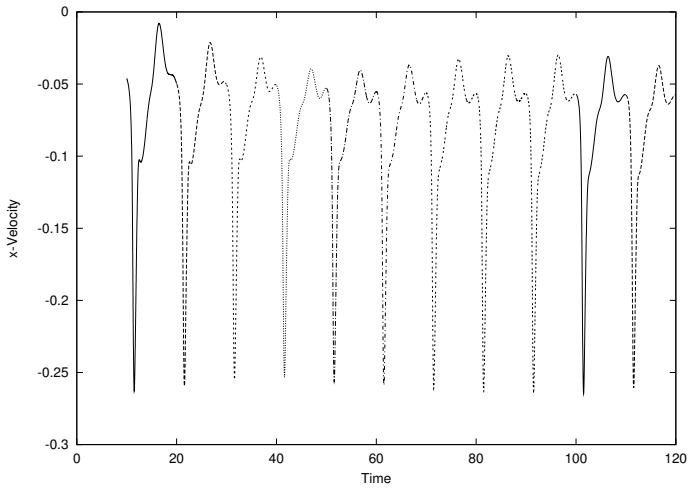

Figure 35: x-Velocity at $(0.8, 0.5)$, $Str = 0.1$, $Re = 5000$, $(Wo = 28.01)$, $t \in [10, 120]$, $U(x, 1, t) = \cos(\frac{2\pi t}{T})$

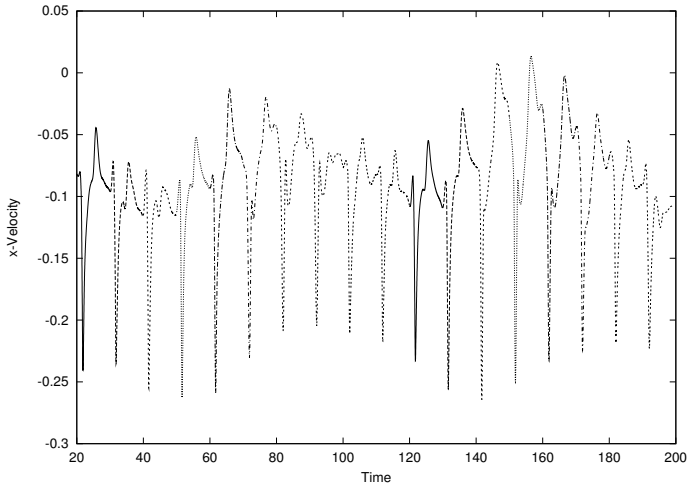

Figure 36: x-Velocity at $(0.8, 0.5)$, $Str = 0.1$, $Re = 8000$, $(Wo = 35.44)$, $t \in [20, 200]$, $U(x, 1, t) = \cos(\frac{2\pi t}{T})$

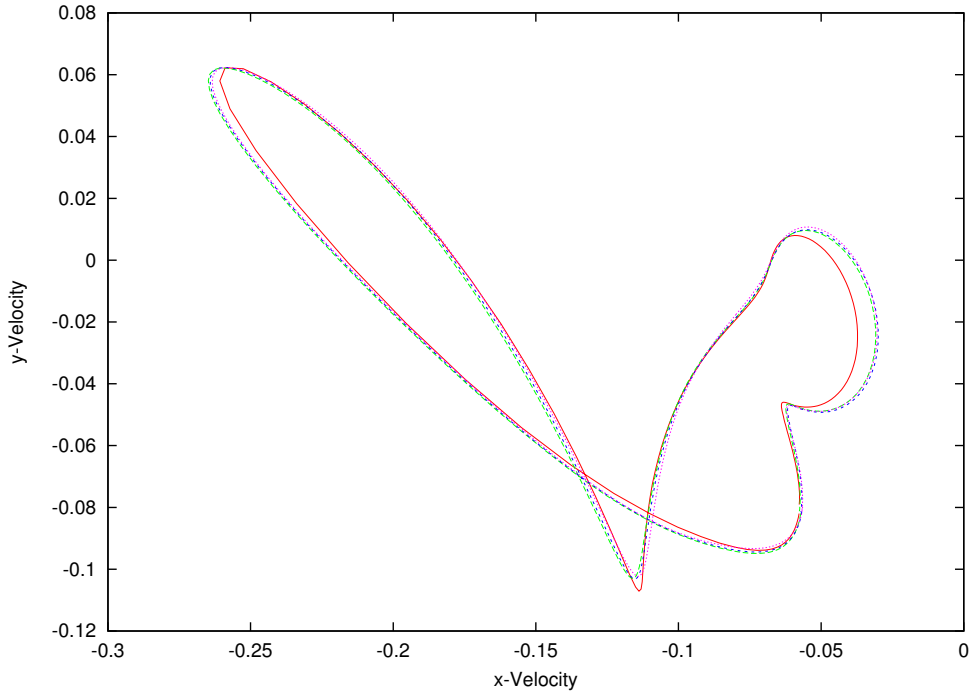

Figure 37: y-Velocity wrt x-Velocity at $(0.8, 0.5)$, $Str = 0.1$, $Re = 5000$, $(Wo = 28.01)$, $t \in [90, 120]$, $U(x, 1, t) = \cos(\frac{2\pi t}{T})$

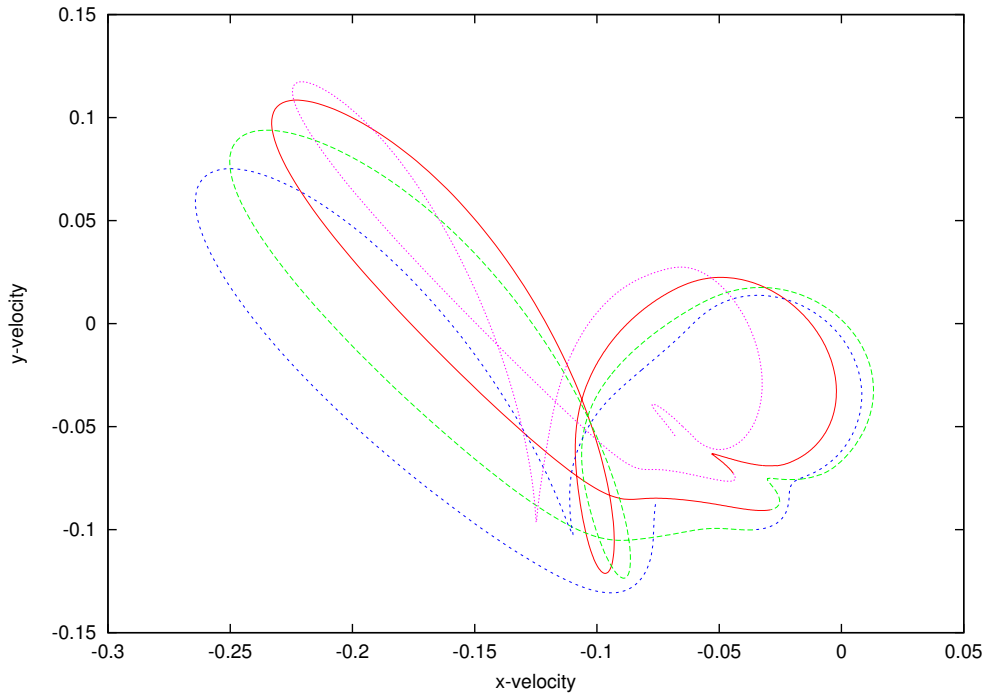

Figure 38: y-Velocity wrt x-Velocity at $(0.8, 0.5)$, $Str = 0.1$, $Re = 8000$, $(Wo = 35.44)$, $t \in [160, 200]$, $U(x, 1, t) = \cos(\frac{2\pi t}{T})$

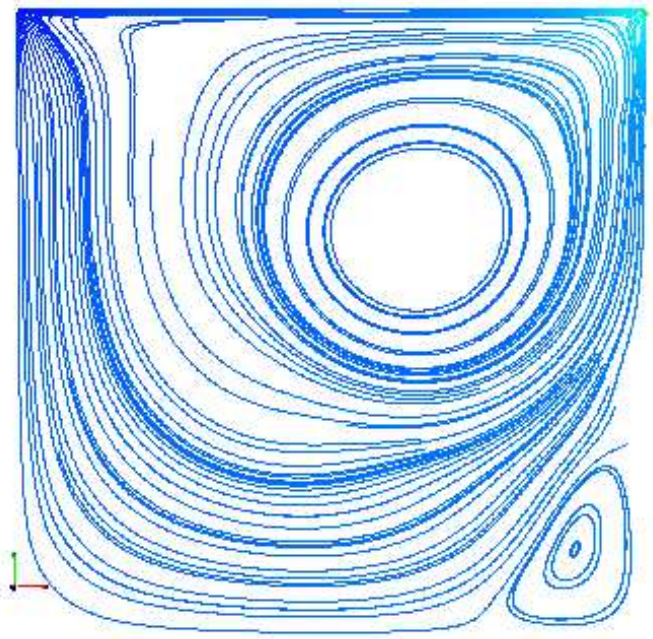

Figure 39: Streamlines colored by the $\| u \|$, $Str = 1$, $Re = 5000$, $(Wo = 88.6)$, $t = 6$, $U(x, 1, t) = (max(\cos(\frac{2\pi t}{T}), 0), 0)$

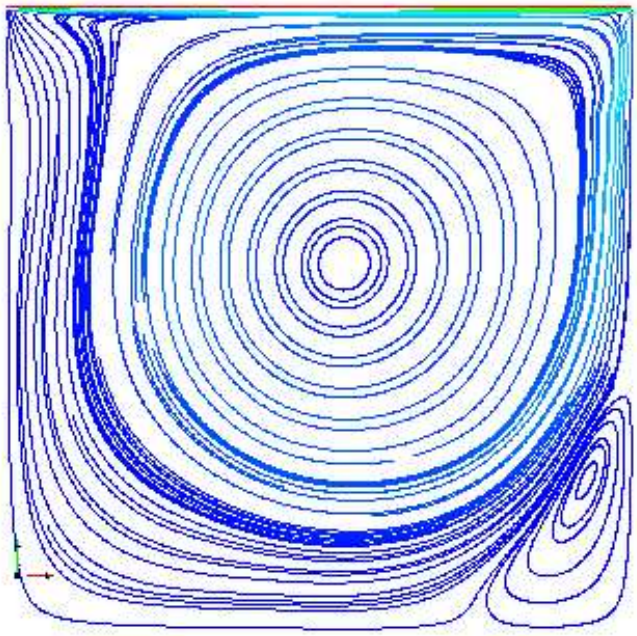

Figure 40: Streamlines colored by the $\| u \|$, $Str = 1$, $Re = 8000$, $(Wo = 112.07)$, $t = 30$, $U(x, 1, t) = (max(\cos(\frac{2\pi t}{T}), 0), 0)$

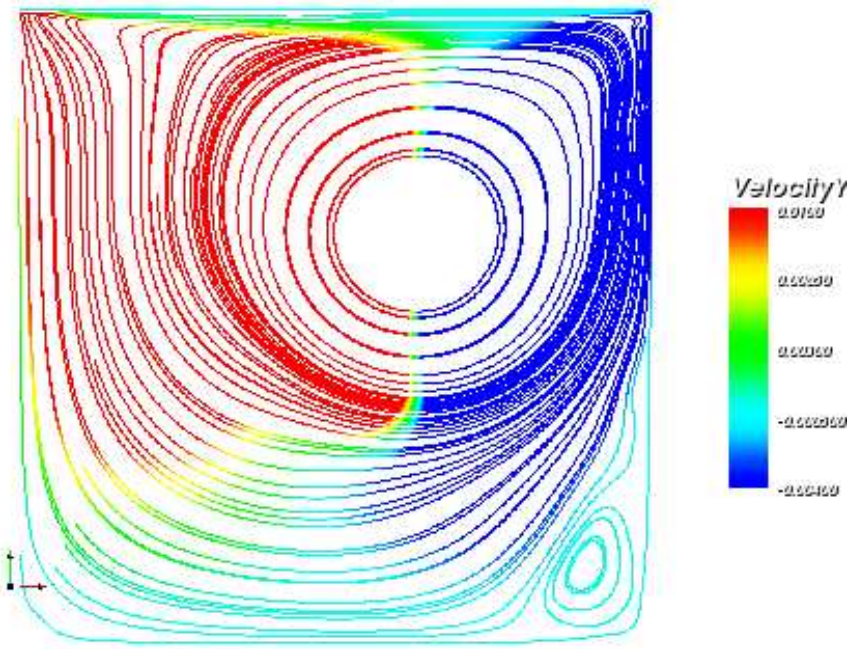

Figure 41: Streamlines colored by the y-velocity, $Str = 1$, $Re = 5000$, $(Wo = 88.6)$, $t = 6$, $U(x, 1, t) = (max(\cos(\frac{2\pi t}{T}), 0), 0)$

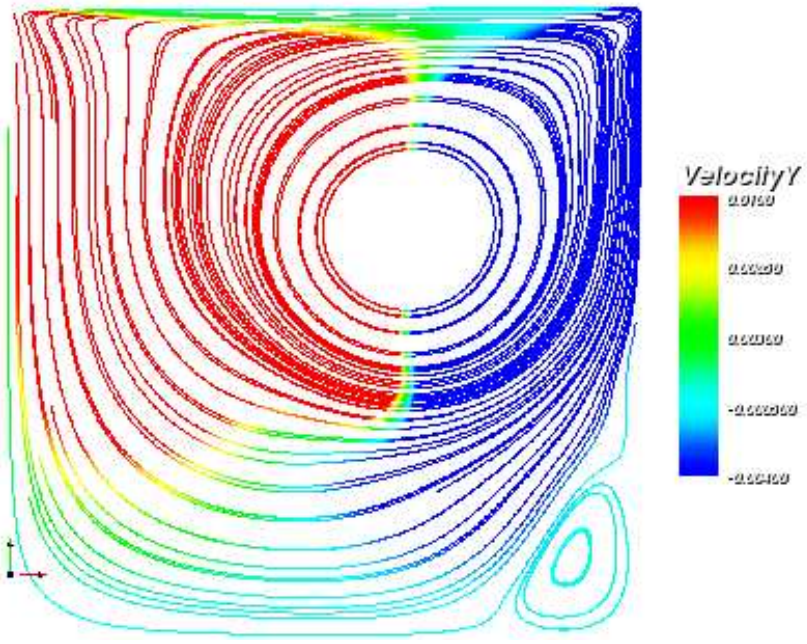

Figure 42: Streamlines colored by the y-velocity, $Str = 1$, $Re = 5000$, $(Wo = 88.6)$, $t = 6 + \frac{T}{4}$, $U(x, 1, t) = (max(\cos(\frac{2\pi t}{T}), 0), 0)$

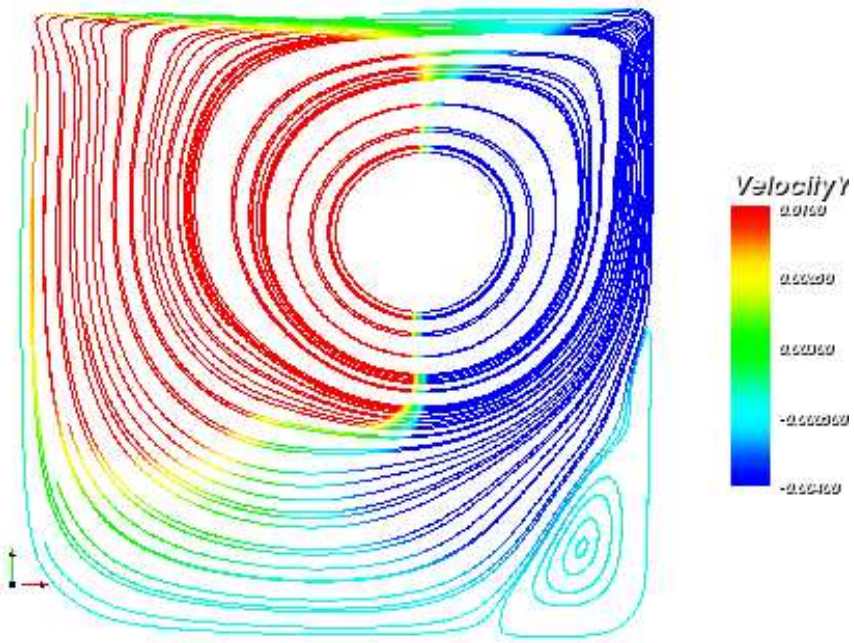

Figure 43: Streamlines colored by the y-velocity, $Str = 1$, $Re = 5000$, $(Wo = 88.6)$, $t = 6 + \frac{T}{2}$, $U(x, 1, t) = (max(\cos(\frac{2\pi t}{T}), 0), 0)$

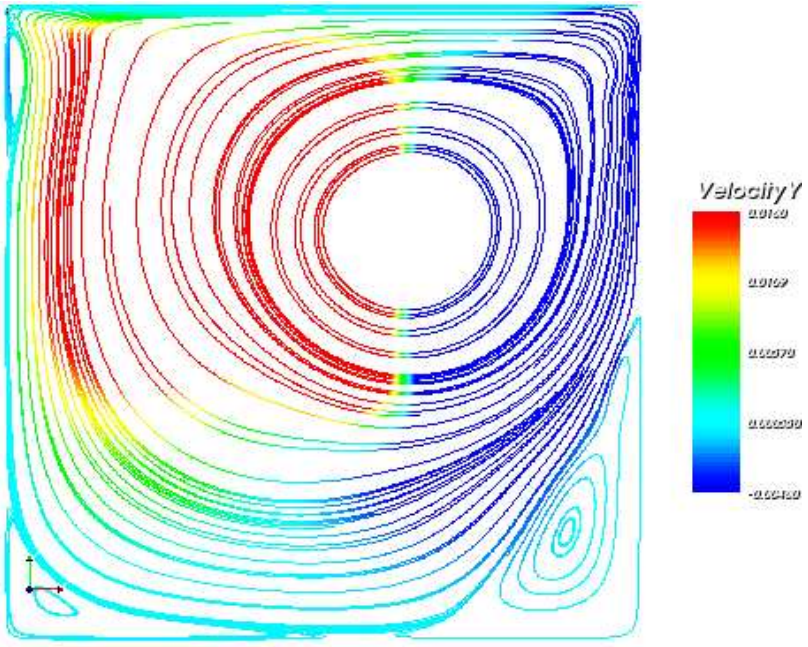

Figure 44: Streamlines colored by the y-velocity, $Str = 1$, $Re = 5000$, $(Wo = 88.6)$, $t = 6 + \frac{3T}{4}$, $U(x, 1, t) = (max(\cos(\frac{2\pi t}{T}), 0), 0)$

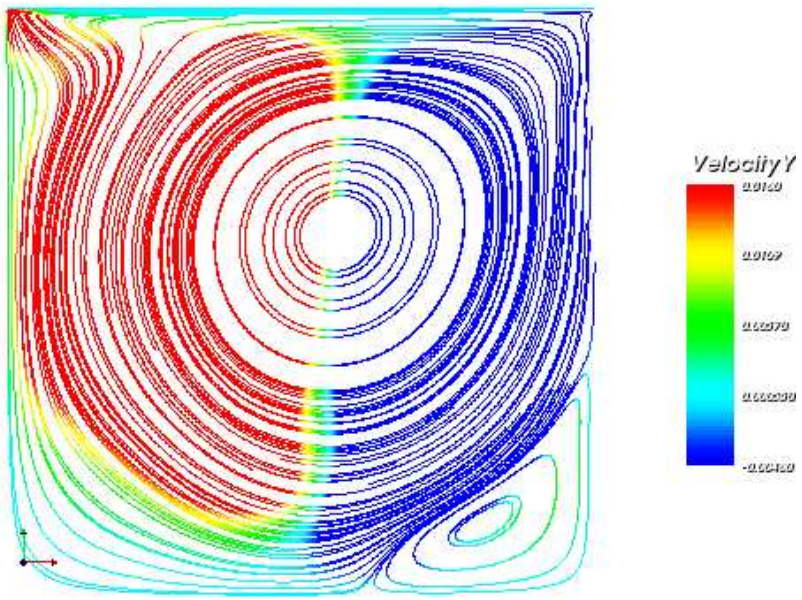

Figure 45: Streamlines colored by the y-velocity, $Str = 1$, $Re = 8000$, $Wo = (112.07)$, $t = 30$, $U(x, 1, t) = (max(\cos(\frac{2\pi t}{T}), 0), 0)$

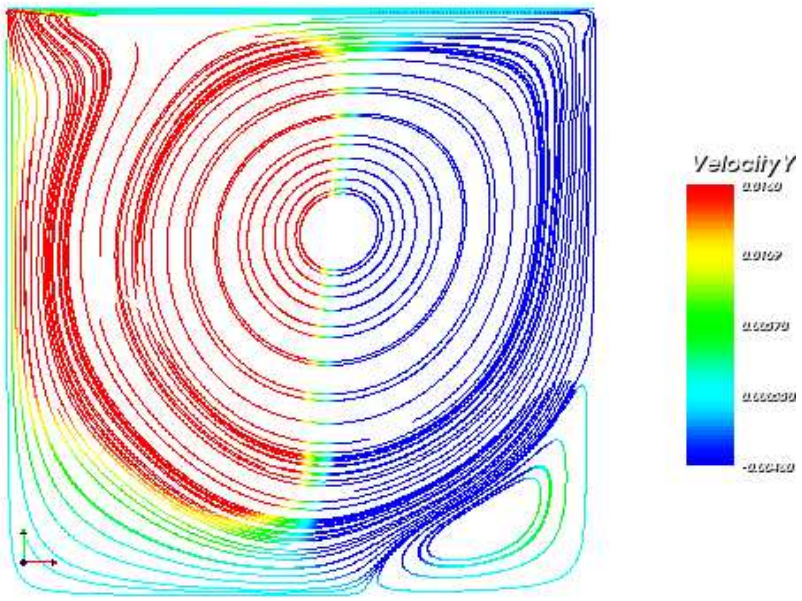

Figure 46: Streamlines colored by the y-velocity, $Str = 1$, $Re = 8000$, $Wo = (112.07)$, $t = 30 + \frac{T}{4}$, $U(x, 1, t) = (max(\cos(\frac{2\pi t}{T}), 0), 0)$

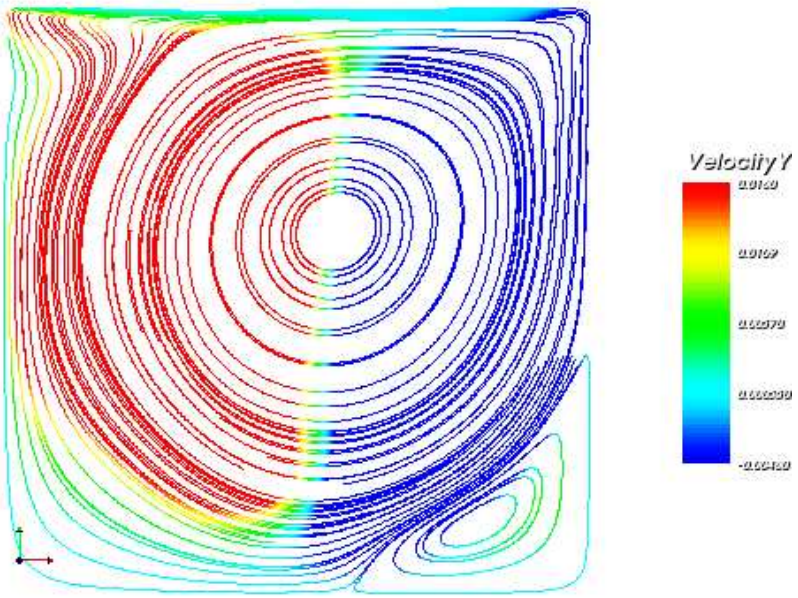

Figure 47: Streamlines colored by the y-velocity, $Str = 1$, $Re = 8000$, $Wo = (112.07)$, $t = 30 + \frac{T}{2}$, $U(x, 1, t) = (max(\cos(\frac{2\pi t}{T}), 0), 0)$

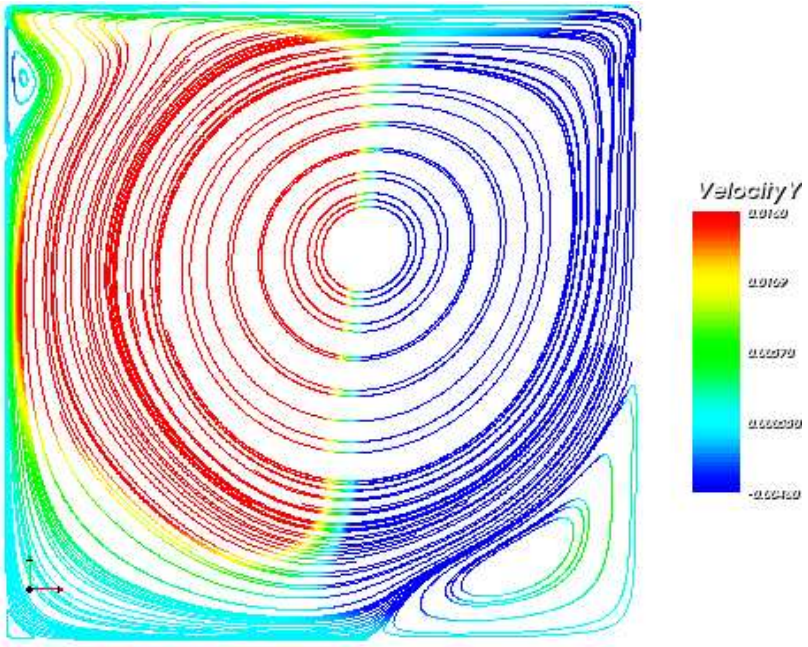

Figure 48: Streamlines colored by the y-velocity, $Str = 1$, $Re = 8000$, $Wo = (112.07)$, $t = 30 + \frac{3T}{4}$, $U(x, 1, t) = (max(\cos(\frac{2\pi t}{T}), 0), 0)$

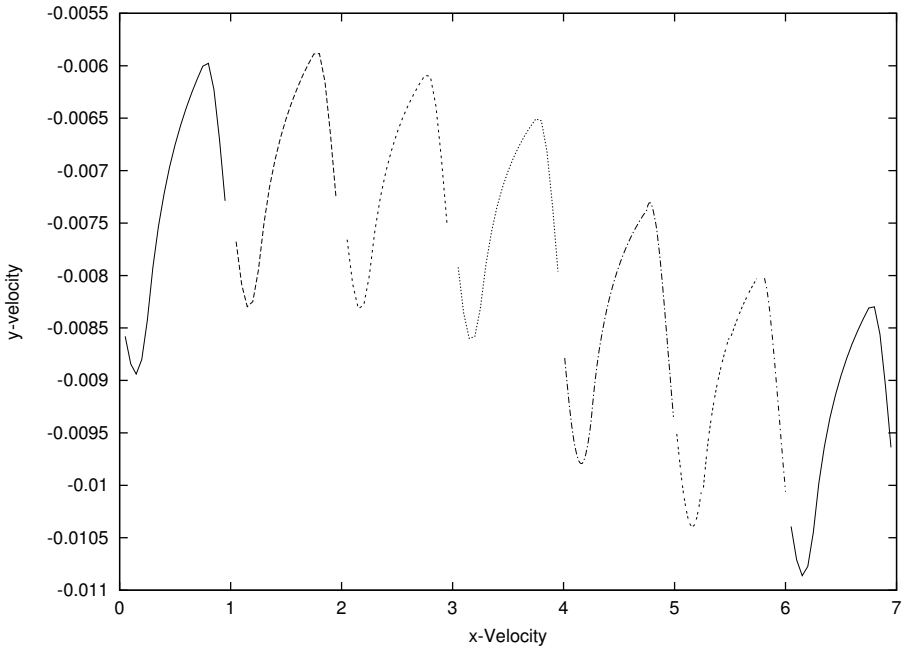

Figure 49: x-Velocity at (0.2,0.75), $Str = 1$, $Re = 5000$, $(Wo = 88.6)$, $t \in [0, 7]$, $U(x, 1, t) = (max(\cos(\frac{2\pi t}{T}), 0), 0)$

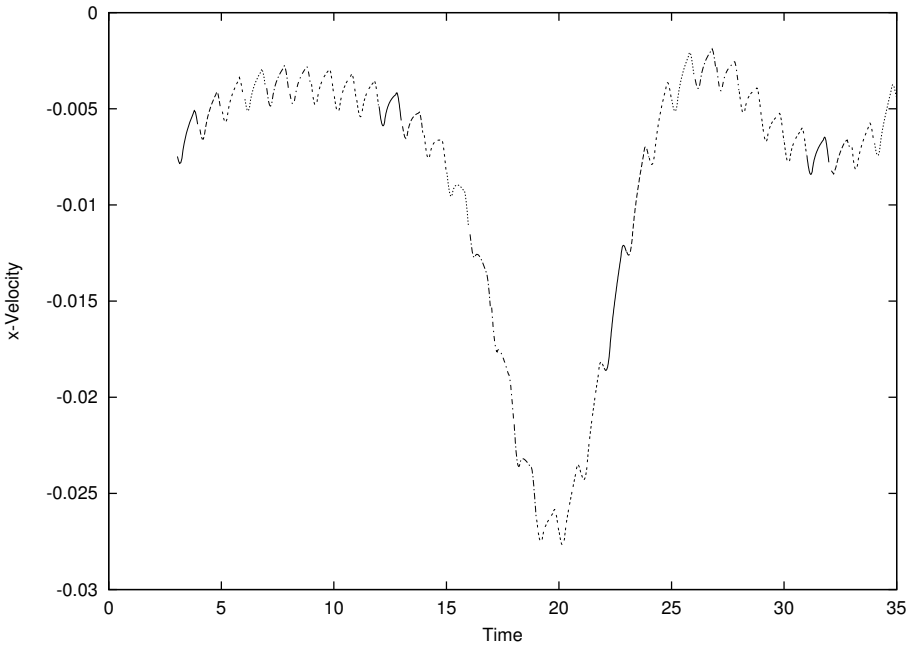

Figure 50: x-Velocity at (0.2,0.75), $Str = 1$, $Re = 8000$, $(Wo = 112.07)$, $t \in [2, 35]$, $U(x, 1, t) = (max(\cos(\frac{2\pi t}{T}), 0), 0)$

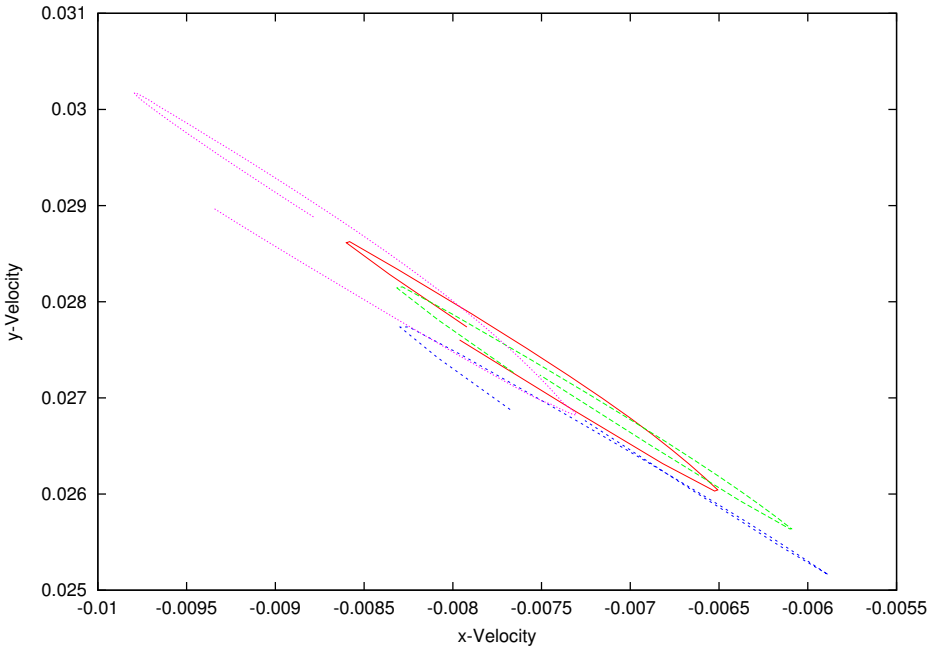

Figure 51: y-Velocity with respect to x-Velocity at (0.2,0.75), $Str = 1$, $Re = 5000$, $(Wo = 88.6)$, $t \in [4, 7]$, $U(x, 1, t) = (max(\cos(\frac{2\pi t}{T}), 0), 0)$

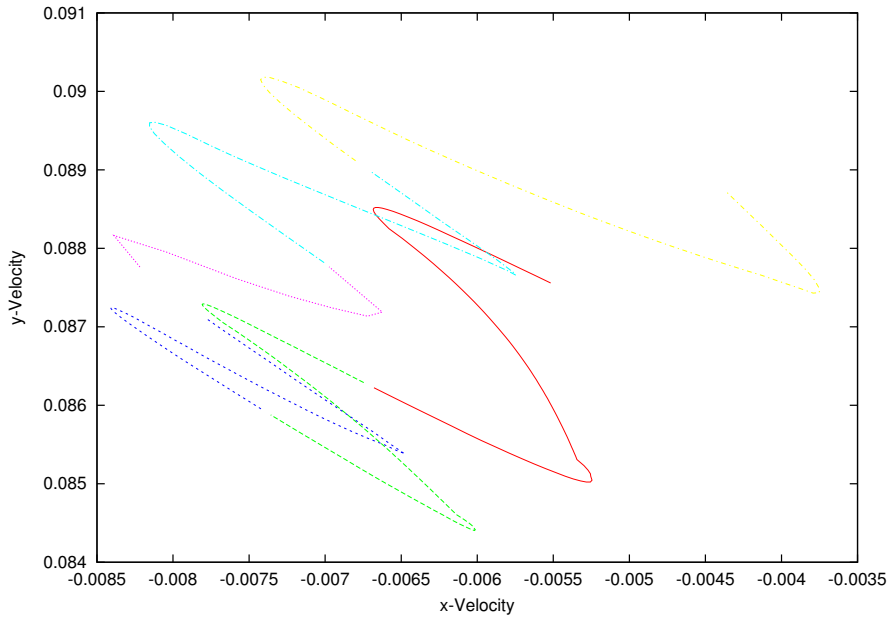

Figure 52: y-Velocity with respect to x-Velocity at (0.2,0.75), $Str = 1$, $Re = 8000$, $(Wo = 112.07)$, $t \in [32, 35]$, $U(x, 1, t) = (max(\cos(\frac{2\pi t}{T}), 0), 0)$

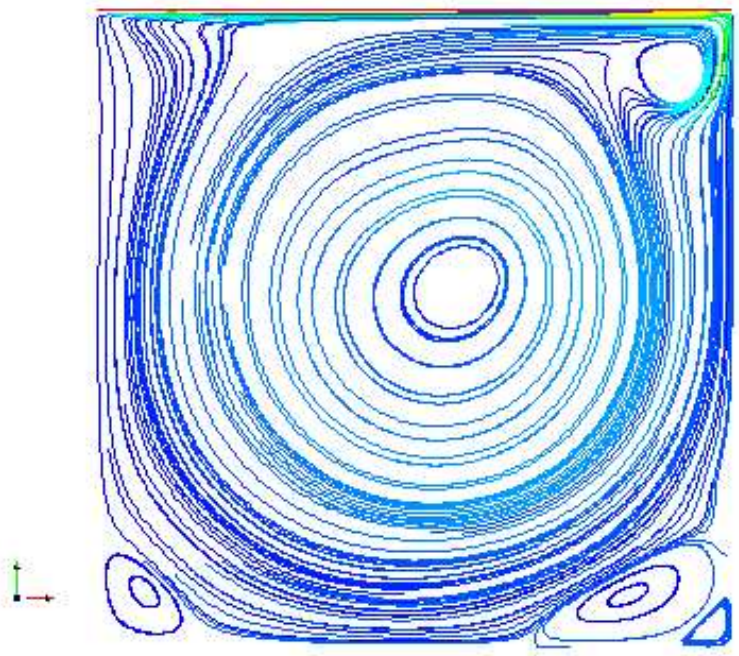

Figure 53: Streamlines colored by the $\| u \|$, $Str = 0.1$, $Re = 5000$, $(Wo = 28.01)$, $t = 190$, $U(x, 1, t) = (max(\cos(\frac{2\pi t}{T}), 0), 0)$

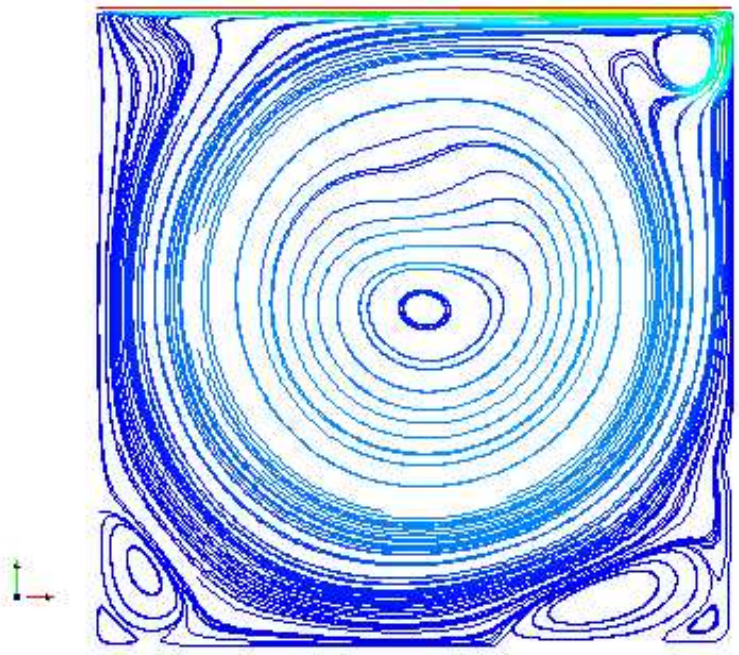

Figure 54: Streamlines colored by the $\| u \|$, $Str = 0.1$, $Re = 8000$, $(Wo = 35.44)$, $t = 160$, $U(x, 1, t) = (max(\cos(\frac{2\pi t}{T}), 0), 0)$

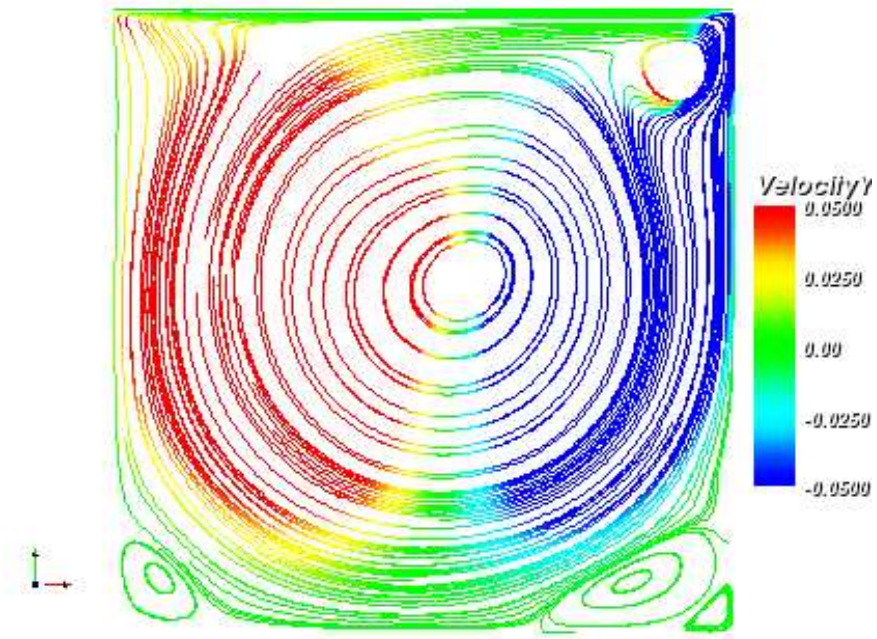

Figure 55: Streamlines colored by the y-velocity, $Str = 0.1$, $Re = 5000$, $(Wo = 28.01)$, $t = 190$, $U(x, 1, t) = (max(\cos(\frac{2\pi t}{T}), 0), 0)$

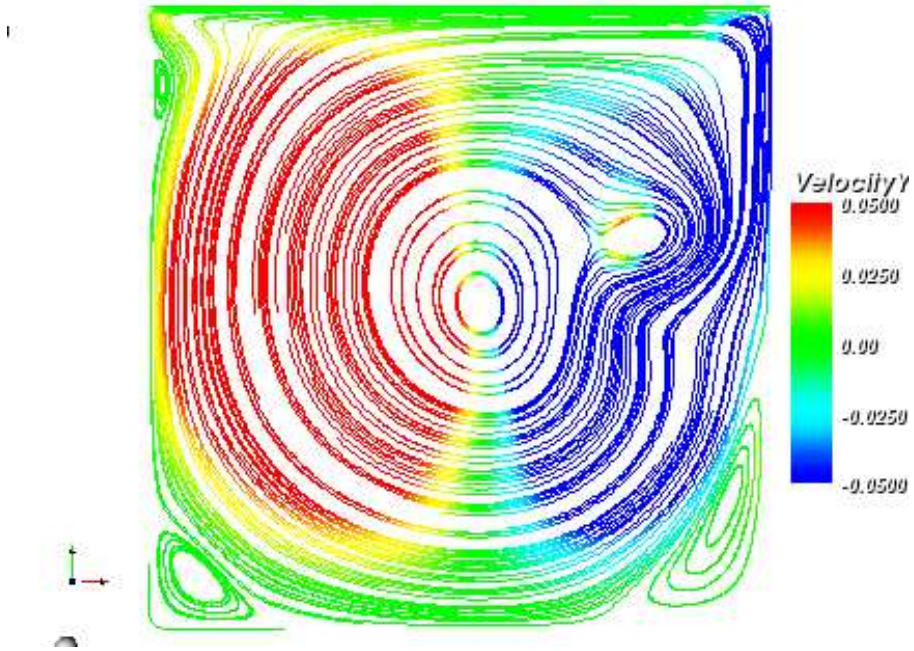

Figure 56: Streamlines colored by the y-velocity, $Str = 0.1$, $Re = 5000$, $(Wo = 28.01)$, $t = 190 + \frac{T}{4}$, $U(x, 1, t) = (max(\cos(\frac{2\pi t}{T}), 0), 0)$

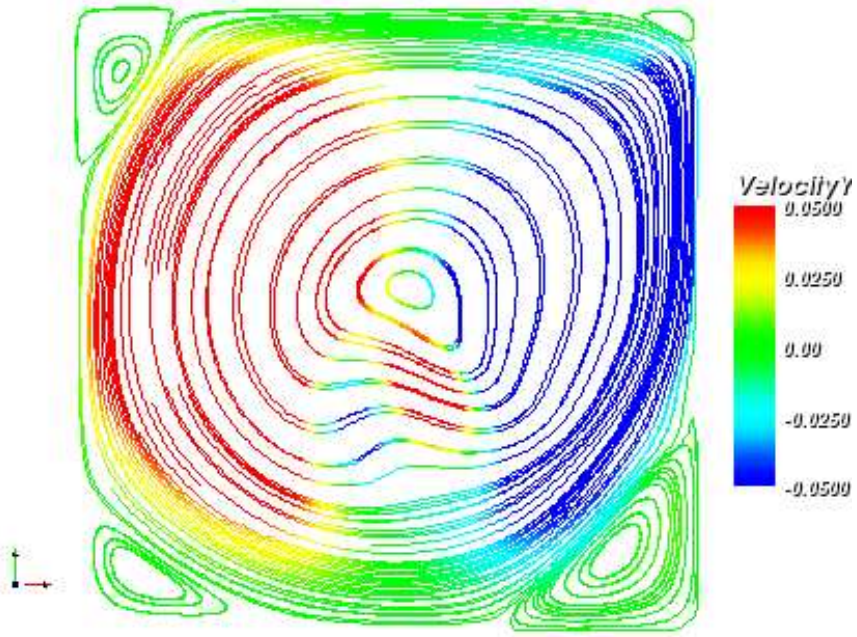

Figure 57: Streamlines colored by the y-velocity, $Str = 0.1$, $Re = 5000$, $(Wo = 28.01)$, $t = 190 + \frac{T}{2}$, $U(x, 1, t) = (max(\cos(\frac{2\pi t}{T}), 0), 0)$

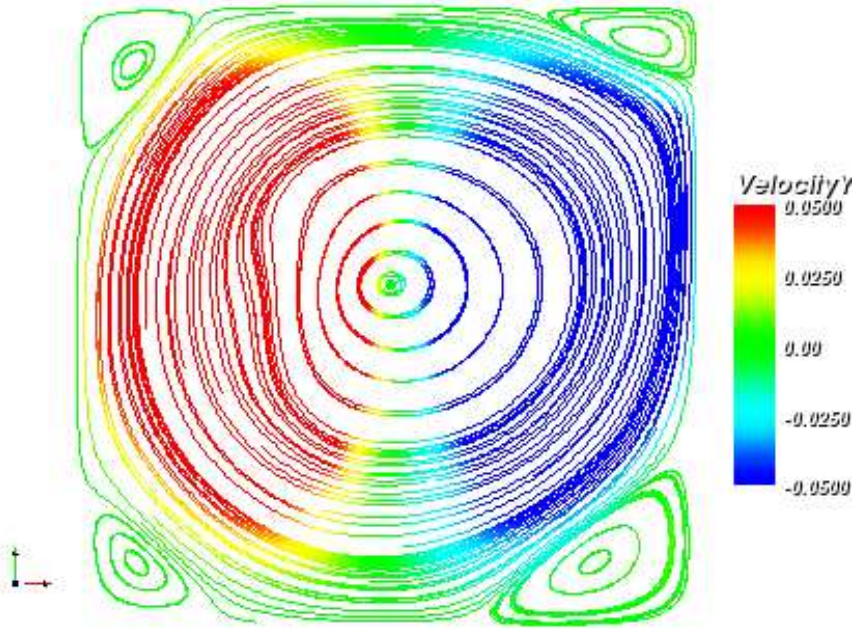

Figure 58: Streamlines colored by the y-velocity, $Str = 0.1$, $Re = 5000$, $(Wo = 28.01)$, $t = 190 + \frac{3T}{4}$, $U(x, 1, t) = (max(\cos(\frac{2\pi t}{T}), 0), 0)$

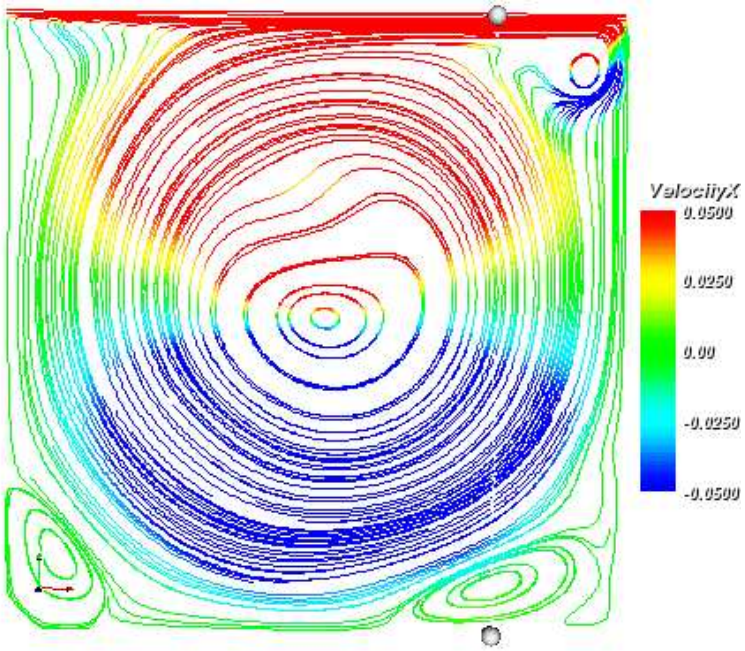

Figure 59: Streamlines colored by the y-velocity, $Str = 0.1$, $Re = 8000$, $(Wo = 35.44)$, $t = 160$, $U(x, 1, t) = (max(\cos(\frac{2\pi t}{T}), 0), 0)$

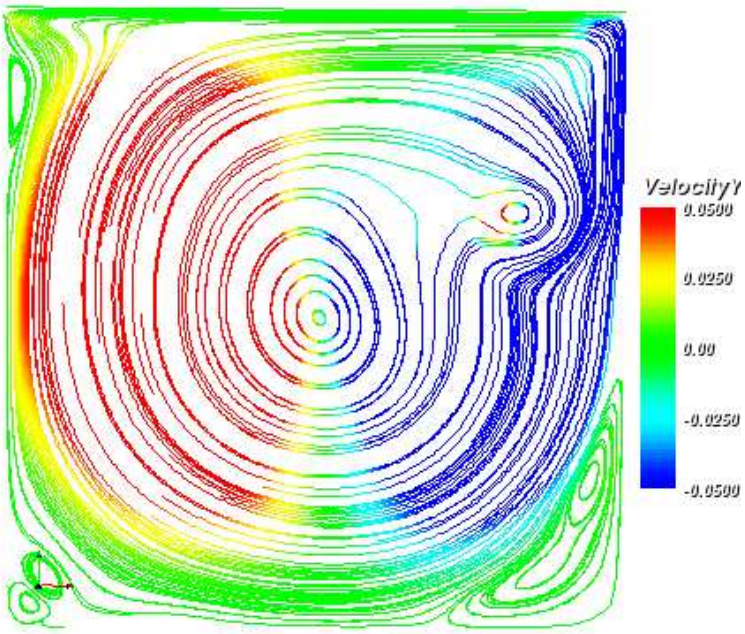

Figure 60: Streamlines colored by the y-velocity, $Str = 0.1$, $Re = 8000$, $(Wo = 35.44)$, $t = 160 + \frac{T}{4}$, $U(x, 1, t) = (max(\cos(\frac{2\pi t}{T}), 0), 0)$

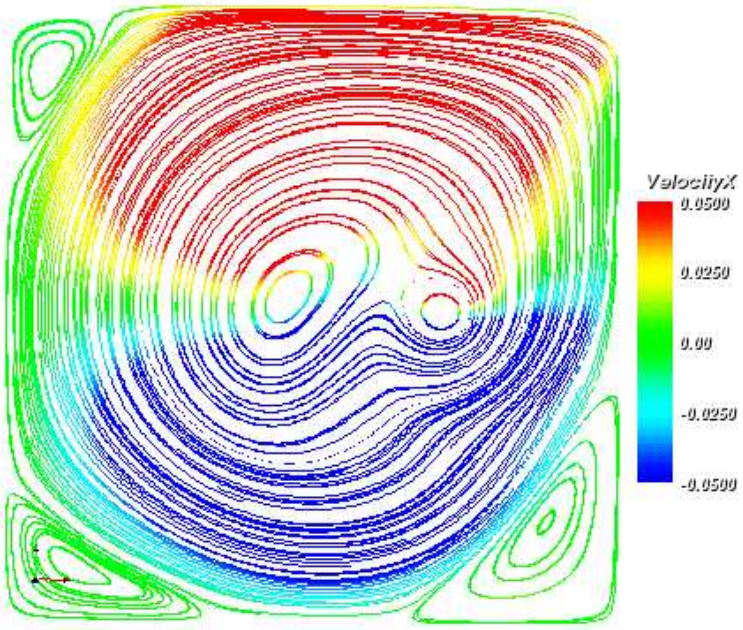

Figure 61: Streamlines colored by the y-velocity, $Str = 0.1$, $Re = 8000$, $(Wo = 35.44)$, $t = 160 + \frac{T}{2}$, $U(x, 1, t) = (max(\cos(\frac{2\pi t}{T}), 0), 0)$

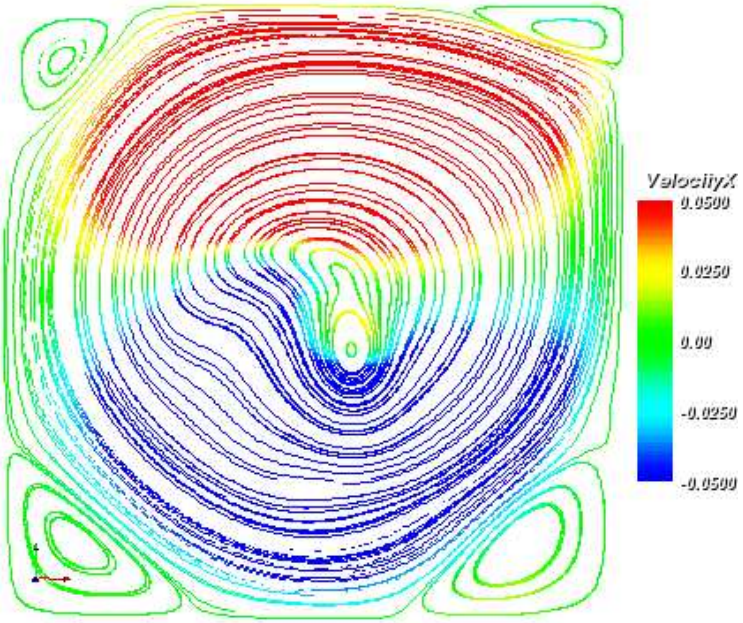

Figure 62: Streamlines colored by the y-velocity, $Str = 0.1$, $Re = 8000$, $(Wo = 35.44)$, $t = 16 + \frac{3T}{4}$, $U(x, 1, t) = (max(\cos(\frac{2\pi t}{T}), 0), 0)$

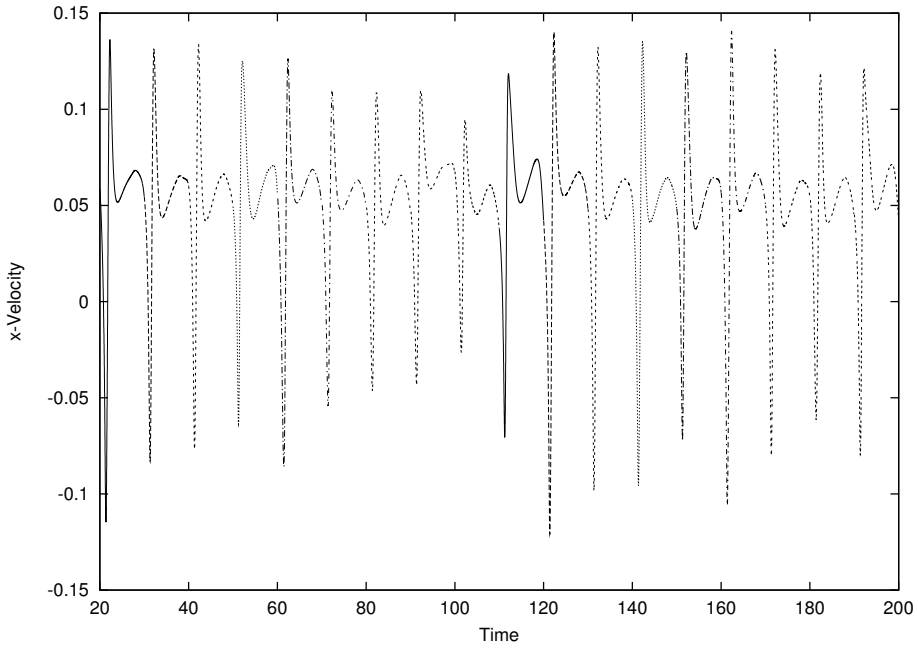

Figure 63: x-Velocity at (0.8,0.5), $Str = 0.1$, $Re = 5000$, $(Wo = 28.01)$, $t \in [20, 200]$, $U(x, 1, t) = (max(\cos(\frac{2\pi t}{T}), 0), 0)$

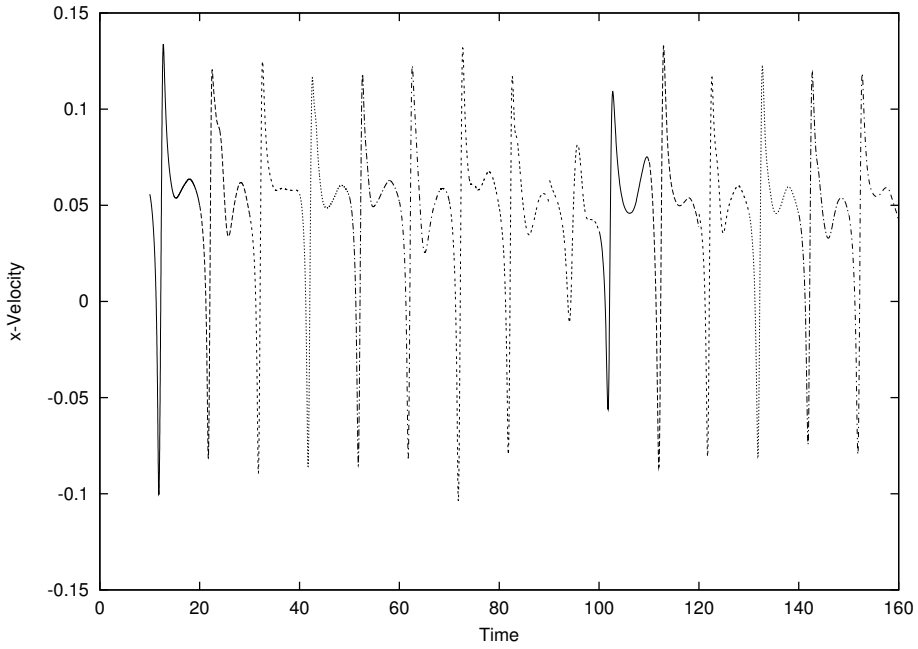

Figure 64: x-Velocity at (0.8,0.5), $Str = 0.1$, $Re = 8000$, $(Wo = 35.44)$, $t \in [10, 160]$, $U(x, 1, t) = (max(\cos(\frac{2\pi t}{T}), 0), 0)$

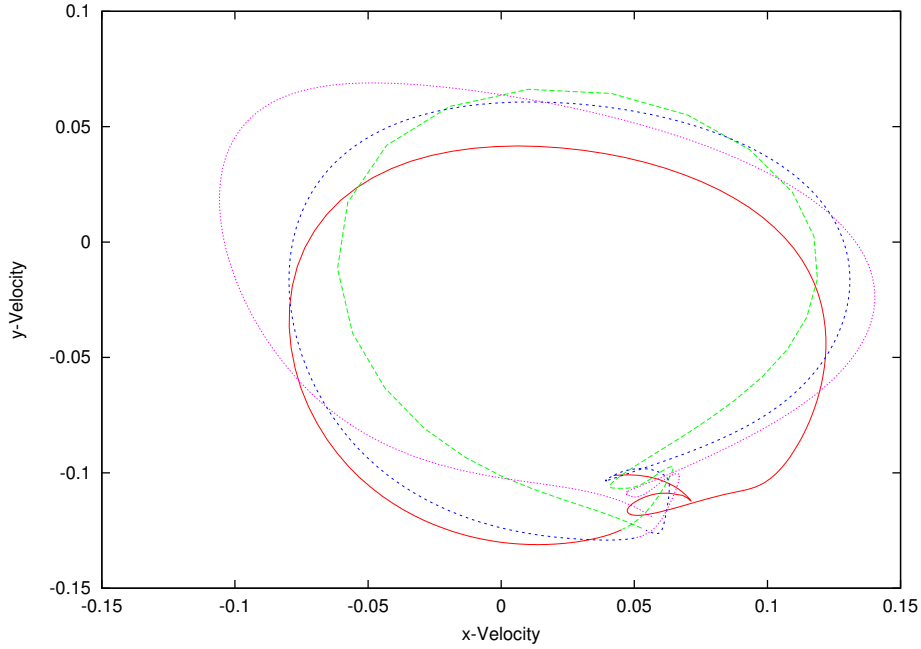

Figure 65: y-Velocity wrt x-Velocity at (0.8,0.5), $Str = 0.1$, $Re = 5000$, $(Wo = 28.01)$, $t \in [170, 200]$, $U(x, 1, t) = (max(\cos(\frac{2\pi t}{T}), 0), 0)$

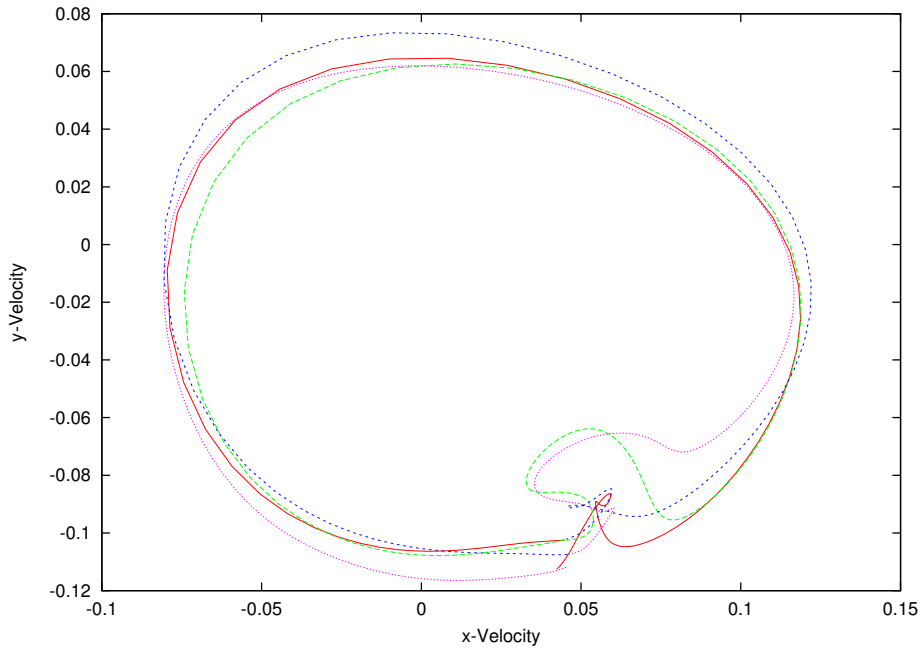

Figure 66: y-Velocity wrt x-Velocity at (0.8,0.5), $Str = 0.1$, $Re = 8000$, $(Wo = 35.44)$, $t \in [130, 160]$, $U(x, 1, t) = (max(\cos(\frac{2\pi t}{T}), 0), 0)$

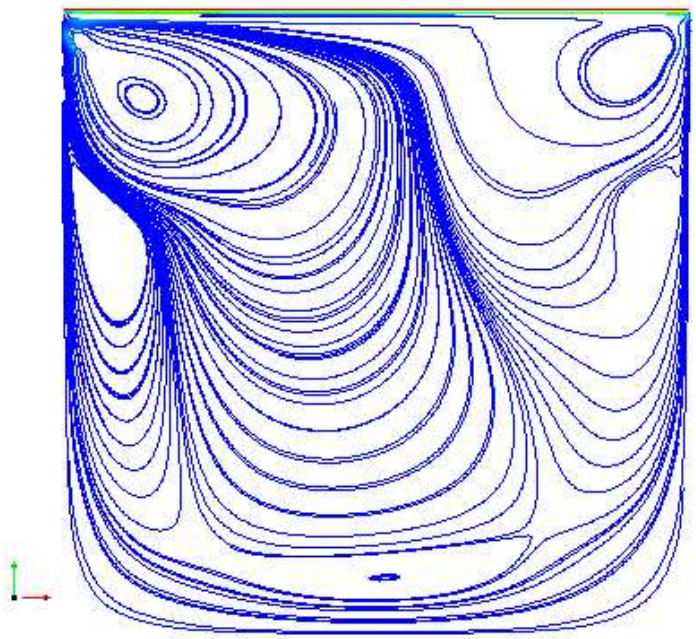

Figure 67: Streamlines colored by the $\| u \|$, $Str = 1$, $Re = 8000$, $(Wo = 112.07)$, $t = 14$, $U(x, 1, t) = \cos(\frac{2\pi t}{T})$

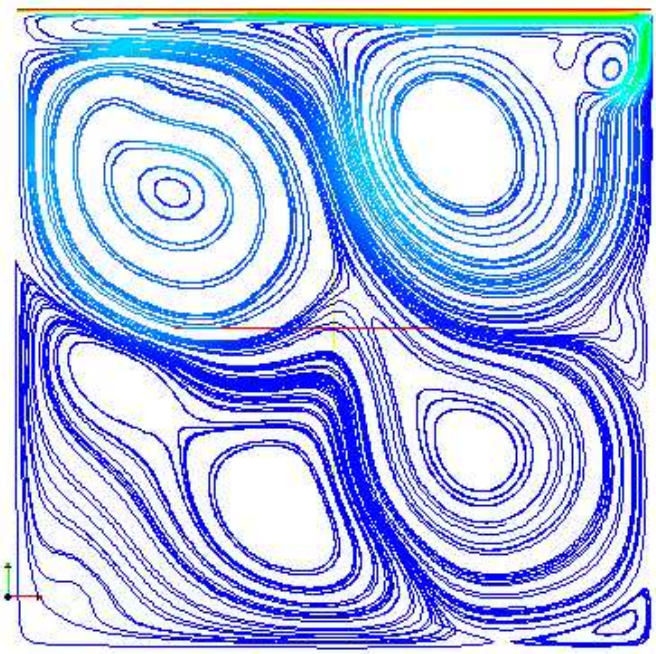

Figure 68: Streamlines colored by the $\| u \|$, $Str = 0.1$, $Re = 8000$, $(Wo = 35.44)$, $t = 190$, $U(x, 1, t) = \cos(\frac{2\pi t}{T})$

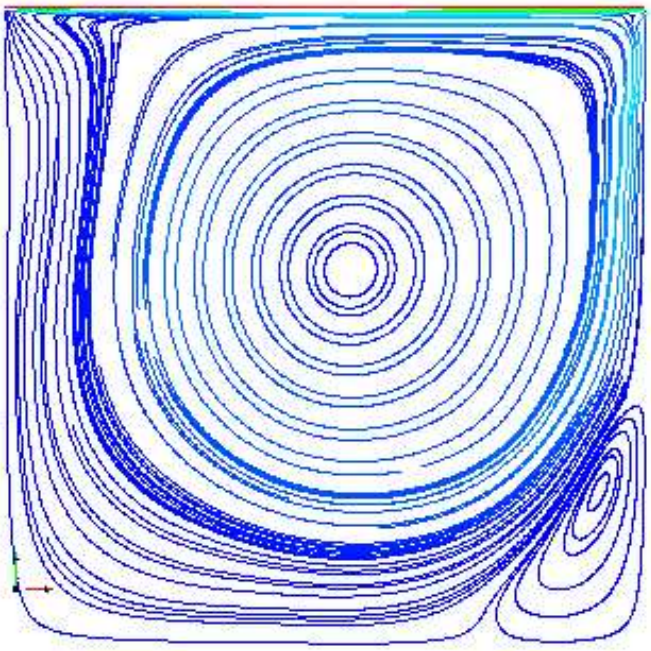

Figure 69: Streamlines colored by the $\| u \|$, $Str = 1$, $Re = 8000$, $(Wo = 112.07)$, $t = 30$, $U(x, 1, t) = max(\cos(\frac{2\pi t}{T}), 0)$

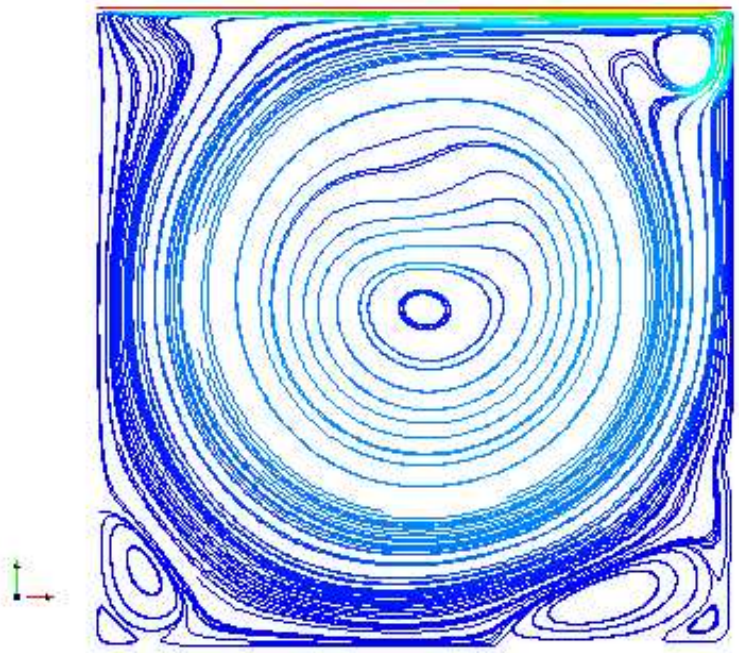

Figure 70: Streamlines colored by the $\| u \|$, $Str = 0.1$, $Re = 8000$, $(Wo = 35.44)$, $t = 190$, $U(x, 1, t) = max(\cos(\frac{2\pi t}{T}), 0)$

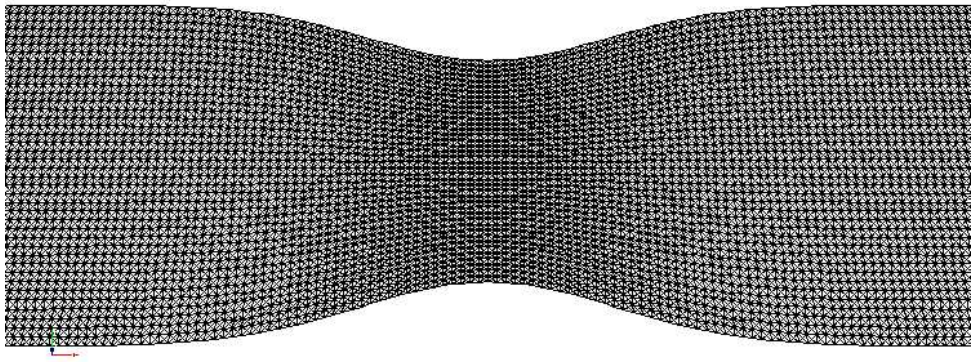

Figure 71: The geometry of the computational domain

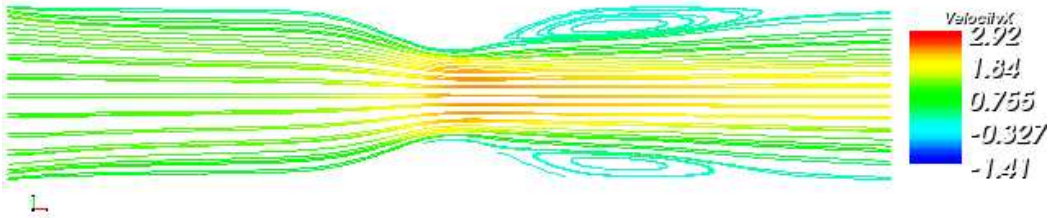

Figure 72: Streamlines colored by the x-velocity,$Str = 0$, $Re = 200$, $(Wo = 0)$, $t = 60$

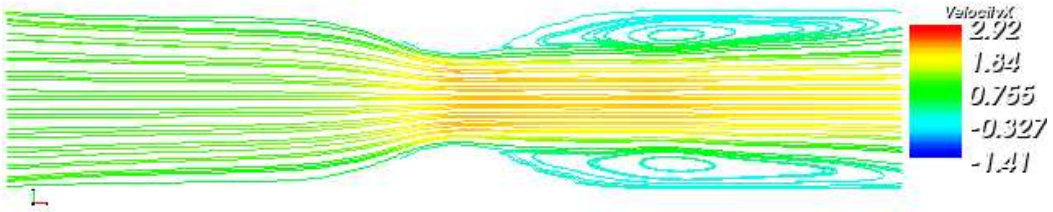

Figure 73: Streamlines colored by the x-velocity, $Str = 0$, $Re = 400$, $(Wo = 0)$, $t = 60$

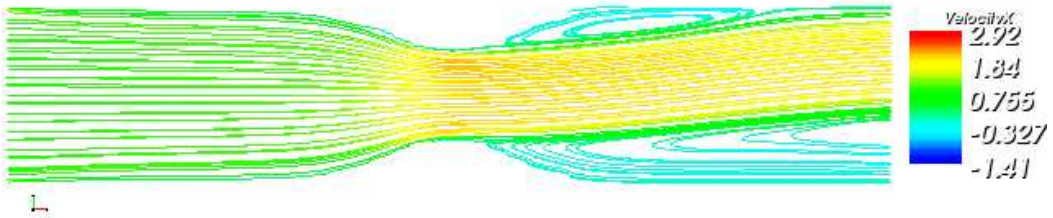

Figure 74: Streamlines colored by the x-velocity, $Str = 0$, $Re = 1200$, $(Wo = 0)$, $t = 60$

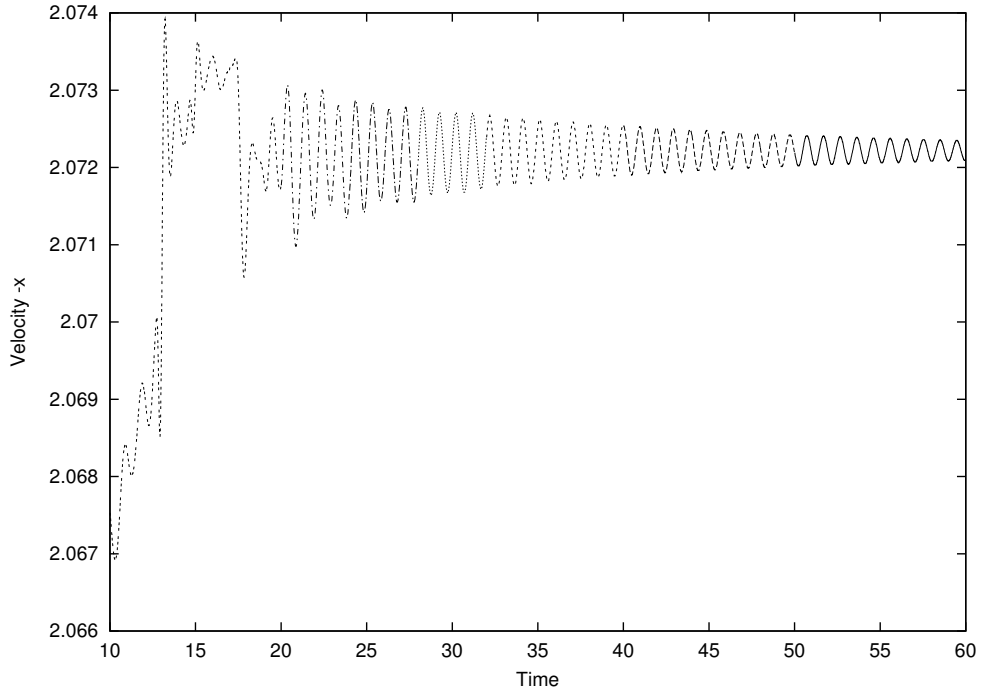

Figure 75: x-Velocity at $(3.2, 0.75)$, $Str = 0$, $Re = 1200$, $(Wo = 0)$, $t \in [10, 60]$

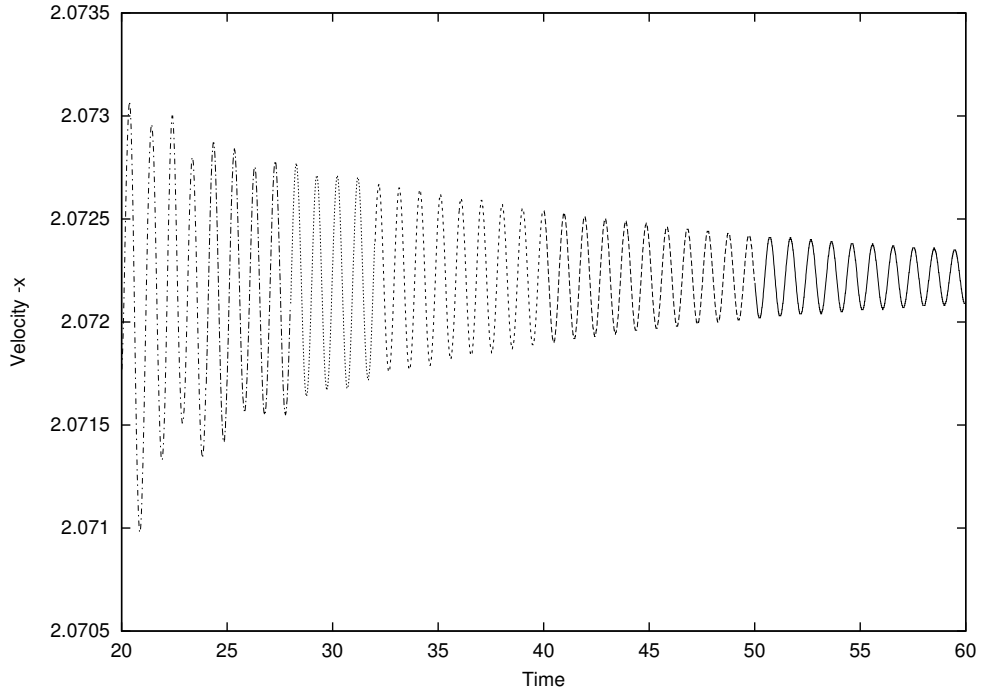

Figure 76: x-Velocity at $(3.2, 0.75)$, $Str = 0$, $Re = 1200$, $(Wo = 0)$, $t \in [20, 60]$

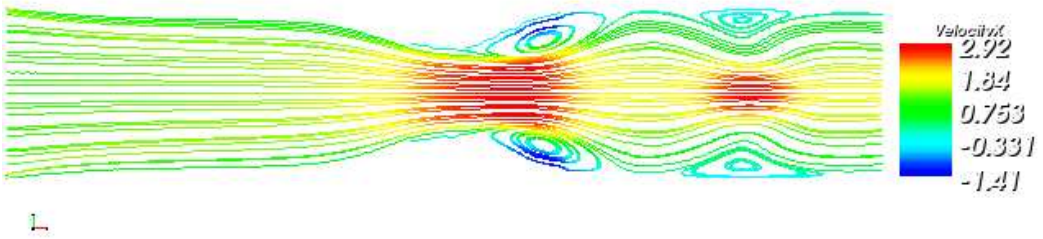

Figure 77: Streamlines colored by the x-velocity, $Str = 1$, $Re = 200$, $(Wo = 17.72)$, $t = 8$

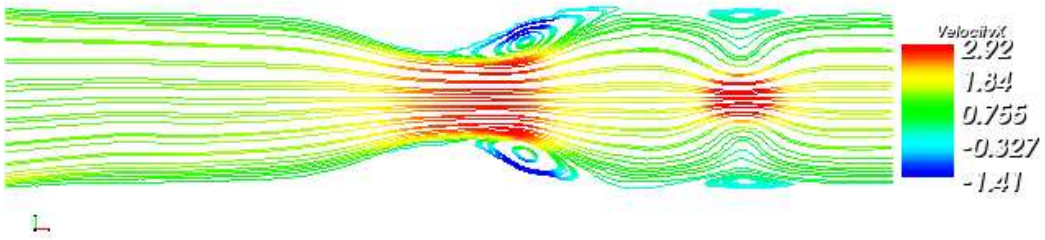

Figure 78: Streamlines colored by the x-velocity, $Str = 1$, $Re = 400$, $(Wo = 25.05)$, $t = 8$

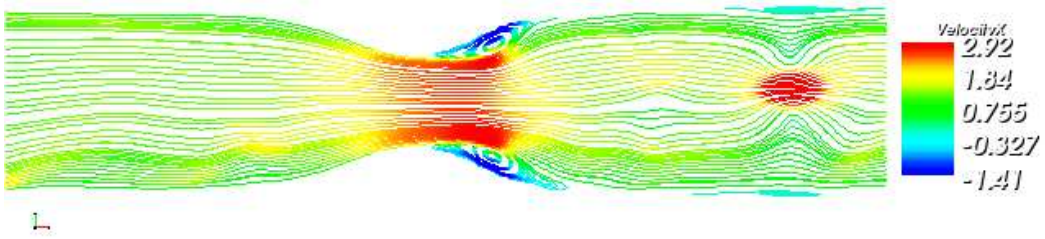

Figure 79: Streamlines colored by the x-velocity, $Str = 1$, $Re = 1200$, $(Wo = 43.4)$, $t = 11$

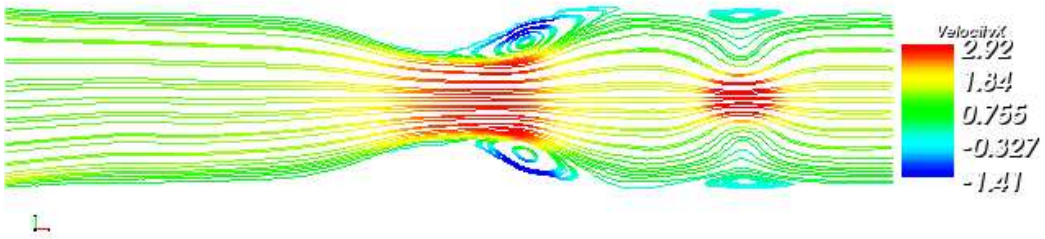

Figure 80: Streamlines colored by the x-velocity,$Str = 1$, $Re = 400$, $(Wo = 25.05)$, $t = 8$

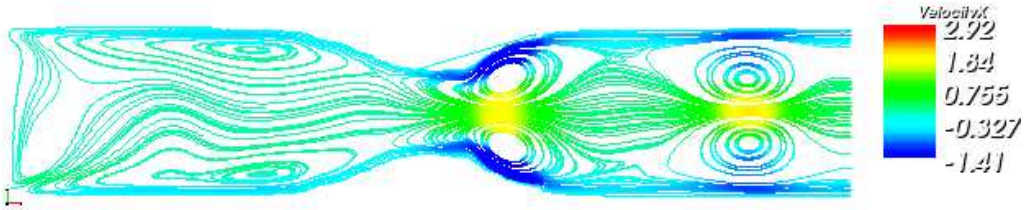

Figure 81: Streamlines colored by the x-velocity, $Str = 1$, $Re = 400$, $(Wo = 25.05)$, $t = 8 + \frac{T}{4}$

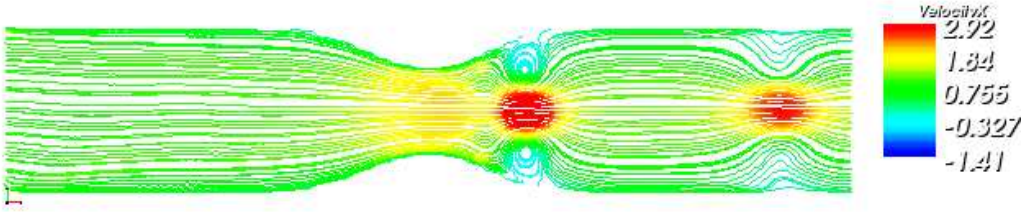

Figure 82: Streamlines colored by the x-velocity, $Str = 1$, $Re = 400$, $(Wo = 25.05)$, $t = 8 + \frac{T}{2}$

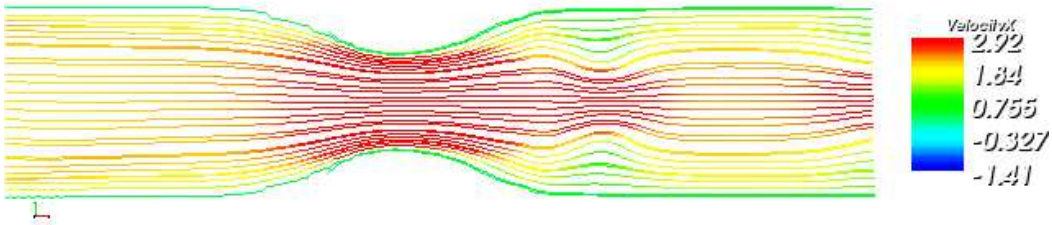

Figure 83: Streamlines colored by the x-velocity, $Str = 1$, $Re = 400$, $(Wo = 25.05)$, $t = 8 + \frac{3T}{4}$

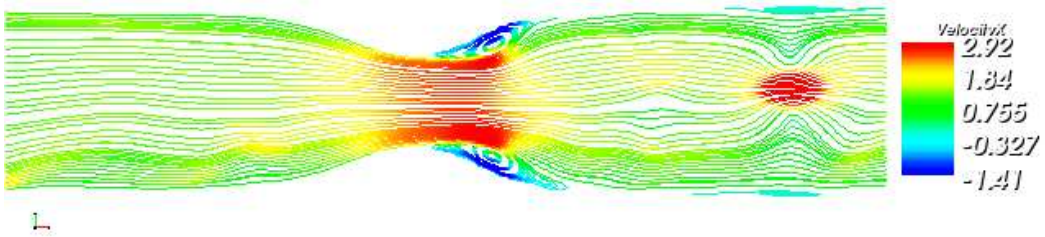

Figure 84: Streamlines colored by the x-velocity,$Str = 1$, $Re = 1200$, $(Wo = 43.4)$, $t = 11$

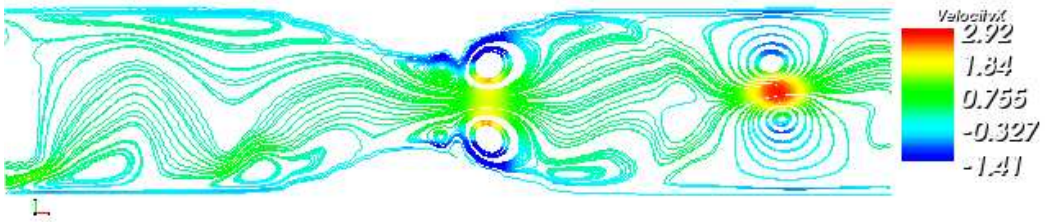

Figure 85: Streamlines colored by the x-velocity, $Str = 1$, $Re = 1200$, $(Wo = 43.4)$, $t = 11 + \frac{T}{4}$

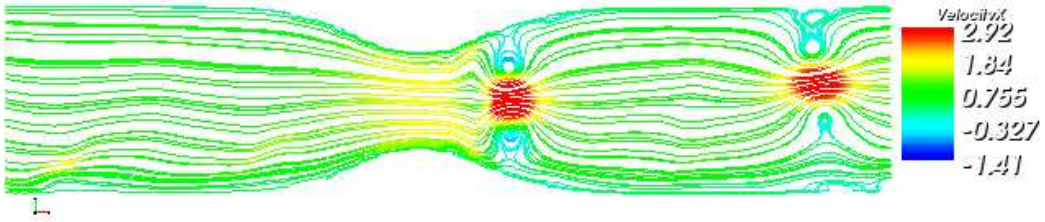

Figure 86: Streamlines colored by the x-velocity, $Str = 1$, $Re = 1200$, $(Wo = 43.4)$, $t = 11 + \frac{T}{2}$

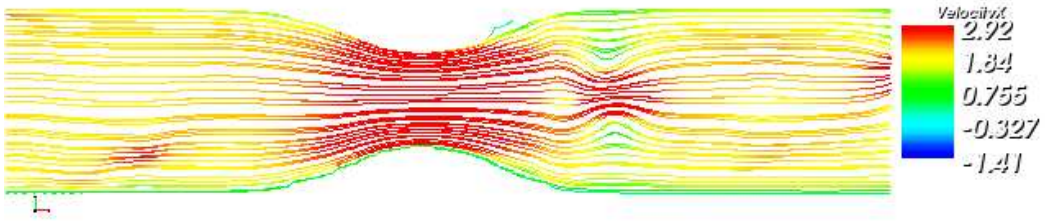

Figure 87: Streamlines colored by the x-velocity, $Str = 1$, $Re = 1200$, $(Wo = 43.4)$, $t = 11 + \frac{3T}{4}$

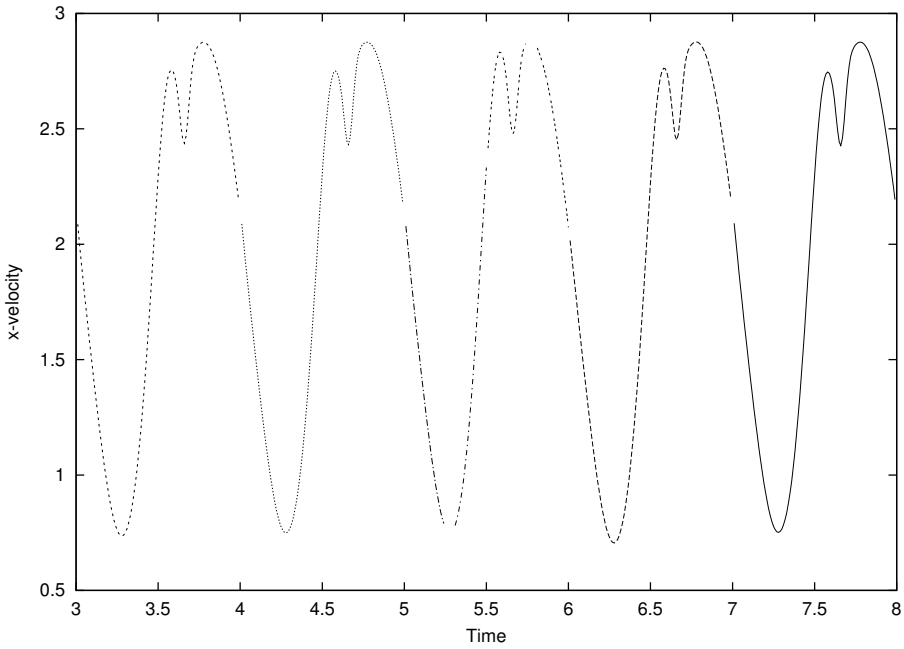

Figure 88: x-Velocity at $(3.2, 0.75)$, $Re = 400$, $Str = 1$, $(Wo = 25.05)$, $t \in [3, 8]$

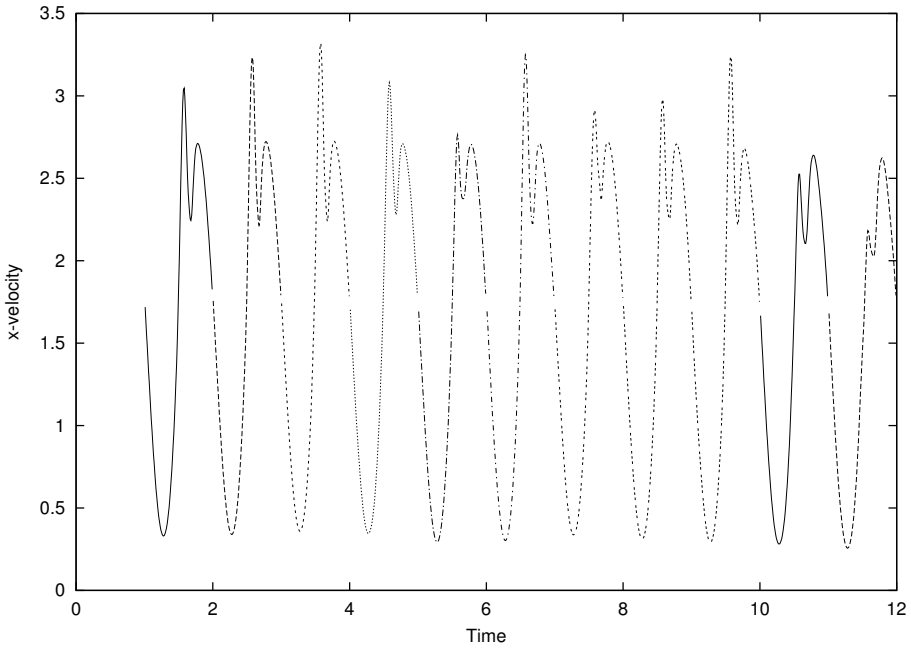

Figure 89: x-Velocity at $(3.2, 0.75)$, $Re = 1200$, $Str = 1$, $(Wo = 43.4)$, $t \in [0, 8]$

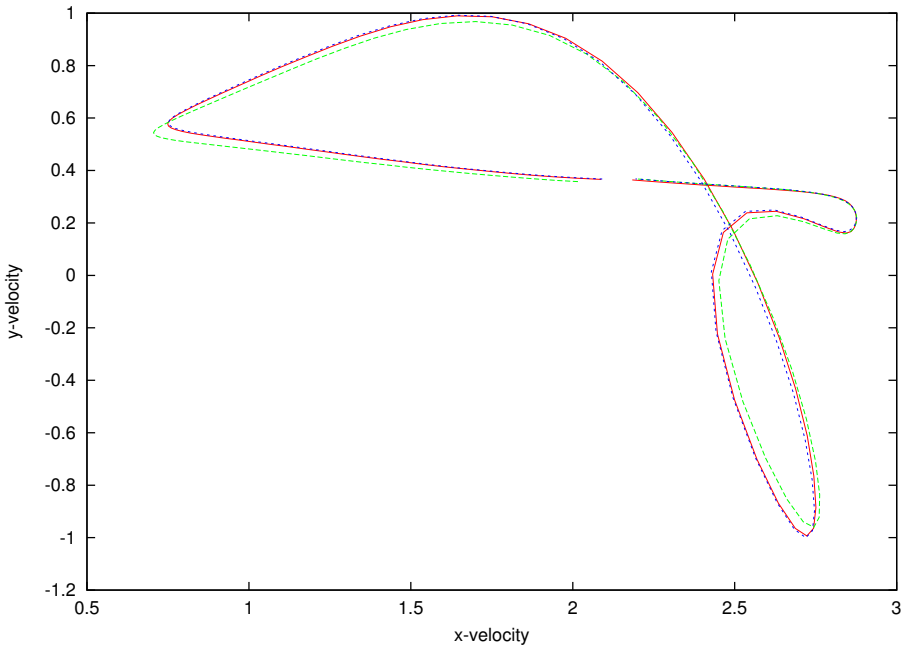

Figure 90: y-Velocity wrt x-Velocity at $(3.2, 0.75)$, $Re = 400$, $Str = 1$, $(Wo = 25.05)$, $t \in [6, 8]$

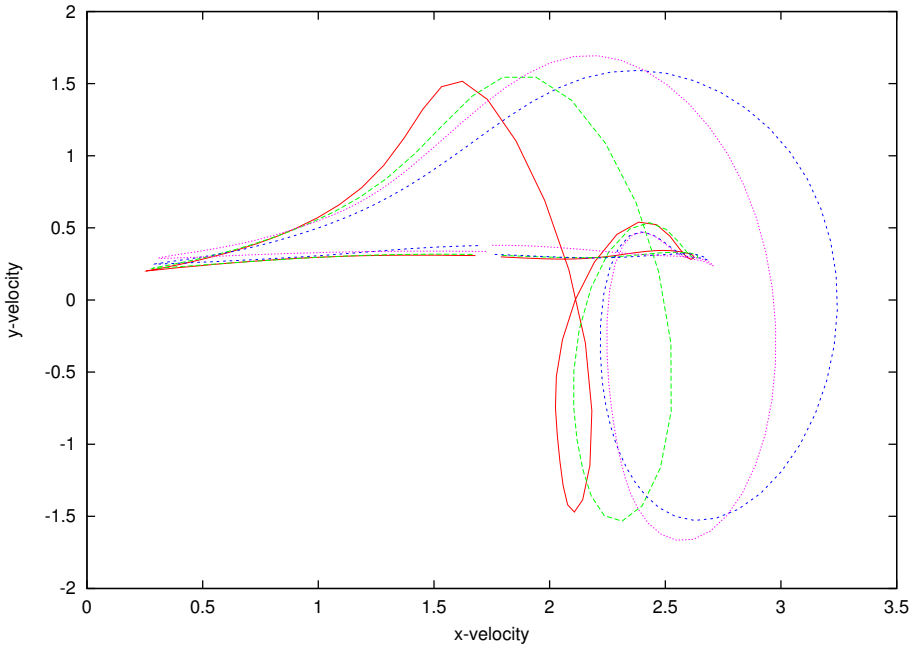

Figure 91: y-Velocity wrt x-Velocity at $(3.2, 0.75)$, $Re = 1200$, $Str = 1$, $(Wo = 43.4)$, $t \in [9, 12]$

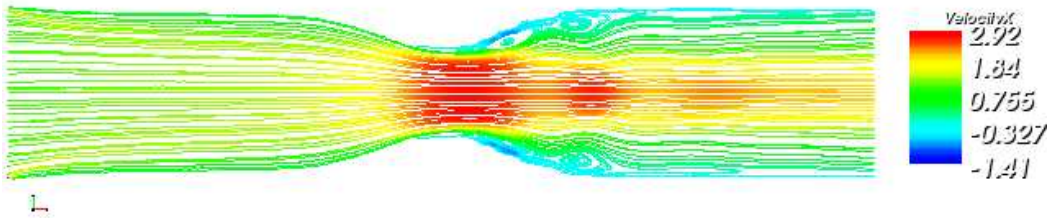

Figure 92: Streamlines colored by the x-velocity, $Str = 2$, $Re = 200$, $(Wo = 25.05)$, $t = 2$

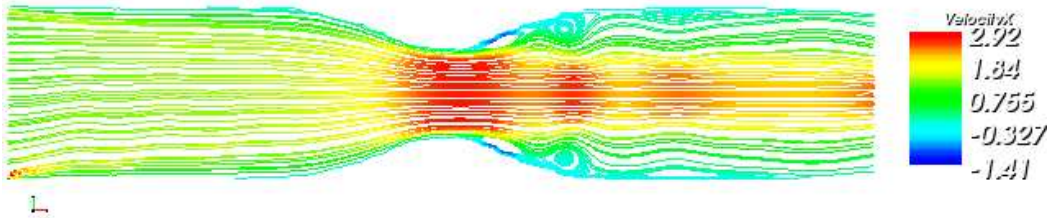

Figure 93: Streamlines colored by the x-velocity, $Str = 2$, $Re = 400$, $(Wo = 35.44)$, $t = 2$

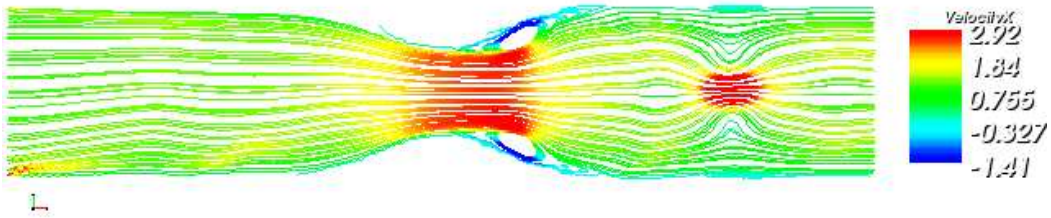

Figure 94: Streamlines colored by the x-velocity, $Str = 2$, $Re = 1200$, $(Wo = 61.38)$, $t = 2$

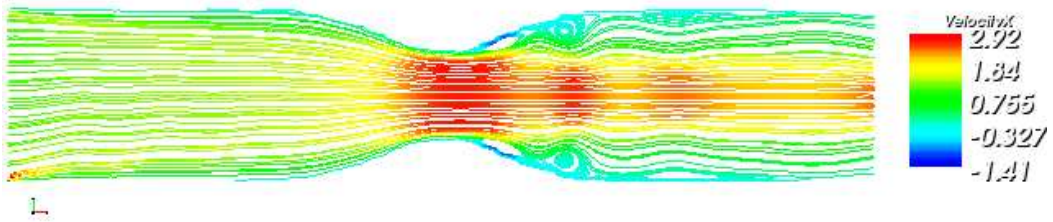

Figure 95: Streamlines colored by the x-velocity, $Str = 2$, $Re = 400$, $(Wo = 35.44)$, $t = 1.5$

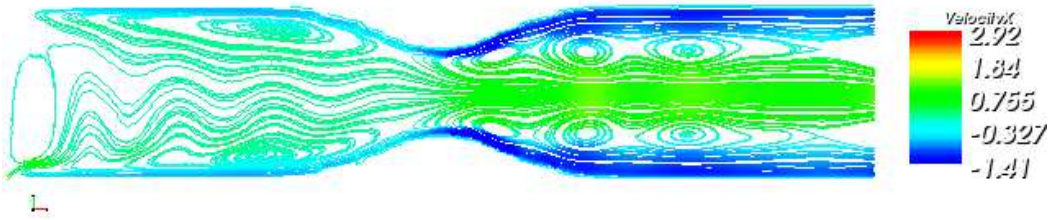

Figure 96: Streamlines colored by the x-velocity, $Str = 2$, $Re = 400$, $(Wo = 35.44)$, $t = 1.5 + \frac{T}{4}$

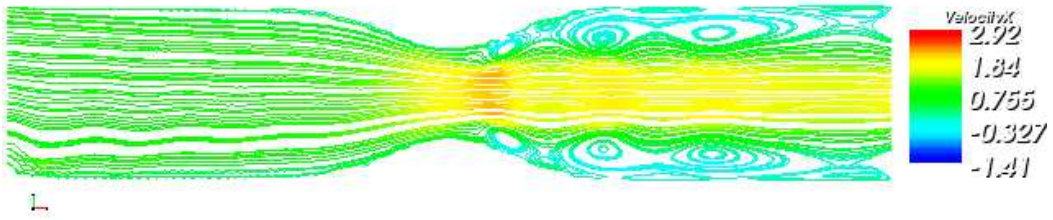

Figure 97: Streamlines colored by the x-velocity, $Str = 2$, $Re = 400$, $(Wo = 35.44)$, $t = 1.5 + \frac{T}{2}$

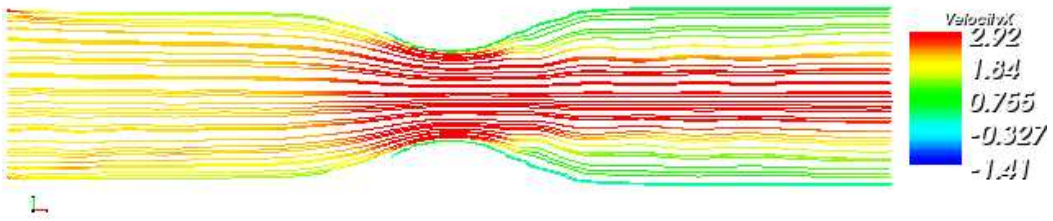

Figure 98: Streamlines colored by the x-velocity, $Str = 2$, $Re = 400$, $(Wo = 35.44)$, $t = 1.5 + \frac{3T}{4}$

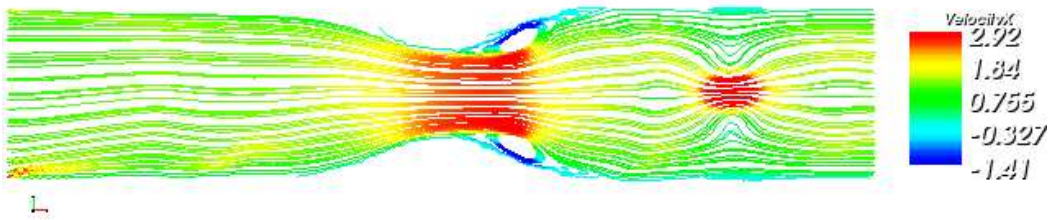

Figure 99: Streamlines colored by the x-velocity, $Str = 2$, $Re = 1200$, $(Wo = 61.38)$, $t = 3$

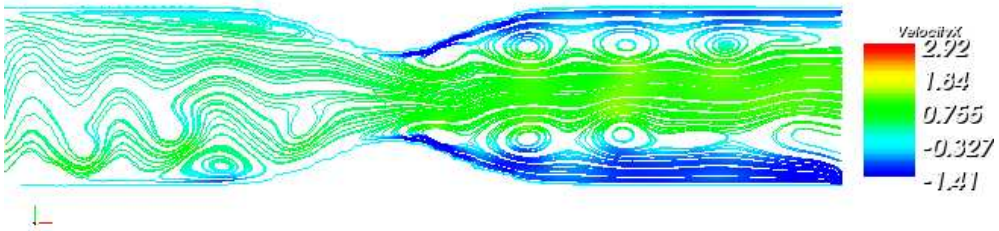

Figure 100: Streamlines colored by the x-velocity, $Str = 2$, $Re = 1200$, $(Wo = 61.38)$, $t = 3 + \frac{T}{4}$

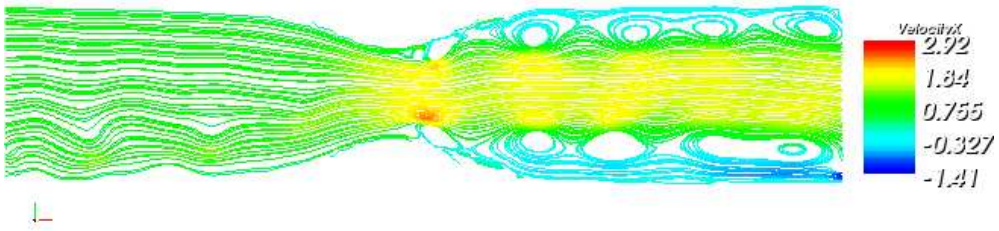

Figure 101: Streamlines colored by the x-velocity, $Str = 2$, $Re = 1200$, $(Wo = 61.38)$, $t = 3 + \frac{T}{2}$

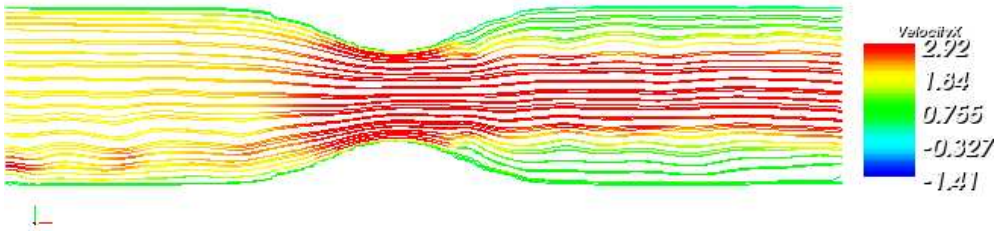

Figure 102: Streamlines colored by the x-velocity, $Str = 2$, $Re = 1200$, $(Wo = 61.38)$, $t = 3 + \frac{3T}{4}$

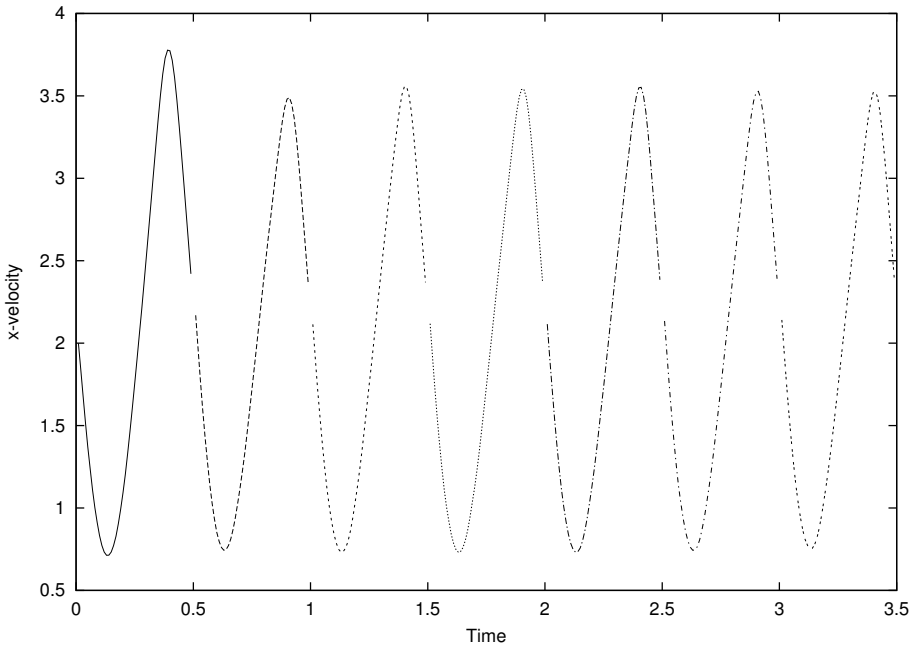

Figure 103: x-Velocity at $(3.2, 0.75)$, $Re = 400$, $Str = 2$, $(Wo = 35.44)$, $t \in [0, 3.5]$

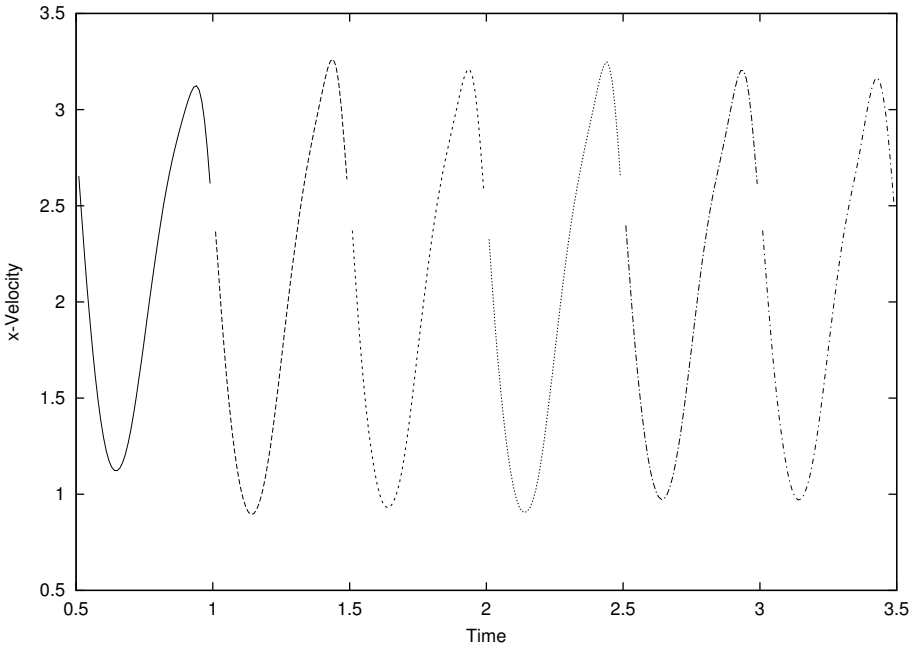

Figure 104: x-Velocity at $(3.2, 0.75)$, $Re = 1200$, $Str = 2$, $(Wo = 61.38)$, $t \in [0.5, 3.5]$

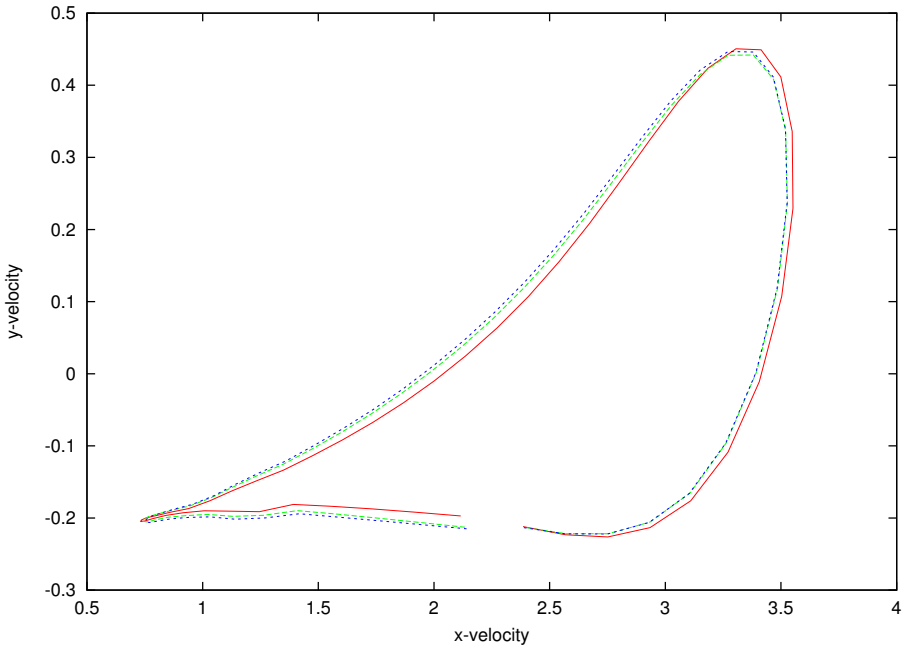

Figure 105: y-Velocity wrt x-Velocity at $(3.2, 0.75)$, $Re = 400$, $Str = 2$, $(Wo = 35.44)$, $t \in [2.5, 3.5]$

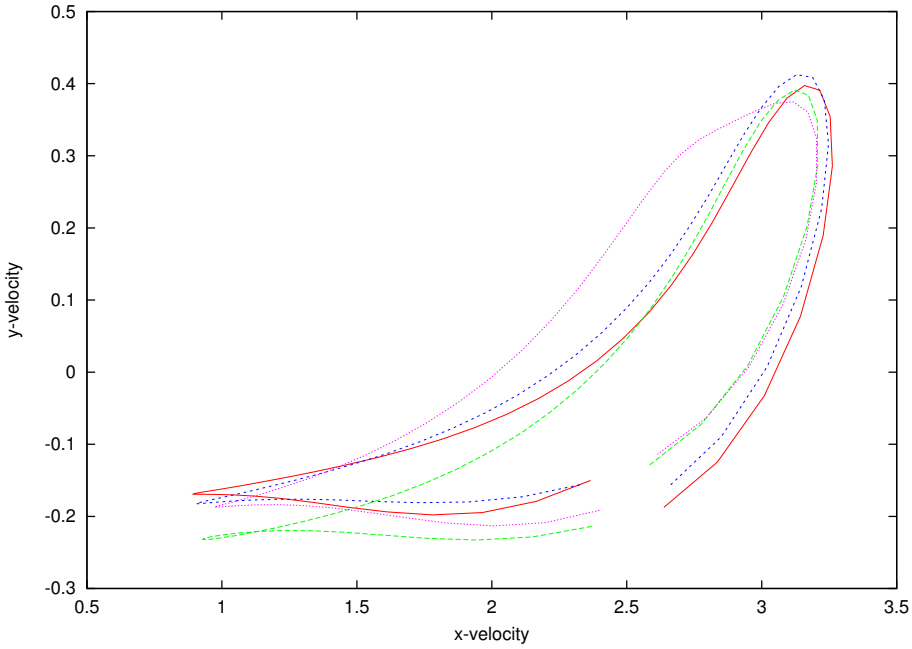

Figure 106: y-Velocity wrt x-Velocity at $(3.2, 0.75)$, $Re = 1200$, $Str = 2$, $(Wo = 61.38)$, $t \in [2, 3.5]$

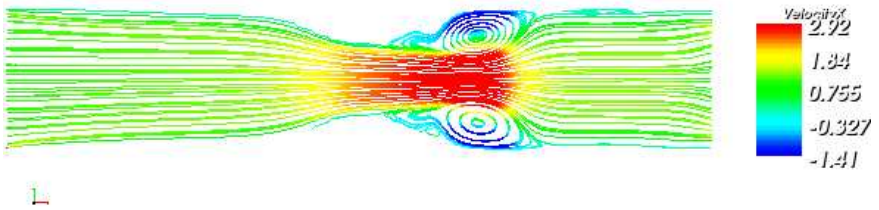

Figure 107: Streamlines colored by the x-velocity, $Str = 0.5$, $Re = 400$, $(Wo = 17.72)$, $t = 12$

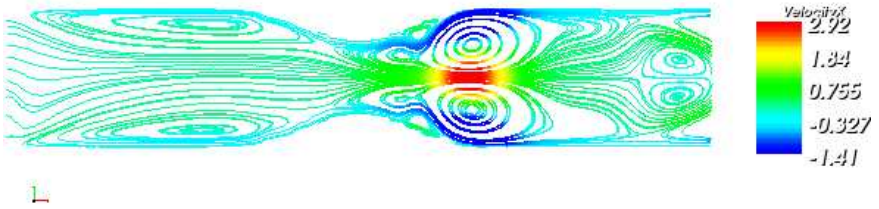

Figure 108: Streamlines colored by the x-velocity, $Str = 0.5$, $Re = 400$, $(Wo = 17.72)$, $t = 12 + \frac{T}{4}$

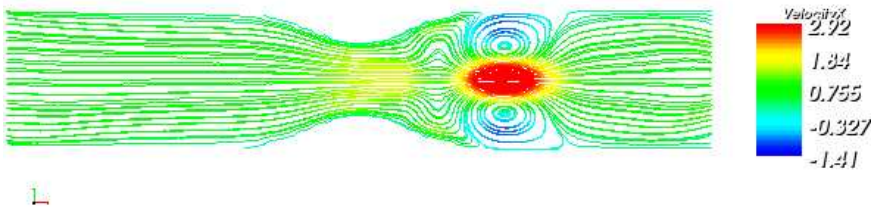

Figure 109: Streamlines colored by the x-velocity, $Str = 0.5$, $Re = 400$, $(Wo = 17.72)$, $t = 12 + \frac{T}{2}$

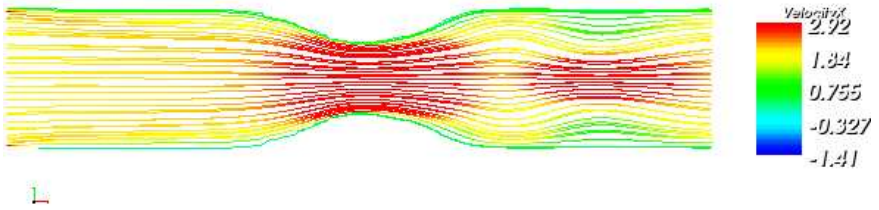

Figure 110: Streamlines colored by the x-velocity, $Str = 0.5$, $Re = 400$, $(Wo = 17.72)$, $t = 12 + \frac{3T}{4}$

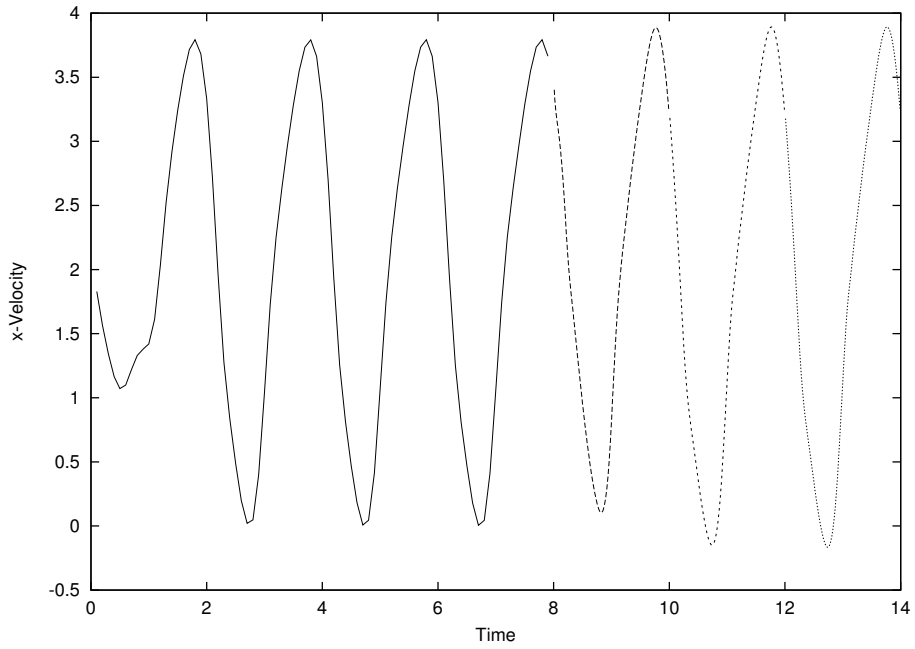

Figure 111: x-Velocity at $(3.2, 0.75)$, $Re = 400$, $Str = 0.5$, $(Wo = 17.72)$, $t \in [0, 14]$

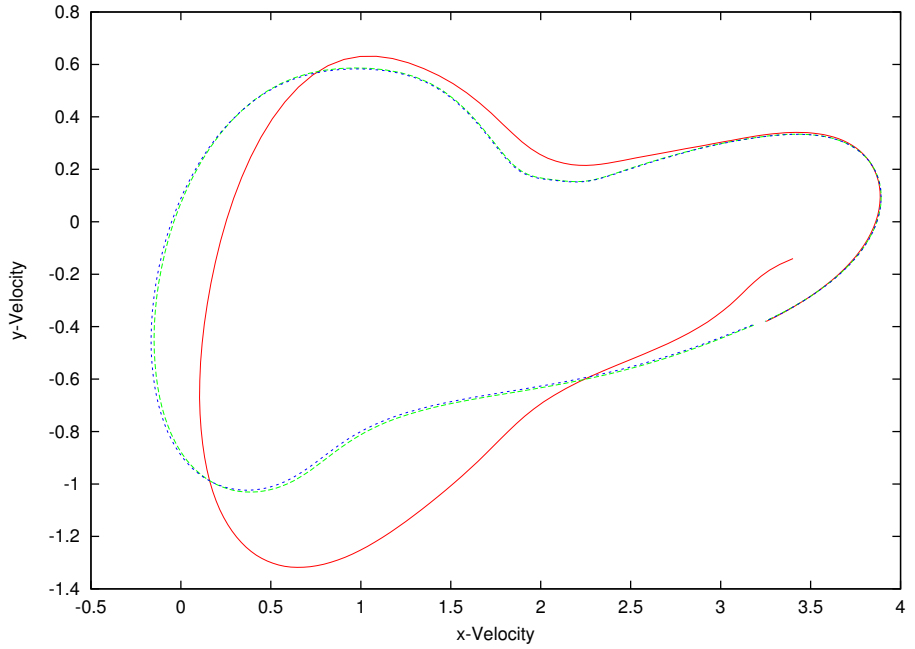

Figure 112: y-Velocity wrt x-Velocity at $(3.2, 0.75)$, $Re = 400$, $Str = 0.5$, $(Wo = 17.72)$, $t \in [8, 14]$

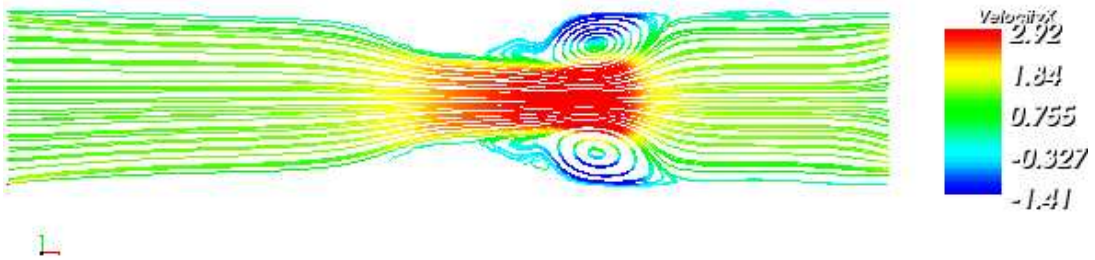

Figure 113: Streamlines colored by the x-velocity, $Str = 0.5$, $Re = 400$, $(Wo = 17.72)$, $t = 12$

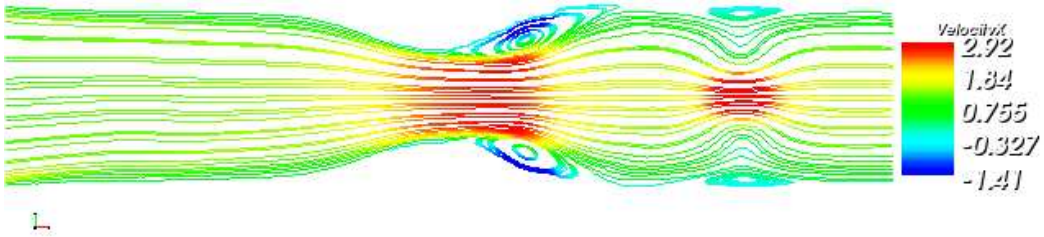

Figure 114: Streamlines colored by the x-velocity, $Str = 1$, $Re = 400$, $(Wo = 25.05)$, $t = 11$

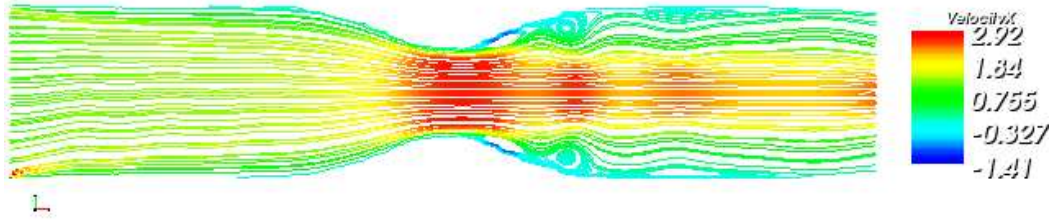

Figure 115: Streamlines colored by the x-velocity, $Str = 2$, $Re = 400$, $(Wo = 35.44)$, $t = 3$

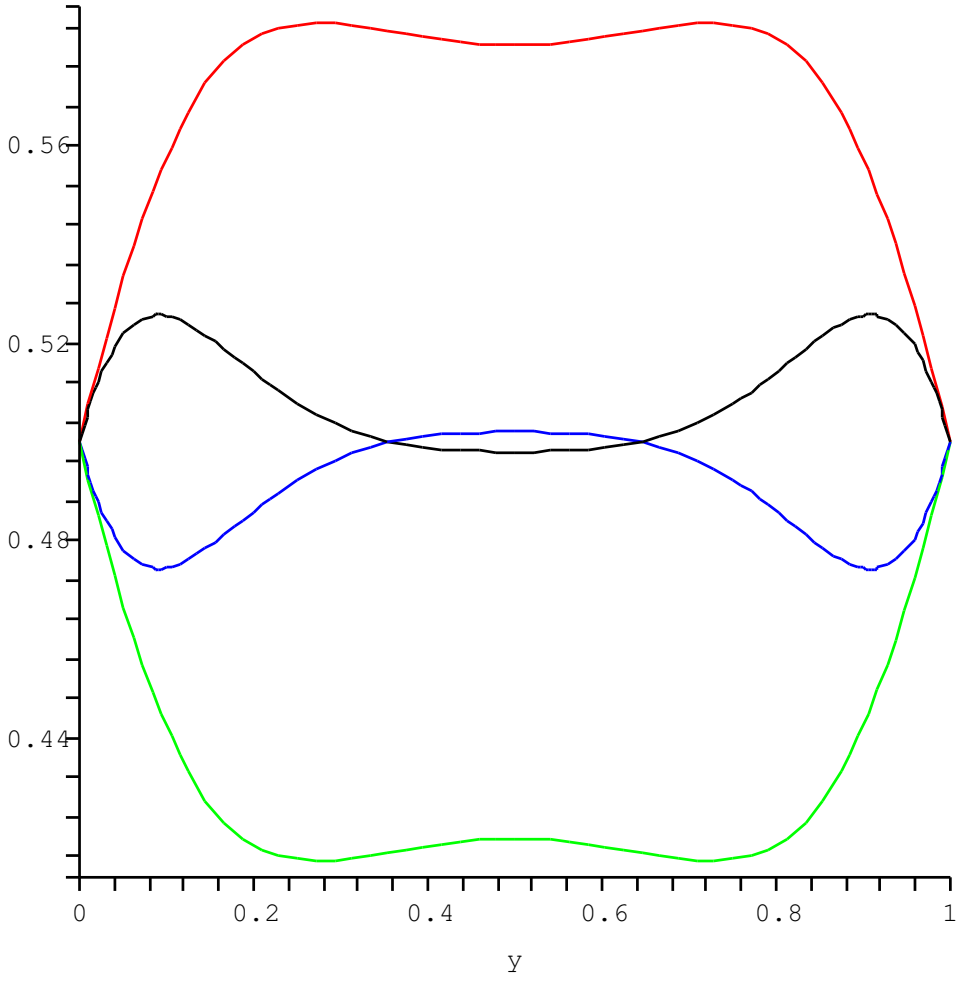

Figure 116: Velocity profile: at $\frac{T}{4}$ (red), $\frac{T}{2}$ (blue), $\frac{3T}{4}$ (green), T (black)

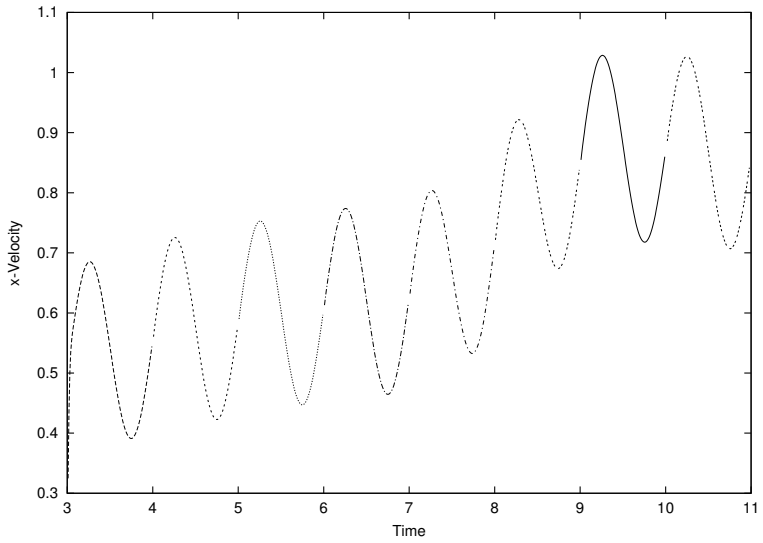

Figure 117: x-Velocity at $(4.02, 0.875)$, $Str = 1$, $Re = 400$, $(Wo = 25.05)$, $t \in [3, 11]$

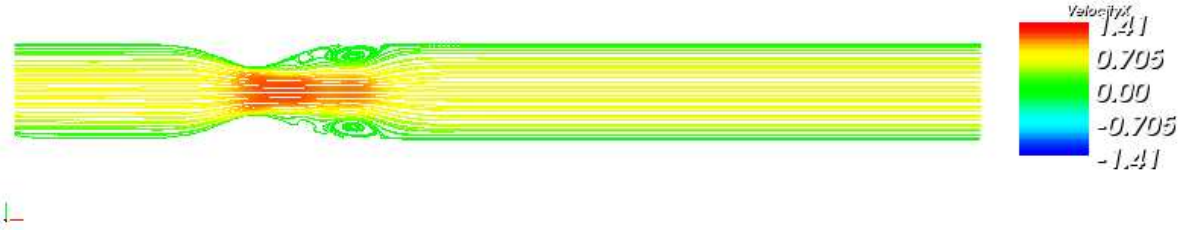

Figure 118: Streamlines colored by the x-velocity, $Str = 1$, $Re = 400$, $(Wo = 25.05)$, $t = 6$

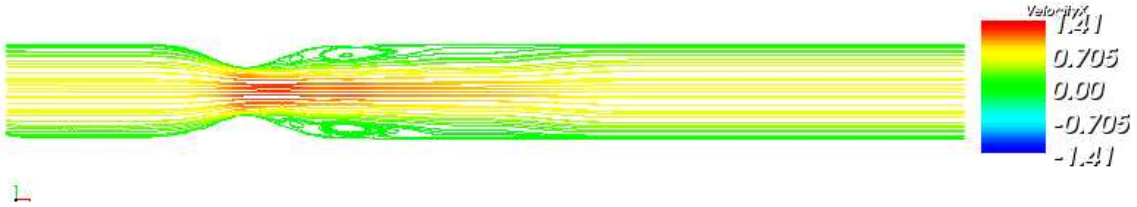

Figure 119: Streamlines colored by the x-velocity, $Str = 1$, $Re = 400$, $(Wo = 25.05)$, $t = 11$